

DISSERTATION

HIGHLY RELATIVISTIC LASER INTERACTIONS WITH ORDERED NANOSTRUCTURES

Submitted by

Reed Hollinger

Department of Electrical and Computer Engineering

In partial fulfillment of the requirements

For the Degree of Doctor of Philosophy

Colorado State University

Fort Collins, Colorado

Spring 2019

Doctoral Committee:

Advisor: Jorge J. Rocca

Amy L. Prieto
Carmen Menoni
Mario Marconi

Copyright by Reed Hollinger 2019

All Rights Reserved

ABSTRACT

HIGHLY RELATIVISTIC LASER INTERACTIONS WITH ORDERED NANOSTRUCTURES

Heating high density matter to extreme temperatures has been one of the primary motivations behind the construction of high power laser facilities around the world. The creation of simultaneously hot (multi-keV) and dense (on the order of a solid) plasma with small scale and mid-scale lasers is a difficult problem due to the barrier that the critical electron density imposes to optical lasers, typically limiting the heating to a very thin plasma into which the laser is inefficiently coupled. Experiments conducted at Colorado State University with joule level laser pulses have demonstrated that using high contrast, relativistic laser pulses it is possible to efficiently heat near solid density nanowire arrays volumetrically to multi-keV temperatures. This dissertation extends these results to the highly relativistic regime, demonstrating extremely high ionization states for volumes $>5\mu\text{m}$ in depth. These relatively large volume plasmas have longer hydrodynamic cooling times while their radiative cooling time is greatly decreased due to the near solid electron densities. This results in very efficient conversion of optical laser light into x-rays since the plasma is able to radiate away more of its' energy as x-rays before cooling due to hydrodynamic expansion. With this technique, an x-ray conversion efficiency of nearly 20% was measured for photon energies greater than 1keV. After a significant upgrade to the laser, these interactions were explored at highly relativistic intensities up to $4 \times 10^{21} \text{ Wcm}^{-2}$, nearly 1000 times higher than initial experiments. Measurements of the energy deposition dynamics, including the time limit for energy coupling and the volume of the nanowire plasma were carried out in comparison to solid targets. The results show that at these intensities, it is possible to generate unprecedented degrees of ionization never before obtained with ultrashort pulse lasers, such as H-like Ni (27 times ionized) and Ne-like Au (69 times ionized).

ACKNOWLEDGEMENTS

I would like to thank my advisor, Jorge Rocca, for his incredible insight, guidance and support during my PhD. The lab has inherited a 'do it yourself' attitude from him, creating an environment where problems, most often times unexpected, can be solved in a moments notice using tools that are either on hand or can be shipped overnight.

I would also like to acknowledge the immense support of my committee members: Amy Prieto for her important contributions in helping our group learn and perfect nanowire synthesis, Carmen Menoni for her expertise in thin film coatings and helping us make high damage threshold coatings, and finally Mario Marconi for his fascinating lectures early on in my PhD which helped me contextualize a lot of unfamiliar ideas in optics.

Over the course of my PhD I have worked with a lot of stellar individuals whose work has provided our lab a laser that is virtually unmatched at the University level. Yong Wang, Shoujun Wang, Alex Rockwood, Liang Yin and Brad Luther have designed, built and maintained a petawatt class Ti:Sapphire system which continues to receive the attention of researchers worldwide. That system is the backbone of the experimental results presented in this dissertation and I am grateful to be able to work with such experienced laser scientists. Michael Purvis and Clayton Bargsten were instrumental in getting this project off of the ground and it was a great experience spending the first few years of my PhD working with them to get the first nanowire results. In running the experiments, I would like to acknowledge the work and friendship of Alden Curtis, Adam Moreau, Chase Calvi, and Huanyu Song. I would also like to acknowledge the continued help from Maria Capeluto as she pushed our abilities to fabricate more exotic nanostructures. Lastly, I must acknowledge fruitful conversations with Brendan Reagan– he was undoubtedly a source of common sense approaches to solving problems in the lab.

Our modeling collaborators have afforded us great insights into the ultrafast dynamics of laser matter interaction with their sophisticated code that continue to elevate our manuscripts. Vyacheslav Shlyaptsev, Alexander Pukhov and Vural Kaymak have made enormous contributions to our

research and I thank them for all of their help. Experimental collaborations with Riccardo Tomasini, Ronnie Shepherd and Jaebum Park at LLNL as well as Matthew Hill at AWE have greatly increased the visibility of this research as we explore these interactions at high energy facilities.

Finally, I would like to acknowledge the love and incredible support of my wife, KatiLyn as well as my family, Bonnie, Russell, Zachary, Leslie and Anita. They encouraged me and supported me throughout my entire education.

This work was supported by the Fusion Sciences program of the Office of Science of the U.S Department of Energy. Previous support from the Defense Threat Reduction Agency is also acknowledged. Part of the simulations were conducted using the CU-CSU Summit computer facilities funded by the National Science Foundation.

TABLE OF CONTENTS

	ABSTRACT	ii
	ACKNOWLEDGEMENTS	iii
	LIST OF FIGURES	vii
Chapter 1	Introduction	1
1.1	Background and Motivation	1
1.2	Absorption of a laser into matter	3
1.3	Previous work heating solid density targets in laser experiments	8
1.4	Previous work heating nanowire arrays in laser experiments	12
1.5	Current work	17
Chapter 2	Highly relativistic $\lambda=400\text{nm}$ beamline and experimental setup	19
2.1	Colorado State University Petawatt Class Ti:Sapphire	19
2.2	Diffraction limited f/2 off axis parabola focus	22
2.3	Nanowire target alignment	23
2.4	X-ray crystal spectrometer	25
2.5	Nanowire Fabrication	26
Chapter 3	Efficient picosecond x-ray pulse generation from plasmas in the radiation dominated regime	29
3.1	Introduction	29
3.2	Creating favorable conditions for high x-ray conversion efficiency	30
3.3	Methods	31
3.4	Results and Discussion	33
3.5	Conclusion	41
Chapter 4	Energy deposition dynamics of highly relativistic femtosecond laser pulses into nanowire array plasmas	43
4.1	Introduction	43
4.2	Measurement of efficient coupling into near solid density nanowire arrays	45
4.3	Gap closure time for 100nm diameter Ni nanowire arrays at two densities	49
4.4	Conclusion	54
Chapter 5	Extreme degree of ionization in near solid density plasmas volumetrically heated by highly relativistic laser pulses	55
5.1	Introduction	55
5.2	Gold L shell emission at highly relativistic intensities	57
5.3	Strong Lyman- α emission from Ni nanowires and solid density targets	58

5.4	Measurement of heat penetration into solid density Ni using buried Co tracers	61
5.5	Lateral source size of nanowire and solid density targets	65
5.6	Conclusion	69
Chapter 6	Conclusions	70
Bibliography	72

LIST OF FIGURES

1.1	Dispersion relationship for an overdense plasma	5
1.2	Dispersion relationship for a plasma with relativistic correction	8
1.3	K shell emission from a stainless steel foil irradiated at $3 \times 10^{21} \text{ Wcm}^{-2}$	9
1.4	Heating of Al foils buried under varying depth of plastic	11
1.5	Heating of Ni foils buried under varying depth of Mo irradiated at $5 \times 10^{20} \text{ Wcm}^{-2}$	13
1.6	K shell emission from Ni nanowires and solid density target irradiated at $I=5 \times 10^{18} \text{ Wcm}^{-2}$	14
1.7	Measurement of volumetric heating in nanowire arrays at $I=4 \times 10^{19} \text{ Wcm}^{-2}$	16
2.1	Colorado State University 0.85 PW 3.3 Hz Ti:Sapphire laser with high intensity second harmonic beamline	20
2.2	CSU Petawatt class Ti:Sapphire laser contrast	21
2.3	f/2 Off axis parabola focus	22
2.4	Target alignment microscope system	24
2.5	Von Hamos crystal spectrometer setup	26
2.6	Nanowire synthesis steps	27
3.1	3D PIC Simulation for 55nm Au nanowires for $I=4 \times 10^{19} \text{ Wcm}^{-2}$	34
3.2	X-ray radiation power for a flat and a nanowire	35
3.3	Radiative and hydrodynamic cooling times for flat and nanowire targets	37
3.4	Angular distribution of x-ray emission	39
3.5	Total X-ray conversion efficiency for flat and nanowire targets	40
3.6	Point projection radiography of a wasp knee	41
4.1	Two pump pulse setup to measure energy deposition into nanowire arrays	47
4.2	Integrated He- α and He/Li line emission from 100nm Ni nanowire arrays versus input energy.	48
4.3	Ionized K shell x-ray spectra from 100nm Ni nanowire arrays at a quarter solid density at different intrapulse delays	50
4.4	Comparison of He-like emission versus time for two different interwire gaps at two intensities: $5 \times 10^{19} \text{ Wcm}^{-2}$ and $1 \times 10^{21} \text{ Wcm}^{-2}$	52
4.5	X-ray conversion efficiency for $h\nu > 1\text{keV}$ at different intrapulse delays	53
5.1	Ge ionized K shell emission used to calibrate Au L shell	58
5.2	FLYCHK Steady state ionization balance of Au plasma at 7keV for a nanowire plasma ($n_e=3 \times 10^{23} \text{ cm}^{-3}$) and a solid density plasma ($n_e=3 \times 10^{24} \text{ cm}^{-3}$)	59
5.3	Au L shell from 9.7-11keV comparison of solid density target and 55nm 12% fraction of solid density nanowire array at $I=4 \times 10^{21} \text{ Wcm}^{-2}$	60
5.4	Single shot x-ray spectra of ionized K shell emission from 55nm diameter Ni nanowire array and a solid density flat target	62
5.5	Measurement of heat penetration into solid density nickel flats	64
5.6	Point projection radiographs of tungsten carbide sphere to determine lateral source size	66

5.7 X-ray conversion efficiency of 100nm diameter Ni nanowires and solid density targets
for $h\nu > 1\text{keV}$ and 6keV 68

Chapter 1

Introduction

1.1 Background and Motivation

Heating solid density matter to extreme temperatures has motivated the construction of some of the largest laser facilities in the world [1–4]. The creation of simultaneously hot (multi-keV) and dense (on the order of a solid) plasmas in the laboratory is difficult due to the poor absorption of optical laser light into solid density matter. This is primarily due to the formation of a critical electron density which effectively shields the laser target from the impinging optical laser light and results in poor coupling of the laser energy into the solid. Spherical compression experiments concerning inertial confinement fusion performed at state of the art facilities such as the National Ignition Facility at Lawrence Livermore National Lab and the OMEGA laser at the Laboratory for Laser Energetics have achieved controllable, long lived plasmas with pressures $>100\text{Gbar}$ and high temperatures ($>1\text{keV}$) [5, 6]. These plasma conditions, similar to those found in the centers of stars, have been out of reach for smaller laser facilities.

There have been rapid developments in laser technology since the first demonstration of the ruby laser by Theodore Maiman in 1960 [7]. In the past 50 years, peak laser powers have increased from kilowatts to petawatts— an increase of over a trillion times. Focusing a petawatt class laser with a high numerical aperture optic can result in light intensities exceeding 10^{22} Wcm^{-2} at the focus [8]. At these intensities, the radiation pressure defined by the ratio of the intensity of the laser [W/cm^{-2}] divided by the speed of light [$3\times 10^{10}\text{ cm/s}$] exceeds a 10^{12} bar. Therefore, it is possible to generate enormous pressures and almost instantaneously heat matter to millions of degrees using a high intensity laser. This is achieved by carefully focusing the energy of an ultrashort laser pulse to a diffraction limited spot onto a target provided there is strong coupling between the impinging laser and the target [9]. This has resulted in the laser becoming one of the most important tools for creating high energy density plasmas in the laboratory.

Using novel targets such as vertically aligned nanostructures has provided a pathway for experimentalists to create these types of ultrahigh energy density plasmas in the laboratory using compact, table top laser drivers. Classified as energy densities $>10^8 \text{ Jcm}^{-3}$, this energy density regime is difficult to access for joule class laser systems. Previous work performed at Colorado State University with aligned nanostructure arrays demonstrated that it is possible to achieve these ultrahigh energy densities using less than one joule of laser energy [10, 11] owing to the increased coupling of the driving laser pulse with the target and the creation of a volumetrically heated plasma. This is possible using relativistic, high contrast laser pulses clean of any prepulses sufficiently intense to ionize the target surface, thus preventing the generation of an unfavorable preplasma which would reflect the main laser pulse.

The generation of plasmas using aligned nanowires is currently being extensively studied, especially for radiation and particle source development applications. These targets are proving to be efficient sources of x-rays [12–15], charged particles such as protons and electrons [16, 17], and neutrons [18] with large increases in comparison to solid density targets. As laser technology advances, the prospect of laser driven particle and x-ray sources replacing conventional sources looks increasingly plausible. For example, short pulse laser driven neutron and x-ray sources emit on the picosecond time scale, when compared to the nanosecond time scale found in pulsed power neutron sources such as dense plasma focus and pinch driven x-ray machines. Not only is this a significant increase in the brightness of the source, but it also translates into higher quality radiographs since there is no motion blur for very fast time scale events, such as compression of fusion capsules in inertial confinement fusion experiments. Moreover, laser driven sources can be converted from x-ray generation to neutron or ion generation by simply changing the target at the focus of the laser— requiring only one laser driver to be developed. Lastly, these sources are point like since they are typically driven by lasers focused to micrometer spot sizes. Small source sizes allow users to perform point projection radiography. In this setup, an object is simply placed between the point like source and a detector and the magnification of the imaging system is the ratio of the source to object and object to detector distances.

This dissertation is primarily concerned with the interaction of highly relativistic laser pulses ($>10^{21}$ Wcm $^{-2}$) with near solid density, ordered nanostructures. This work has significantly increased the x-ray conversion efficiency of laser driven picosecond x-ray sources available with current laser technology. Fundamental aspects of the interaction were studied including the time limit for efficient coupling of the driving laser pulse was measured for relativistic and highly relativistic intensities. Finally, these interactions demonstrated the creation of highly ionized plasmas such as Ne-like Au and H-like Ni using <10 J of laser energy– a first for compact, table top laser systems.

1.2 Absorption of a laser into matter

Consider the simple case of a laser field incident on a hydrogen atom. In order to ionize the electron bound to the nucleus, the minimum electric field of the laser must be:

$$E_{bind} = \frac{e}{4\pi\epsilon_0 a_b^2}$$

Where $a_b = 4\pi\epsilon_0\hbar/m_e e^2$ is the classic Bohr radius. For hydrogen, this is $\approx 5 \times 10^{-11}$ meters. Solving for the electric field strength required to ionize a hydrogen atom yields 5×10^9 V/m. The electric field strength is related to the laser field intensity by:

$$I = 0.5\epsilon_0 c |E|^2$$

Therefore, the necessary laser intensity (neglecting multiphoton ionization) required for the ionization of hydrogen is $>10^{16}$ Wcm $^{-2}$. Increasing the laser intensity even higher causes the field to directly modify the coulomb electric potential of the atom, effectively lowering the ionization barrier– this is referred to as tunneling ionization. This allows a high intensity laser field to rapidly ionize matter, creating a plasma comprised of a significant number of free electrons which gain tremendous energy in the laser field. For intensities below 10^{16} Wcm $^{-2}$, ionization can still occur due to multiphoton ionization. This can be understood as the probability of several photons

with energy below the ionization threshold combining their energies to promote a free electron from a bound state. The Keldysh parameter is used to analyze which mechanism, tunneling or multiphoton ionization, dominates in a laser matter interaction. This parameter is defined as:

$$\gamma = \omega_{laser} \frac{\sqrt{2m_e V_I}}{eE_{laser}}$$

Where V_I is defined as the zero field ionization energy, ω_{laser} is defined as the angular frequency of the laser, m_e and e are the mass and charge of an electron and E_{laser} is the electric field strength of the impinging laser. For $\gamma \gg 1$, multiphoton ionization will occur, whereas for $\gamma \ll 1$, tunnel ionization from the laser field will dominate.

For an intensity of $5 \times 10^{18} \text{ Wcm}^{-2}$, a small fraction of the electrons will be accelerated to relativistic velocities, acquiring an energy greater than their rest mass of 511keV. At these intensities, mechanisms such as vacuum heating described by Brunel [19], become very important. When the product of the laser intensity and the square of its' wavelength (known as $I\lambda^2$), exceeds 10^{18} , this process begins to dominate as the primary absorption of the laser energy. In this process, the laser's electric field is sufficiently strong to ionize atoms and accelerate the free electrons in the field away from the target surface during the first half of the laser cycle. As many electrons are simultaneously pulled from the target surface, a strong positive space charge is formed at the target surface, causing the electrons to accelerate back into the target surface with additional energy gained from the second half of the laser field cycle, which has reversed direction. The kinetic energy of these electrons are transferred into the plasma through collisions, additionally ionizing other bound electrons provided the kinetic energy transferred is greater than the ionization potential of the bound electrons. These electrons are in turn accelerated by the laser to produce more electrons in which is described as avalanche ionization.

There is a significant limit to this process though, as the free electrons can begin to screen out the incoming electric field of the laser. This fundamentally limits the energy deposition of the laser into the solid density target. Consider the dispersion relationship for an electromagnetic wave propagating in a plasma:

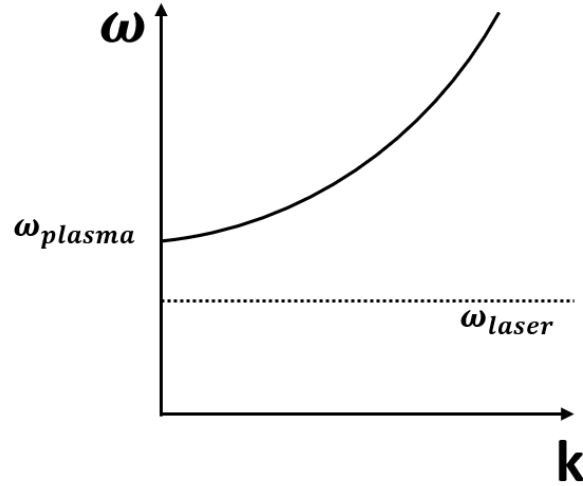


Figure 1.1: Dispersion relationship for a solid density plasma with frequency, ω_{plasma} , and a visible laser with frequency, ω_{laser} .

$$\omega_{laser}^2 = \omega_{plasma}^2 + k^2 c^2$$

In this equation, ω_{laser} represents the frequency of the incident laser light and ω_{plasma} represents the frequency of the electrons that can collectively oscillate in the plasma and is defined as:

$$\omega_{plasma}^2 = \frac{n_e e^2}{m_e \epsilon_0}$$

From this equation, it is readily apparent that the plasma frequency is only dependent upon the electron density of the plasma, unless the mass of the electron is modified through relativistic motion, which will be considered shortly. In order for the electromagnetic wave of the laser to continue propagating in this plasma medium, the wave vector k must be greater than 0.

Therefore, a critical electron density exists for which a laser with frequency ω_{laser} can no longer propagate in a plasma with frequency ω_{plasma} . This is plotted in Figure 1.1 for a solid density plasma with frequency ω_{plasma} and a visible laser, ω_{laser} . The laser frequency is not high enough for the laser beam to propagate in the plasma. Considering the case where $k=0$, then $\omega_{plasma}^2 = \omega_{laser}^2$ and the following relationship can be derived for the electron density:

$$n_{crit} = \frac{m_e \epsilon_0 \omega_{laser}^2}{e^2}$$

Solving for n_{crit} in terms of laser wavelength provides a useful, back of the envelope calculation:

$$n_{crit} = \frac{1.1 \times 10^{21}}{\lambda^2 [\mu m]}$$

Considering solid density matter has electron densities on the order of 10^{24} cm^{-3} , light cannot penetrate more than the skin depth into material, which is typically tens of nanometers for metals. Moreover, the formation of a critical density surface will reflect further incoming laser light, which has been leveraged in the field of high intensity plasma mirrors [20]. This leaves only four options for overcoming the barrier imposed by the critical density when attempting to heat a large volume of plasma.

One approach is to use shorter wavelength lasers, such as x-ray lasers with wavelengths on the order of nanometers. The critical electron density for a $\lambda = 10 \text{ nm}$ x-ray laser is 1.1×10^{25} . These are useful tools, however even the most expensive x-ray laser facilities in the world such as the Linear Coherent Light Source can only generate several mJ of energy.

Limiting the discussion to the case of optical lasers, the simplest approach is starting with what is colloquially known as an underdense target. For example, irradiating a gaseous target with densities of only 10^{19} cm^{-3} will remain under the critical density for a $1 \mu m$ laser wavelength, allowing for the laser to propagate and volumetrically heat the low density volume. These low density plasmas do not have high collisional rates and therefore their radiation cooling lifetime is long, resulting in long radiation emission time which reduces the brightness of the source. To

significantly decrease the emission time, it is necessary to increase the density several orders of magnitude, approaching solid density.

To couple efficiently to a solid density target, the laser intensity must increase for visible wavelength lasers. As the laser intensity increases well beyond 10^{18} Wcm^{-2} , the electrons move relativistically and as a result, their mass increases by the relativistic parameter $\gamma = 1/\sqrt{1 - (v^2/c^2)}$. This decreases the plasma frequency, ω_{plasma} by a factor of γ shown in Figure 1.2 and thus increases the critical electron density. For a thick solid density gold target to appear transparent to a $\lambda = 1 \mu\text{m}$ laser pulse, the laser intensity would need to exceed $5 \times 10^{24} \text{ Wcm}^{-2}$, an intensity that is over 200 times higher than what is currently available in the laboratory.

Finally, the fourth option and the focus of this dissertation is creating a near solid density structure using an engineered nanostructure target, herein described as a nanowire array in which the laser can propagate deeply before the formation of a critical electron density. In such a target, the laser can propagate into the nanowire array where it is trapped and nearly completely absorbed provided it is deposited on a time scale faster than the formation of a supercritical electron density between the wires. In order to understand the dynamics of this interaction, experiments were conducted to probe the depth of the hot plasma formation, the x-ray conversion efficiency, the time that it takes for the wires to explode and form a critical density plasma and the degree of ionization occurring in the nanowire arrays when irradiated at highly relativistic intensities.

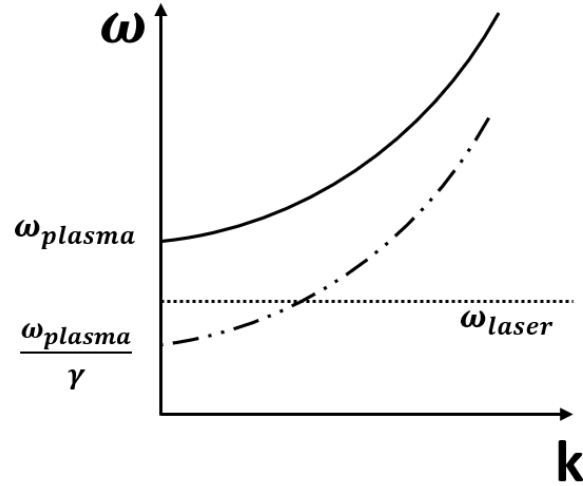


Figure 1.2: Relativistically corrected dispersion relationship for a relativistic solid density plasma with frequency, $\frac{\omega_{plasma}}{\gamma}$ and a visible laser with frequency, ω_{laser} .

1.3 Previous work heating solid density targets in laser experiments

Lasers have long been proposed as a method of heating solid matter. A. Caruso and R. Gratton theoretically analyzed the problem of a terawatt (10J, 10ps) laser pulse irradiating a target in 1968 [21]. They concluded that the plasma production for a short pulse laser is significantly different than nanosecond laser matter interactions and it may be possible to heat a solid 'speck' of matter to keV temperatures. J. Bechtel considered the heating of solid targets with pulsed lasers in 1975 [22]. He found that for 30ps laser pulses with intensities below the ionization threshold (1 GW cm^{-2}), it was possible to heat a tungsten surface up to 700 kelvin in less than 20ps, with a temperature of several hundred kelvin tens of nm into the bulk.

As lasers achieved higher intensities, many research groups investigated the heating of solid density matter using short pulse, high intensity beamlines, relevant to the research in this dissertation. The first laser to reach the petawatt threshold, a kilojoule of laser energy in a picosecond was implemented converting one of the arms of the NOVA laser at LLNL into a chirped pulse amplification system [23]. This laser system could achieve focal intensities of $7 \times 10^{20} \text{ Wcm}^{-2}$, opening

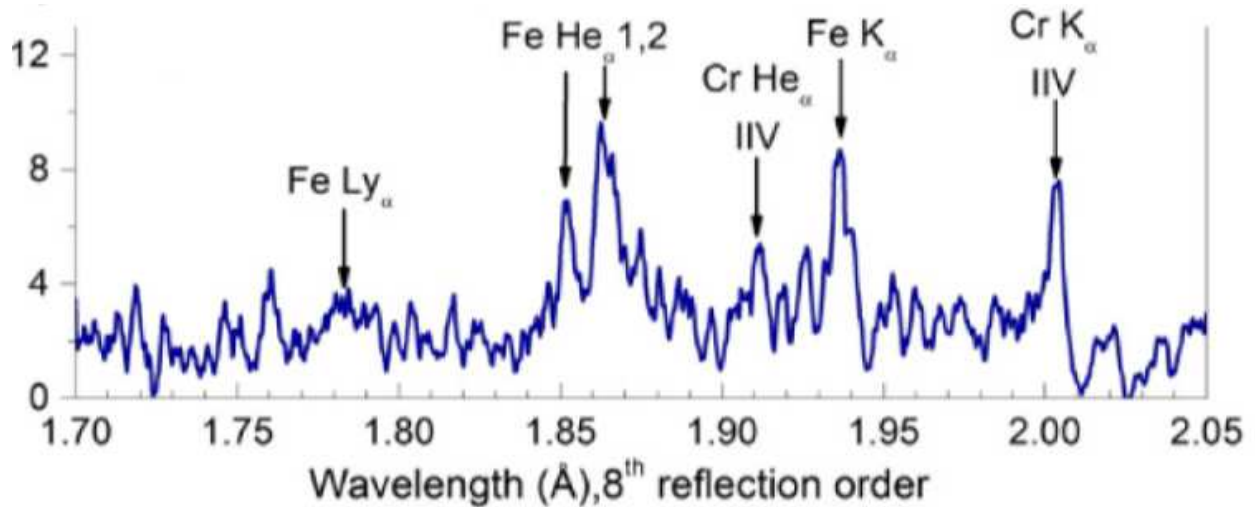


Figure 1.3: Ionized Fe K shell emission from a stainless steel foil irradiated at an intensity of $3 \times 10^{21} \text{ Wcm}^{-2}$ by Alkhimova et al [28]

a new door to relativistic laser matter interactions. Electron, photon and ion spectra and flux were measured, with estimates of 40% to 50% of the laser energy being converted into high energy electrons, generating bright protons and x-rays [24].

Recent experiments by Faenov et al have shown that at intensities $>10^{21} \text{ Wcm}^{-2}$ there exists an unusual nonlinear growth of the x-ray emission from the plasma periphery proportional to E^{4-5} , where E is the laser energy deposited in micron thick Al foils [25]. According to their modeling, a central hot spot of $>1\text{keV}$ at near solid density generates an x-ray field with an intensity of $>10^{17} \text{ Wcm}^{-2}$ for keV x-rays. This x-ray field deposits energy into the adjacent cold matter, heating it to hundreds of eV and generating KK hollow ions measured by their crystal spectrometer.

This action of this high energy, high intensity x-ray field heating up material is referred to as a radiation dominant kinetic regime (RDKR) as the radiation ionization process dominates the standard collisional atomic processes. This creates ions which have their outer valences intact, yet have substantially ionized inner shells which is useful for comparison against atomic physics models. This is similar to the exotic states of matter created at x-ray free electron lasers (XFEL) facilities such as the Linac Coherent Light Source (LCLS) at the Stanford Linear Accelerator [26, 27], but with a much more compact light source— a petawatt class laser.

This same group has also done work irradiating mid Z elements, in this case stainless steel foils containing mostly Fe with some Cr and Ni. At an intensity of $3 \times 10^{21} \text{ Wcm}^{-2}$ emission from He-like Fe was observed similar in intensity to the neutral K- α as well as a small amount of H-like Fe signal, comparable to the continuum [28] shown in Figure 1.3. With this, the modeling (Spectroscopic Collisional-Radiative Atomic Model SCRAM [29]) suggested an electron temperature of 2.1keV at an electron density of $5 \times 10^{22} \text{ cm}^{-3}$. From this they infer that the laser energy is absorbed in the relativistic critical density only several hundred nm in depth.

Extensive studies of the heating of Al foils buried in plastic with second harmonic $\lambda = 527\text{nm}$, 100J, 500fs pulses by Hoarty et al at the ORION laser facility at the Atomic Weapons Establishment (AWE) in the UK has demonstrated the importance of high laser contrast when heating large volumes. The temperature of the Al foils were measured by monitoring the He-like and H-like α and β lines while varying the amount of plastic on top of the Al at an intensity of $1 \times 10^{19} \text{ Wcm}^{-2}$. It was found that 500TW pulses with poor laser contrast heated the Al to 300-500eV under less than $5 \mu\text{m}$ of plastic. When ORION was frequency doubled and high contrast, second harmonic light was used to irradiate the target at a power of 150TW, temperatures of 700-800eV were achieved under $5 \mu\text{m}$ of plastic and $>600\text{eV}$ at $25 \mu\text{m}$ of plastic [30] shown in Figure 1.4.

By shock compressing the Al foils with ns duration kJ pulses, ORION was also able to demonstrate measurements of ionization potential depression occurring in Al foils shock compressed to above solid density. The field from neighboring ions in high density plasmas as well as free electrons in the plasma causes the electron binding energies to be lowered causing line transitions to merge with the continuum. This effect manifested itself in the suppression of the 3-1 He-like and H-like Al lines when the shock compressed Al reached 9g/cc, roughly three times solid density [31]– the first time these effects were measured using high intensity laser matter interactions.

Work by Akli et al determined the plasma conditions of a solid density Ni layer buried underneath a varying amount of Mo irradiated with 400J, 800fs pulses focused to a peak intensity of $5 \times 10^{20} \text{ Wcm}^{-2}$ by performing x-ray spectroscopy of K shell emission from the Ni layer [32]. K shell and L shell spectroscopy is a useful indicator of temperature since the density is reason-

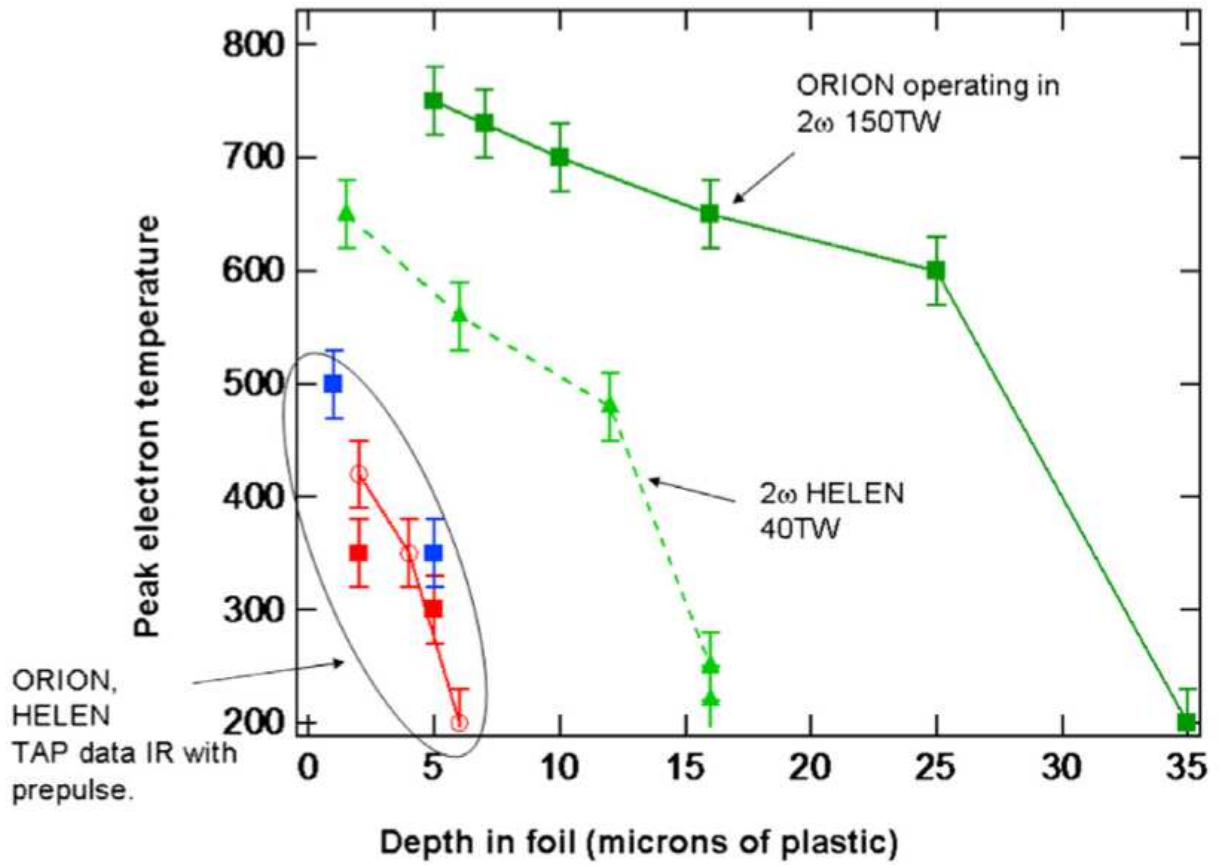


Figure 1.4: Buried Al foils irradiated with up to 500TW low contrast laser pulses (ORION, HELEN IR data with prepulse) and high contrast, second harmonic beams (ORION and HELEN 2ω by Hoarty et al [30])

ably well known for such targets, allowing modelers to vary the plasma temperature to match the ionization state of the experiment.

The thickness of the molybdenum layer on the top of the Ni layer was varied from $0\mu\text{m}$ to $1\mu\text{m}$ while observing the change in the He-like and H-like Ni emission as well as the Mo emission from the front and the back of the target shown in Figure 1.5. The contrast of the laser was measured to be 4×10^{-8} , suggesting that the prepulse had some influence on the measurements since it was roughly at the ablation threshold of the material. Interestingly, emission from the front surface of the target yielded virtually no H-like line emission even when the Ni tracer was not buried under any Mo. Instead, some H-like emission was measured at the rear of the target. For half a micrometer of Mo on top, the emission from Ni decreased substantially and could not be measured at $1\mu\text{m}$ depth. Modeling suggested that the surface layer was heated to $\approx 5\text{keV}$ decreasing to $\approx 2\text{keV}$ in the first 100nm of the target. At a depth of $1.3\mu\text{m}$, the temperature was $<600\text{eV}$, insufficient to reach the He-like ionization state of Ni. This measurement inspired a similar measurement in Chapter 5 of this dissertation, which demonstrated that at higher intensity, a larger depth of material could be heated using less than 10J of laser energy.

1.4 Previous work heating nanowire arrays in laser experiments

Previous work had shown the advantage of using structured targets, such as 'smoked' clustered targets [13, 33, 34], nanometer sized spheres and ellipsoids [14, 35], micro-lithographic gratings [33, 36, 37] and nanowire arrays to increase the absorption efficiency [13, 15, 38, 39]. In comparison to solid density targets, it was generally found that these nanostructured targets absorb more laser light and emit more x-rays, many times that of solid targets. For example, the work by Kulcsar et al achieved 0.1% conversion efficiency for optical light into x-rays $>900\text{eV}$ irradiating $1\mu\text{m}$ Ni tall, 70nm diameter nanowire arrays, a 50x increase over solid density targets [13]. Mondal et al achieved a 43x increase in hard x-ray emission (for $150\text{-}300\text{keV}$ photons) from Cu nanorods in comparison to solid density targets [39]. Ovchinnikov et al measured a 3x increase in $\text{K-}\alpha$ yield

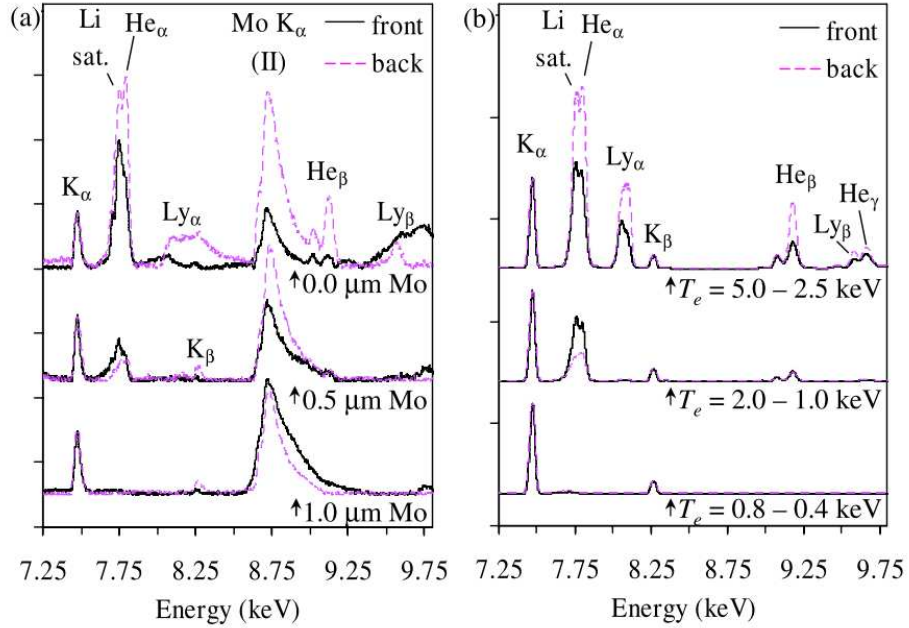


Figure 1.5: Measurements of He-like and H-like emission from Ni foils buried under a varying amount of Mo at an intensity of $5 \times 10^{20} \text{ W cm}^{-2}$. The spectra in (a) was measured from the front and rear surfaces and modeling of the spectra in (b) predicts the temperatures for target configuration by Akli et al [32].

from Cu nanorods $1 \mu\text{m}$ in length [38]. The aforementioned work was primarily motivated by increasing the x-ray yield, often adjudicating the higher yields to increased laser absorption and electric field enhancement by the small scale features. These laser experiments did not address volumetric heating, which is shown to be key to achieving very efficient x-ray production. Moreover, the choice of laser parameters and target parameters, namely ps duration pulses, poor laser contrast and low aspect ratio nanowires prevented the formation of a large volume plasma.

The first experiments conducted at Colorado State University with nanostructured targets were designed to achieve a new nanostructure regime, in which efficient volumetric heating achieved by the careful selection of both target and irradiation parameters, would yield significantly enhanced x-ray conversion efficiency. These experiments used high contrast, femtosecond duration laser pulses with high aspect ratio nanowire arrays. It was discovered that it was possible to generate highly ionized plasmas with gigabar pressures, extending several microns in depth when irradiating metal nanowires at intensities of $5 \times 10^{18} \text{ W cm}^{-2}$ ($a_0 = 1$) only using 0.5J of laser energy [11]. Time integrated x-ray spectra from nickel nanowires, 55nm in diameter at a 12 % fraction of solid density

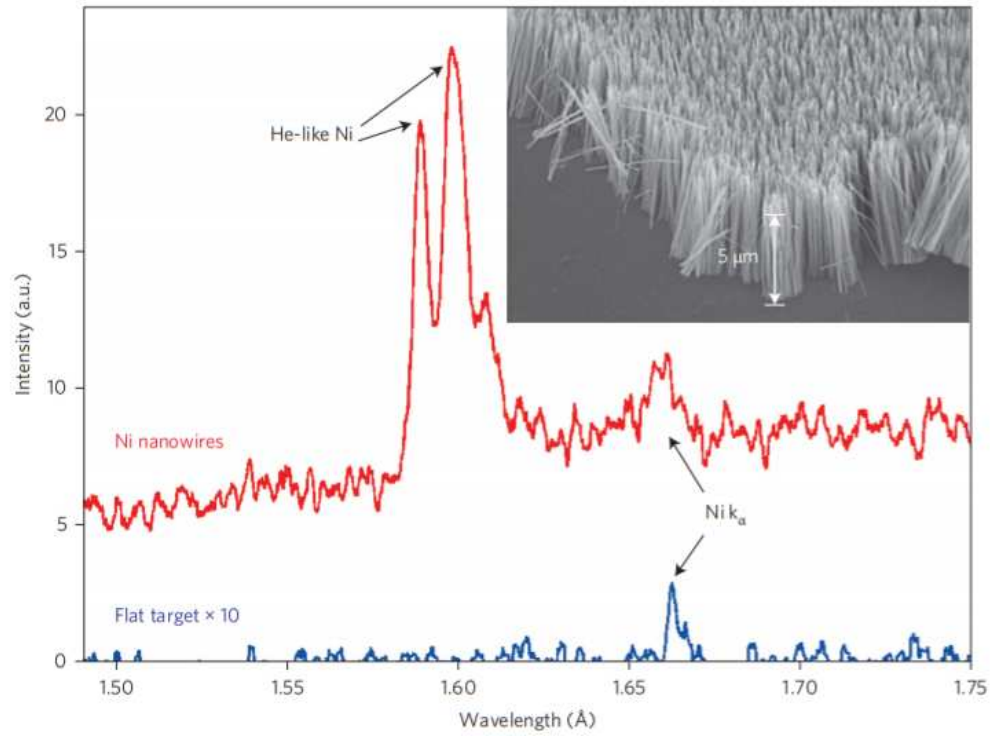


Figure 1.6: K shell emission of 55nm diameter Ni nanowires 12% of solid density in red compared to solid density target in blue multiplied by 10x. Both were irradiated at an intensity of $I=5 \times 10^{18} \text{ Wcm}^{-2}$. Work performed by Purvis et al [11]

revealed strong line emission from the He-like Ni $1s2p - 1s^2$ transition, over an order of magnitude greater in intensity than the characteristic cold K- α emission from neutrals as shown in Figure 1.6.

Previous experiments by Theobald et al conducted at the Jupiter Laser Facility demonstrated that cold K shell emission in a Cu plasma was exceeded by He-like emission only at intensities greater than $2 \times 10^{20} \text{ Wcm}^{-2}$ [40]. Simulations show that multi-keV temperatures are required to drive the large collisional rates necessary to create such highly ionized near solid density nanowire plasmas. In contrast, the result of the initial CSU experiment showed that this was possible with intensities of only $5 \times 10^{18} \text{ Wcm}^{-2}$, as a result of the creation of a new class of ultrahigh energy density plasmas using high contrast, femtosecond, joule level lasers.

The laser light, propagating between the wires, can volumetrically heat the sample creating a plasma with a longer lifetime than that of a solid density flat target. To measure the depth of the high temperature, near solid density plasma, an experiment was conducted using Ni and Co dual composition nanowire which made it possible to definitively measure the energy penetration of the laser in the array [10]. This was done by monitoring the ionized K shell x-ray emission from a buried Co tracer segment in the Ni nanowire array shown in Figure 1.7. It was found that at an irradiation intensity of $4 \times 10^{19} \text{ Wcm}^{-2}$ the emission of the Co tracer is still visible under up to 4 μm of Ni, giving direct experimental evidence of a volumetrically heated plasma.

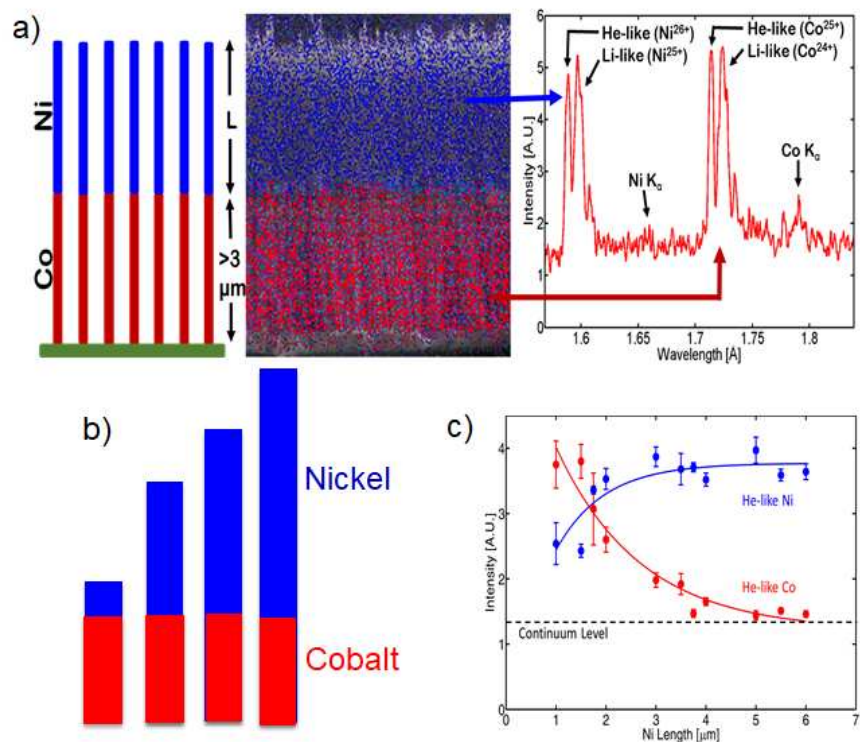


Figure 1.7: Ionized K shell emission from both Ni and Co was monitored from a dual composition nanowire target consisting of $3 \mu\text{m}$ of Co beneath a varying amount of Ni shown in (b). An x-ray spectra of the emission, shown in (a) contains significant emission from the He-like state of both Co and Ni, suggesting the Co underneath is heated to a significantly high temperature. The amount of Ni is varied on top while monitoring the normalized intensity of the He-like emission from both elements and the length is increased until the signal from the Co disappears at a depth of $4 \mu\text{m}$ [10].

A consequence of these high energy density, volumetrically heated plasmas is a significant increase in the conversion efficiency of the optical laser light into x-rays. The reason for this, elaborated upon in Chapter 3, is the combined effects of a large increase in the hydrodynamic lifetime of the volumetrically heated plasma as its depth increases, ΔL , when compared to a thin surface plasma from a solid density target and the plasma's significantly shortened radiative lifetime due its' high electron density, n_e . This combination leads to a condition where the plasma can radiate most of its' energy in the form of x-rays before cooling due to hydrodynamic expansion as described by:

$$\tau_{rad} \propto \frac{1}{\langle \sigma v \rangle n_e} < \frac{\Delta L}{C_s} \propto \tau_{hydro}$$

Where τ_{rad} is the radiative cooling time, τ_{hydro} is the hydrodynamic cooling time, $\langle \sigma v \rangle n_e$ is the total electron density dependent collisional rate and C_s is the acoustic velocity. By fulfilling the above inequality, an x-ray conversion efficiency of over 20% in 4π for photons with energies greater than 1keV was demonstrated irradiating 80nm diameter, 5 μ m long Au nanowires [12].

1.5 Current work

The rest of this dissertation is as follows: Chapter 2 details the experimental setup used to conduct the experiments, including the petawatt-class laser and high intensity second harmonic beamline used to conduct the experiments. This system, that is currently the highest focused intensity second harmonic beamline in the world, has enabled us to conduct the research in the following chapters:

Chapter 3 elaborates on the aforementioned large increase in x-ray yield achieved using the concept of creating plasma which primarily dissipates energy in the form of x-rays as opposed to hydrodynamic losses, leading to what is referred to as a radiation dominated regime. These results are compared to fully relativistic, three dimension particle in cell (3D PIC) simulations [41].

Chapter 4 introduces a two pump pulse experiment, designed to determine the dissociation time of the individual nanowires and subsequent filling of the interwire gaps with high density plasma

which affects the energy coupling. At highly relativistic intensities of $1 \times 10^{21} \text{ Wcm}^{-2}$, it is found that laser pulse durations must be $< 100\text{fs}$ to successfully couple into a 100nm diameter nanowire array at a quarter solid density.

Finally, Chapter 5 discusses the generation of near solid density plasmas with extreme ionization states achieved in nanowire arrays irradiated at highly relativistic intensities up to $4 \times 10^{21} \text{ Wcm}^{-2}$. It is found that using $< 10\text{J}$ of laser energy, it is possible to ionize Au to a Ne-like state (69 times ionized) and Ni to a H-like state (27 times ionized), the first time such a high degree of ionization is observed in a plasma generated by a compact laser system.

Chapter 2

Highly relativistic $\lambda=400\text{nm}$ beamline and experimental setup

2.1 Colorado State University Petawatt Class Ti:Sapphire

This work covers a large range of intensities, from the initial experiments conducted at an intensity of $5 \times 10^{18} \text{ Wcm}^{-2}$ to the most recent results, conducted at intensities exceeding 10^{21} Wcm^{-2} , an increase of 3 orders of magnitude in focal intensity. This was made possible by a laser that allowed us to increase the energy on target from less than half a joule to nearly 10J, as well as creating a diffraction limited focus with an $f/2$ off axis parabola, achieving a spot focus of $1.6 \mu\text{m}$. This system is described in "0.85 PW laser operation at 3.3Hz and high-contrast ultrahigh-intensity $\lambda = 400\text{nm}$ second-harmonic beamline" by Y. Wang et al. Figure 2.1 shows a schematic of the system, including the high contrast beamline designed specifically for the purpose of conducting the work contained in this dissertation [42]. A panoramic photo of the table top laser setup is seen in Figure 2.1b. The laser system is a chirp pulsed amplification (CPA) using titanium doped sapphire as the gain medium. It operates at a central wavelength of 800nm with 50nm of bandwidth FWHM, resulting in a 30 fs transform limited pulse duration. The first two stages of amplification generate pulses of up to 200mJ pulses at 10Hz and are pumped by a commercial Nd:YAG laser. This repetition rate is useful for alignment of diagnostics. The following three power amplifiers allow us to reach an energy of $\approx 36\text{J}$ before compression. These amplifiers are pumped with the second harmonic of a 1053nm neodymium glass slab laser that was designed to run up to 5Hz. However, experiments were typically conducted at a shot per minute rate, limited by plasma diagnostics.

The second harmonic beamline ($\lambda=400\text{nm}$) is the most important difference between this system and other femtosecond, petawatt-class beamlines. The second harmonic generation process is a χ^2 process, which implies that its' overall efficiency is proportional to I_L^2 . The laser's contrast is

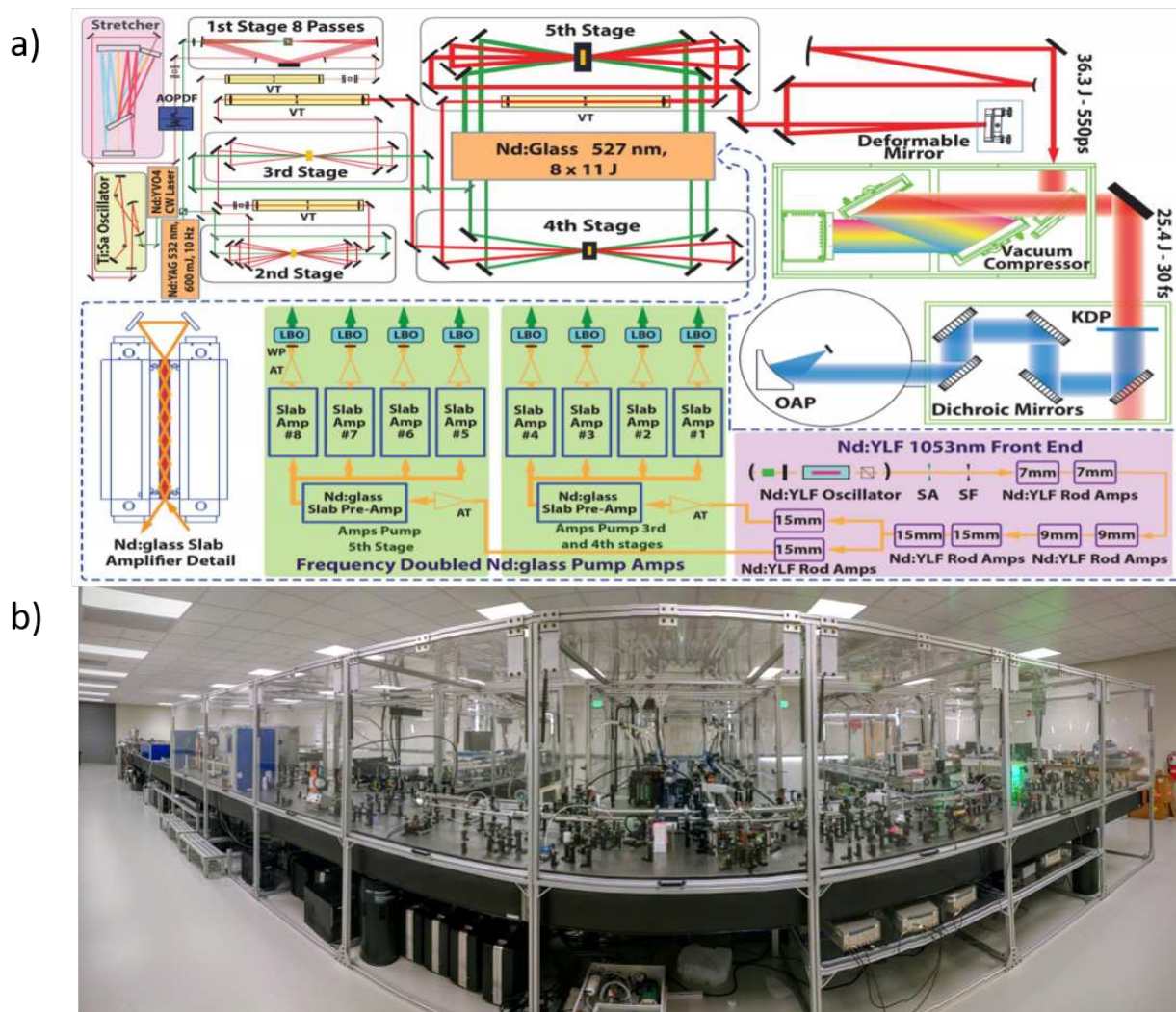


Figure 2.1: a) Diagram of the 0.85 PW, 3.3Hz Ti:Sapphire laser system. The Ti:Sa laser is on the top along with the second harmonic chamber using potassium diphosphate (KDP) and focused with an off axis parabola (OAP). The pump laser shown in the bottom is based on a Nd:glass slab amplifier. VT, vacuum tube; SA, serrated aperture; SF, spatial filter; AT, anamorphic telescope; WP, wave plate. b) A panoramic photo of the laser system.

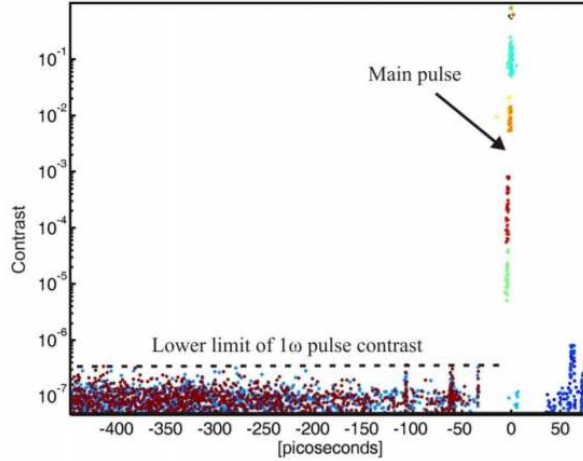


Figure 2.2: Contrast profile for 500ps leading up to the main pulse taken with a scanning third order autocorrelator

defined as the intensity ratio between the main pulse and the pulses preceding the main pulse. The contrast of the fundamental beam, illustrated in Figure 2.2 measured to be 5×10^{-6} . This suggests that when the main laser pulse achieves a focal intensity of $6.5 \times 10^{21} \text{ Wcm}^{-2}$ on target, the prepulse intensity would be on the order of 10^{16} Wcm^{-2} . This is significantly higher than the ablation threshold of nanostructured material, which has been measured to be $7 \times 10^{12} \text{ Wcm}^{-2}$ [43] for XXX. By exploiting the second harmonic process, it is possible to largely suppress the laser prepulses. The laser's contrast is squared provided the second harmonic (2ω) and fundamental are separated using dichroic mirrors reflective at 2ω and transmissive at the fundamental by more than the initial laser contrast. Currently, 5 dichroic mirrors are used to separate the fundamental from the second harmonic. Each mirror transmits $>99\%$ of the fundamental, resulting in an effective separation of 10 orders of magnitude. With this separation, the contrast is $> 10^{12}$ for this system and suppresses the laser prepulses several orders of magnitude below the ablation threshold, ensuring that the nanowires will not be destroyed and no unfavorable preplasma will be created before the main laser pulse arrives.

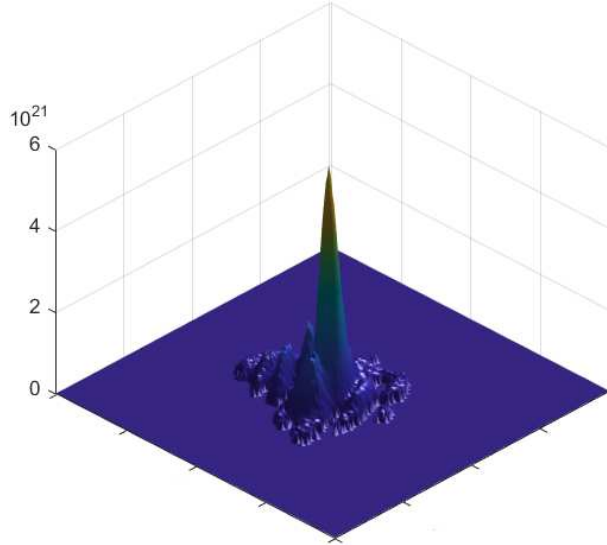


Figure 2.3: Spot focus taken with a 50x objective FWHM diameter of $1.6\mu\text{m}$

2.2 Diffraction limited $f/2$ off axis parabola focus

One of the most important aspects of the experiment setup is the final focusing optic. The diffraction limited focus, d , for a uniform intensity beam (flat top intensity profile) can be calculated by considering the first null of the Airy disk: $d = 2.44f\#\lambda$. Therefore, a $\lambda = 400\text{nm}$ beam focused with a $f/2$ optic will focus to a diffraction limit of $1.95\mu\text{m}$.

Unfortunately, a diffraction limited focus is not guaranteed after several stages of laser amplification and pulse compression. The laser pulse accumulates spatial phase through the laser chain which manifests itself as aberrations in the final focus. These aberrations are typically low order Zernike polynomials, dominated by coma and astigmatism and are corrected by the use of a programmable deformable mirror (Imagine Optics). The wavefront of the laser is measured by a Shack-Hartmann sensor which samples the slope of the wavefront at up to 1280 points. A feedback loop adjusts actuators on the deformable mirror to minimize the wavefront error, trying to cancel out the spatial phase and thus making the wavefront as flat as possible. With this technique, we have been able to create a wavefront with $\lambda/4$ peak to valley error and an $\lambda/15$ RMS error.

The spot focus is monitored in the chamber using a 20x or 50x Mitutoyo Infinity conjugated long working distance microscope objective coupled to a sensitive 12bit CCD detector. An exam-

ple of a spot focus is seen in Figure 2.3. The axis of the focusing optic is aligned to be collinear with the axis of the objective to ensure no additional aberration is generated in the measurement of the spot. The off axis parabola is slowly varied in its X and Y tip/tilt while observing changes in the spot focus, minimizing the size of it. Finally, small amounts of astigmatism and coma are added and subtracted using the deformable mirror to get the focus near a diffraction limit. This is necessary since the first wavefront correction is performed at the end of the laser chain before the grating compressor, second harmonic generation KDP crystal and 5 dichroic mirrors, all of which impart additional wavefront error.

2.3 Nanowire target alignment

Although the choice of a high numerical aperture focusing optic provides high intensity, there is a serious limitation that must be considered. Short focal length optics have short Rayleigh lengths which require the targets to be placed precisely in the focal plane to ensure maximum intensity. The Rayleigh length is defined as the distance from the beam waist to where the area of the beam is doubled and is calculated as $z_r = \pi w_o^2 / \lambda$ where w_o is the diffraction limited spot size. The confocal parameter is twice the Rayleigh length which defines the window that the target surfaces must be placed within for maximum intensity. For the aforementioned f/2 optic focusing a $\lambda = 400\text{nm}$ beam, the confocal parameter is only $16\mu\text{m}$.

To ensure the target surface is always in the focal plane of parabola, a Mitutoyo 20x finite conjugated, telecentric microscope objective coupled to a low power CMOS camera from Mightex was used to hold a reference plane at 45 degrees with respect to target normal shown in Figure 2.4. The objective has a confocal parameter of only $1.6\mu\text{m}$ and can resolve less than $1\mu\text{m}$.

It also has an ultralong working distance of 20mm, which allows it to not interfere with the XYZ motion of the target and target holder. The target is first placed in the focal plane of the parabola and then imaged with the microscope while a 10Hz pulse of several hundred nJ energy 'paints' the laser focal spot on the target surface. The shape of the focal spot can be observed from the image of the scattered light collected by the microscope objective. To ensure the target

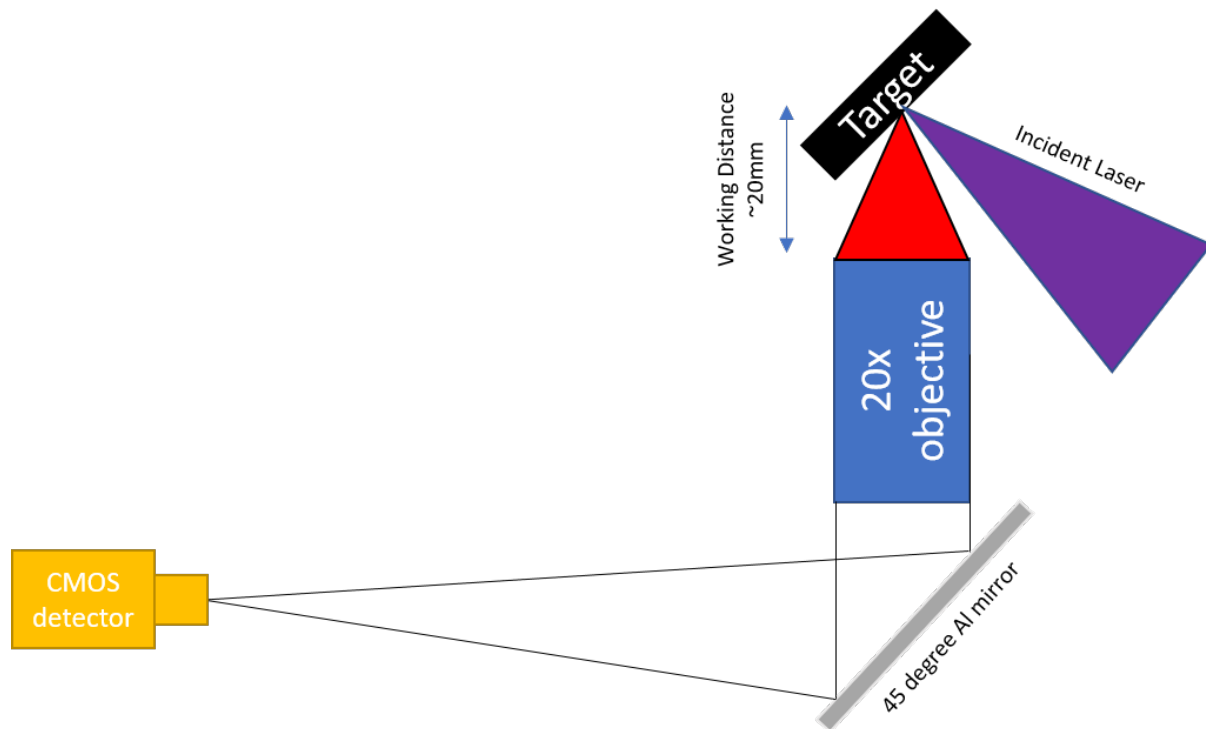


Figure 2.4: A finite conjugate 20x Mitutoyo ultralong working distance objective images the target front surface at a 45 degree angle onto a CMOS camera to ensure the target plane is consistently in the focal plane of the off axis parabola. The profile of the scattered focal spot can also be observed on the target.

is at best focus, the user can slowly vary the focal position of the target while following the spots position with the microscope until the scattered spot profile is at a minimum.

This technique has proven to be useful as it improved the consistency of experiments discussed in the following chapters. Recently, the microscope setup as well as the spot focal camera were put on a motorized, retractable vertical stage with micron precision limit switches. This prevents the imaging systems from blocking considerable solid angle that can be used for plasma diagnostics. As a result, multiple plasma diagnostics can be fielded simultaneously on the equatorial plane of the laser target interaction, greatly decreasing the number of experiments that need to be run.

2.4 X-ray crystal spectrometer

X-ray crystal spectroscopy is a powerful tool for diagnosing high energy density plasma temperatures and used extensively in this dissertation. While there are many geometries available for crystal spectroscopy, the Von Hamos configuration offers many advantages for laser driven plasma sources. This geometry, described extensively by Shevelko et al [44, 45], can be thought of as a focusing cylinder that is composed of many flat Bragg diffractors that all focus their dispersion planes to a single line. By doing this, the solid angle of the radiation collected by the crystal is greatly increased and results in a very high signal to noise ratio compared to non focusing geometries. In contrast to kJ and mJ class experiments that have enormous x-ray flux available for diagnostics, experiments using <10J of laser light must be carefully designed to collect sufficient x-ray flux to ensure a good signal to noise ratio.

Mica ($2d=19.84\text{\AA}$) was used for the measurements taken in this dissertation. Mica is easily cleaved and able to be bent into a cylindrical shape without very significant dislocations forming in the lattice preventing spurious signal from interfering with the spectrum. It also has very low mosaicity when compared to other diffractive crystals such as lithium fluoride (LiF) and highly oriented pyrolytic graphite (HOPG) that are also commonly used in laser driven plasma spectroscopy. This allows for moderate spectral resolution ($\Delta E/E \approx 1000$ at 8keV) necessary for resolving spectral features such individual ion contributions in the L shell of Au.

The spectrometer used in all measurements consisted of a 4cm long cylindrically bent piece of mica with a radius of curvature of 4cm. Mica has moderate reflectivity compared to other crystals like LiF and HOPG, but it can be used efficiently in odd orders without a significant drop in reflectivity. The crystal was used in the 3rd order and all measurements used image plate (Fujifilm BAS MS) which are insensitive to the large electromagnetic pulses generated by the laser matter interaction. Figure 2.5 shows the setup for 7.4-7.8keV which is calculated to have a source to line distance of 31.5cm to 33cm. The setup of this crystal spectrometer is easy as the source and image plane are set on a straight line with the crystal parallel to the image plane and offset from the line by its' radius of curvature. In order to focus the crystal on the image plane, the crystal is scanned several mm in both direction until it is focused to a thin line on the image plane. Line width measurements of the K- α of Ge ($h\nu = 9855\text{eV}$) were found to be 8eV FWHM, suggesting the mica Von Hamos spectrometer had a $E/\Delta E$ of ≈ 1000 .

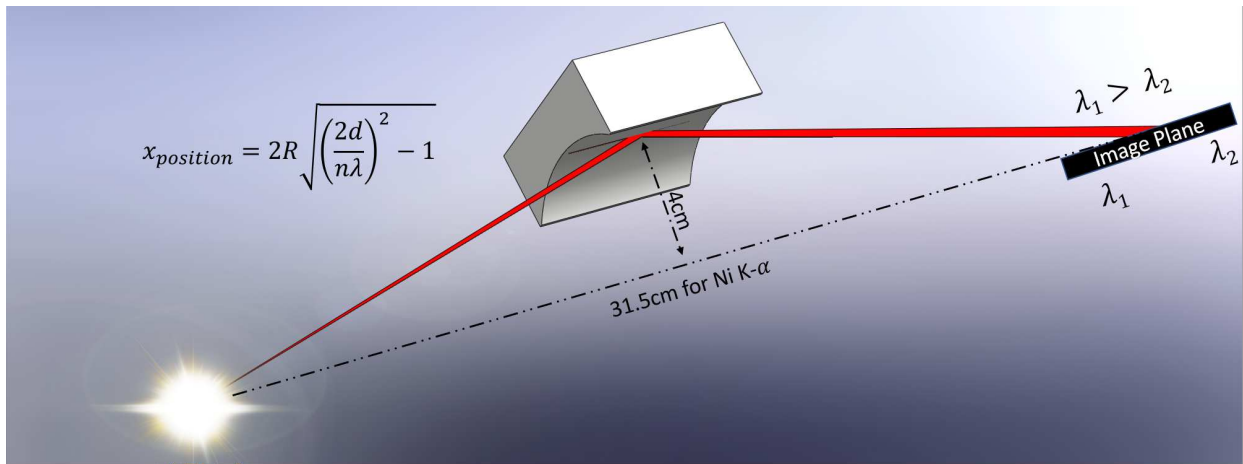


Figure 2.5: Von Hamos crystal spectrometer using a cylindrically bent mica crystal ($2d=19.84\text{\AA}$) with a radius of curvature of 4cm. Higher energy, shorter wavelength x-rays are closer to the crystal. The source is on the left.

2.5 Nanowire Fabrication

Large area ($>1\text{cm}^2$), high aspect ratio ($>100:1$) metal nanowire arrays exhibiting high degrees of alignment have been fabricated at Colorado State University. These targets are grown by de-

positing several hundred nm of gold onto one side of an anodic alumina oxide (AAO) template to create an electrical contact followed by electrochemical deposition of a metal into the template shown in Figure 2.6, allowing any metal that is easily plated to be used in the synthesizing process [46]. Metals have been successfully used as nanowires: cobalt, copper, nickel, rhodium, ruthenium, palladium, silver and gold. By changing the parameters of the commercially available AAO templates, it is possible to vary the nanowire array parameters in three different ways:

- 1) The diameter of the wires can be changed from 35nm to 250nm
- 2) The interwire spacing of the wires can be changed defining the average densities corresponding to a fraction of solid density ranging from as low as 3% to as high as 35%
- 3) The length of the wires can be varied from less than 1 μm to up to 50 μm , the thickness of the template.

This provides a large parameter space for fabricating targets of different characteristics. These are used for interesting experiments such as measuring the gap closure time in Chapter 3 as well as measuring the x-ray conversion efficiency for different metals and different wire diameters in Chapter 2.

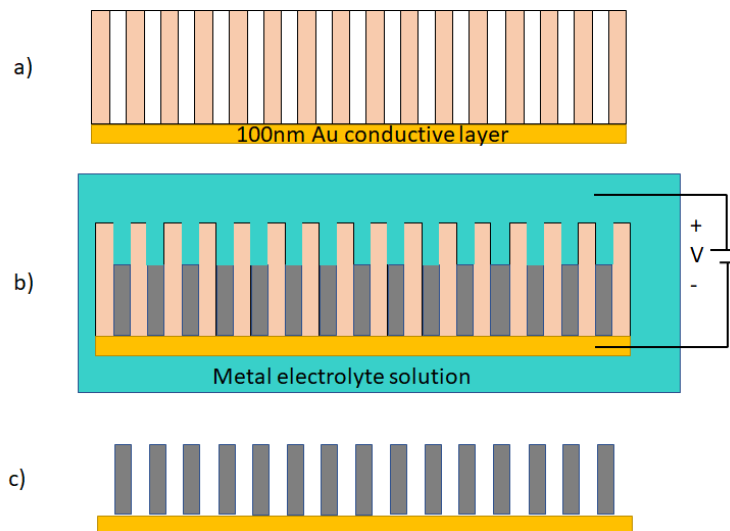


Figure 2.6: a) a 100nm thick layer of Au is deposited on one side of the template. b) Metal is deposited electrochemically into the AAO porous template. c) The template is dissolved, leaving the nanowires remaining.

Following the deposition of the metal shown in Figure 2.6, the template is dissolved in concentrated NaOH to expose the wire array. At this point, bringing the nanowire array out of solution would cause the nanowires to bunch and form "haystacks" due to the surface tension of the fluid. To prevent this bunching the wire arrays were dried in a supercritical CO₂ environment. This allows the drying process to move from the liquid phase of CO₂ through the supercritical phase of CO₂ (1073psi at room temperature) and then finally to the gas phase which exhibits no surface tension [47]. This process ensures that the nanowire array remains aligned and the gaps between the wires are consistent.

Chapter 3

Efficient picosecond x-ray pulse generation from plasmas in the radiation dominated regime¹

Overview: The efficient conversion of optical laser light into bright ultrafast x-ray pulses in laser created plasmas is of high interest for dense plasma physics studies, material science, and other fields. However, the rapid hydrodynamic expansion that cools hot plasmas has limited the x-ray conversion efficiency (CE) to 1% or less. Here we demonstrate more than an order of magnitude increase in picosecond x-ray CE by tailoring near solid density plasmas to achieve a large radiative to hydrodynamic energy loss rate ratio, leading into a radiation loss dominated plasma regime. A record 20% CE into $h\nu > 1\text{keV}$ photons was measured in arrays of large aspect ratio Au nanowires heated to keV temperatures with ultrahigh contrast femtosecond laser pulses of relativistic intensity. The potential of these bright ultrafast x-ray point sources for table top imaging is illustrated with single shot flash radiographs obtained using low laser pulse energy. These results will enable the deployment of brighter laser driven x-ray sources at both compact and large laser facilities.

3.1 Introduction

Intense ultrashort bursts of x-ray radiation are essential for backlighting the implosion of capsules in inertial confinement fusion experiments [48, 49]. They are also of significant interest for fundamental studies that include laboratory opacity measurements in matter at the conditions of stellar interiors [50], and for probing ultrafast changes in material with high spatial and temporal resolution [51, 52]. Dense plasmas produced by laser irradiation of solid density materials with intense femtosecond laser pulses are emitters of intense x-ray pulses. However, different factors

¹R. Hollinger et al "Efficient picosecond x-ray pulse generation from plasmas in the radiation dominated regime" Optica, vol. 4, no. 11, p. 1344, 2017.

contribute to limit the CE into ultrafast x-ray pulses. First, only a fraction of the laser energy is absorbed by the plasma. Second, the radiation typically originates from a shallow plasma volume whose rapid expansion results in hydrodynamic cooling rates that exceed the radiation cooling rate. The result is poor conversion efficiency. Efforts to increase the ultrafast x-ray yield have largely focused on addressing the first of these two limitations by improving the coupling of the laser energy into the material using structured targets. Targets investigated include micro-lithographic gratings [33, 36, 37], nanometer size dielectric spheres or ellipsoids [14, 35], "smoked" clustered surfaces [13, 33, 34], and nanowire arrays [11, 13, 15, 38, 39]. Increased CE with respect to flat solid target have been reported [11, 13, 34, 36, 38, 39, 53]. In the case of nanowires, the increased x-ray yield was often adjudicated to increased absorption [13, 38], including enhanced absorption due to a "lightning rod effect" that increases the number of hot electrons as a result of an enhancement of the electric field at the tip of nanostructures [39, 53]. Kulcsar et al. suggested several causes in addition to increased absorption, including a larger number of heated atoms [13]. However, the CE into $h\nu > 0.9$ keV x-rays was limited to ≈ 0.1 percent, a value similar to that obtained using smoke targets. In all the experiments with different types of nanostructured targets the x-ray CE into $h\nu > 1$ keV photons has remained less than 1 percent, in spite of the increase in energy coupling. This CE into picosecond x-ray pulses is significantly lower than that achieved in converting laser light into nanosecond x-ray pulses in underdense (gas, cavity and pre-exploded foil) plasmas [54–58].

3.2 Creating favorable conditions for high x-ray conversion efficiency

In this letter we show that an increase of more than an order of magnitude in optical to picosecond x-ray CE can be achieved by tailoring the plasma characteristics to reach a smaller radiative cooling time, τ_{rad} , than the hydrodynamic cooling time, τ_{hydro} , resulting in a larger radiative to hydrodynamic cooling rate ratio that effectively overcomes hydrodynamic cooling. The radiative cooling time is here defined as the time needed to radiatively dissipate the thermal energy of the plasma. In the simple case of an ideal plasma with ions of average charge Z , this characteristic time

can be expressed as the ratio of the kinetic energy of free electrons to their rate of radiated energy loss by collisions: $\frac{3ZkT_e}{2E} \frac{1}{\langle \sigma v \rangle n_e}$ where σ is the effective electron collision cross section for all three major radiative processes (line radiation, photorecombination and bremsstrahlung) T_e, n_e are the electron temperature and density, and E is the average energy radiated per collision event. The hydrodynamic cooling time is defined here as $\frac{\Delta L}{C_s}$, where ΔL is plasma size and C_s is the acoustic velocity. Considering that within the range of high electron densities and high temperatures of interest for x-ray generation τ_{rad} is inversely proportional to the electron density dependent total collision rate $\langle \sigma v \rangle n_e$ and τ_{hydro} is proportional to the plasma size ΔL , this condition requires a large electron density and/or large plasma size such that:

$$\tau_{rad} \propto \frac{1}{\langle \sigma v \rangle n_e} < \frac{\Delta L}{C_s} \propto \tau_{hydro}$$

We experimentally demonstrate that this approach results in a $\approx 20\%$ CE of optical laser light into $h\nu > 1\text{keV}$ x-rays in 4π sr, more than an order of magnitude increase in CE with respect to previous work. We fulfilled the above inequality by volumetrically heating supercritical density plasmas by irradiating arrays of high aspect ratio Au or Ni nanowires at an intensity of $I = 4 \times 10^{19} \text{ Wcm}^{-2}$ with ultrahigh contrast femtosecond laser pulses. The interaction was tailored to simultaneously achieve deep volumetric heating (large ΔL) to multi-keV temperatures, and plasma densities on the order of 100 times the critical density in which the collisional rates are greatly increased with respect to plasmas generated from solid targets.

3.3 Methods

The experiments were conducted by irradiating arrays of free-standing, vertically aligned Au and Ni nanowires with diameters of 55nm, 80nm, or 100nm and 4-6 μm in length. The laser beam impinged parallel to the nanowire axis, normal to the nanowire array target surface. The nanowire arrays were synthesized by electrodeposition into anodic aluminum oxide templates [46]. The nanowires were grown with an average density of 12% solid density for the targets composed of

55nm or 80nm diameter nanowires, and 15% of solid density for the 100nm diameter nanowire targets. After dissolving the template an array of ordered, high aspect ratio ($\approx 50-100:1$) nanowires is exposed. This corresponds to an interwire spacing of 85nm and 130nm for the 55nm and 100nm diameter wire arrays respectively. Each nanowire target was imaged using a scanning electron microscope. The nanostructured targets were irradiated by ultrahigh ($>10^{12}$) contrast $\lambda=400$ nm pulses of ≈ 55 fs duration with energy up to 1 joule from a frequency doubled Ti:Sapphire chirped-pulse-amplification (CPA) laser. The laser consists of a conventional front end followed by 3 Ti:Sapphire power amplifiers pumped by Nd:glass slab lasers designed to operate at up to 5 Hz repetition rate [59]. The beam was expanded to 9cm and the pulses were compressed using a gold grating vacuum compressor. Frequency doubling in a 0.8mm thick Type I KDP crystal with an efficiency of 40-50 % greatly improves the contrast as the second harmonic generation process is proportional to the square of the intensity. The duration of the frequency doubled pulse was measured in a single shot self-diffraction autocorrelator. The wavefront was corrected with a deformable mirror (Imagine Optic). The high contrast pulses were focused onto the target by a 90 degree off axis parabolic mirror with a 15.4cm focal length, resulting in a spot size of $\approx 4.5 \mu\text{m}$ to obtain an intensity of $\approx 4 \times 10^{19} \text{ Wcm}^{-2}$. The angular distribution of the x-ray emission was measured using an array of four filtered Si photodiodes mounted at equally spaced polar angles on a 28cm radius circular rail centered on the laser beam focus where the target was placed. Polished Ni or Au flat solid targets were shot immediately preceding each nanowire target shot for comparison. The diodes were placed on a plane that forms an angle of 20 degrees with respect to the plane of incidence. Magnet pairs were placed in the front of each of the photodiode to deflect electrons up to 6 MeV energy away from the diodes. It was verified that increasing the magnetic field strength by 2X and the length of the magnets by the same factor did not change the photodiode signals, ensuring that the photodiode/filter assembly is in practice only detecting x-rays. The spectrally resolved x-ray emission was simultaneously recorded using a von Hamos mica crystal spectrometer and a front illuminated CCD. Time integrated spectral emission of the plasmas showed He-like Ni ion lines which dominate over the characteristic $K\text{-}\alpha$ emission by over an order of magnitude.

3.4 Results and Discussion

Figure 3.1 illustrates a particle-in-cell simulation (PIC) of the electron temperature and electron density evolution in an array of Au nanowires at three different times after the laser pulse. The array is composed of wires 55 nm diameter with an average density corresponding to 12% of solid density and the laser pulse has a 55 fs FWHM duration. The simulation was conducted using the fully relativistic 3-D PIC code Virtual Laser-Plasma Laboratory (VLPL) [41]. In contrast to flat solid targets, where a thin plasma layer is heated, in nanowire arrays the ultrafast laser pulses propagate several micrometers within the inter-wire gaps. The heated nanowires explode creating a thick plasma layer of nearly solid density, reaching $\approx 4 \times 10^{23} \text{ cm}^{-3}$ 311 fs after the peak of the laser pulse while the electron temperature is $\approx 15 \text{ keV}$ (Figure 3.1c,f). Later the plasma cools, but 1ps after the peak of the laser pulse the temperature still remains at a few keV.

To illustrate the major radiative differences between a flat solid target and a volumetrically heated nanowire array Figure 3.2 shows the computed x-ray radiation power density spatial distribution as a function of time up to 10ps after the laser pulse. The simulations are the result of hydrodynamic model computations with transient atomic kinetics in which the VLPL PIC code was used to simulate the first stages of nanowire plasma formation until the nanowires are fully dissolved. Both targets are assumed to be irradiated with an intensity of $4 \times 10^{19} \text{ Wcm}^{-2}$. It is shown that irradiation of the Au nanowire array results in both a large increase in the radiating volume, and a larger emitted power density. In the case of the flat solid target most of the x-ray emission takes place in a very thin supercritical layer heated by conduction, where acceleration and expansion cooling takes place with the plasma density rapidly dropping orders of magnitude in one micron. The much larger heated plasma depth in the nanowire plasma greatly increases the plasma hydrodynamic cooling time. Simultaneously, the larger plasma density results in increased electron collisional excitation rate, leading to a shorter radiative cooling time.

The magnitude of these effects is quantitatively illustrated in Figure 3.3 by atomic kinetic calculations that compare the characteristic radiative and hydrodynamic cooling times of a Au flat target plasma and a Au nanowire array plasma. The computations were conducted with the hy-

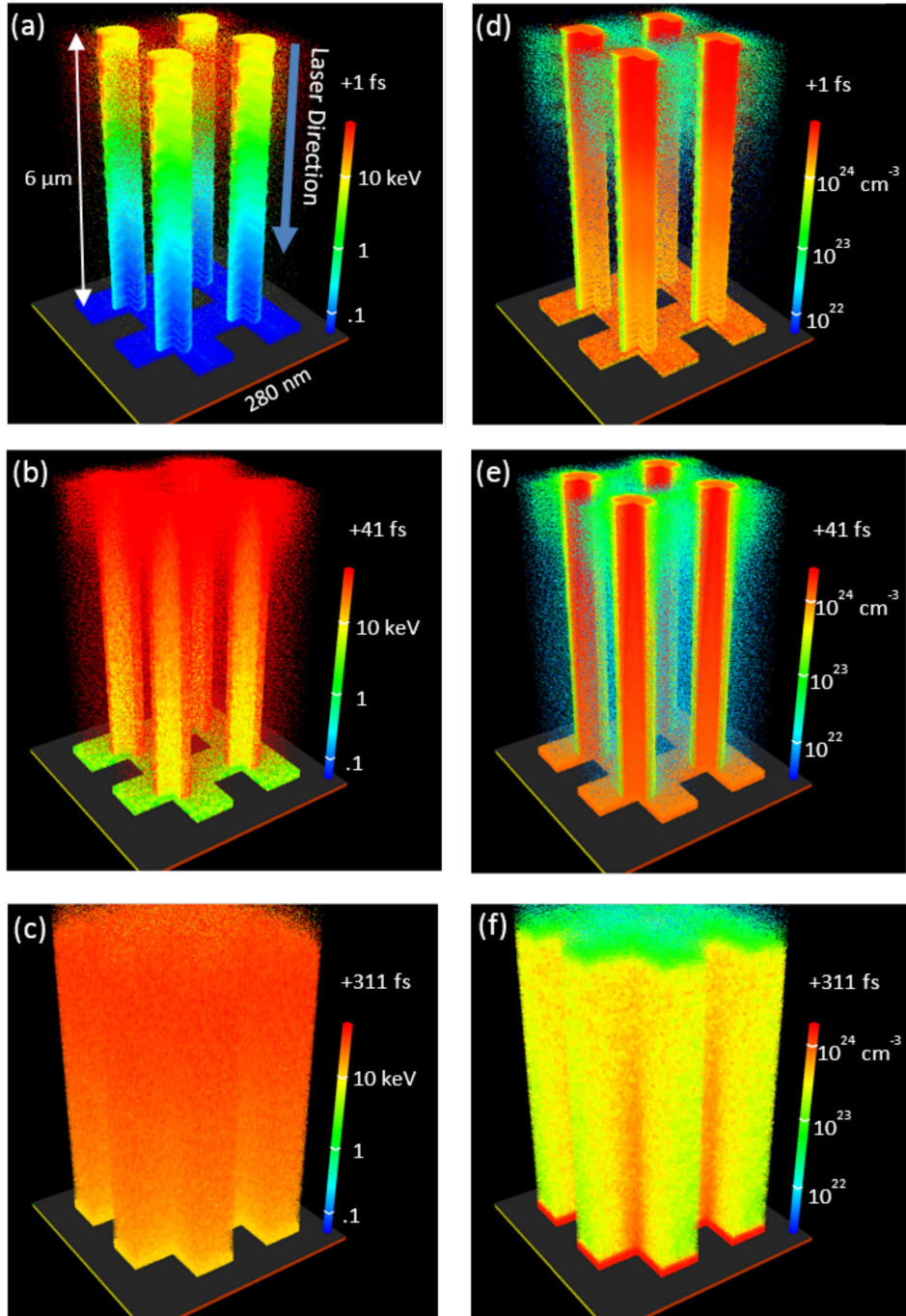


Figure 3.1: (a-c) PIC simulation of the electron temperature distribution in a 55 nm diameter Au nanowire array irradiated by a $\lambda = 400$ nm laser pulse of 55 fs duration at an intensity of $4 \times 10^{19} \text{ Wcm}^{-2}$ at three different times after the laser pulse. (d-f) shows the corresponding electron density maps.

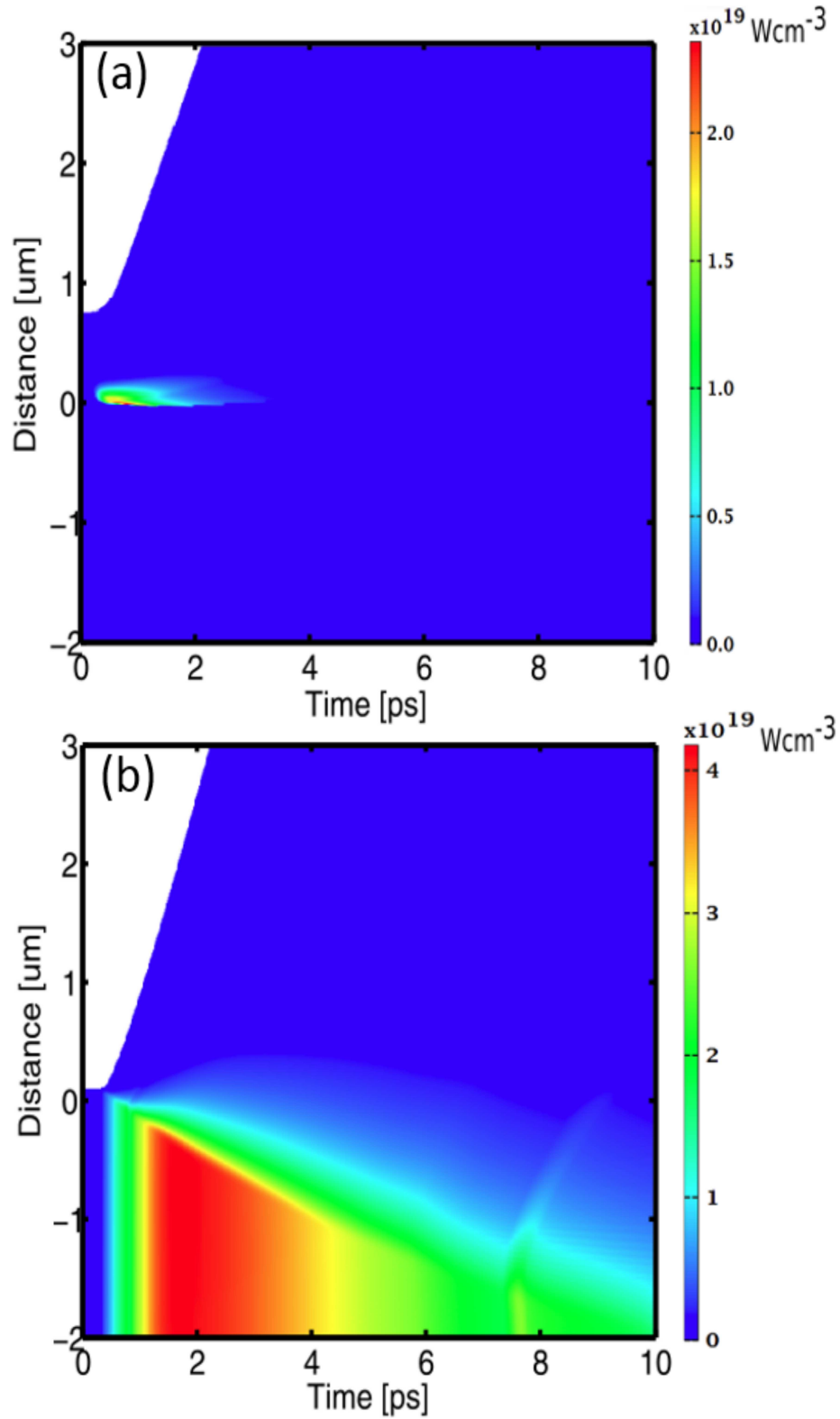


Figure 3.2: Computed evolution of the x-ray radiation power for a Au flat target (a), and a Au nanowire target (b), both irradiated at an intensity of $4 \times 10^{19} \text{ Wcm}^{-2}$ with a 55 fs FWHM pulse. The array of nanowires is assumed to be composed of 55nm diameter wires with an average density of 12% solid. Time is measured with respect to the peak of the laser pulse, and the distance is in the direction normal to the target surface.

hydrodynamic/atomic physics code Radex [60] Figure 3.3a shows the cooling times for a Au plasma with a density of $n_e=6 \times 10^{22} \text{ cm}^{-3}$ and a thickness of $0.2 \text{ }\mu\text{m}$. These are the typical parameters of the x-ray emitting layer computed by both PIC and hydrodynamic models for plasmas created irradiating a solid Au target. Both models give similar source thickness values in spite of the fact that RADEX is approaching the validity limit of the hydrodynamic approximation. In this case the great majority of the laser energy is lost in the hydrodynamic expansion before collisions have time to convert the electron kinetic energy into radiation. For the electron temperatures of interest the hydrodynamic cooling time is much shorter than the radiative cooling time, resulting in a small CE. This result is in contrast to Figure 3.3b for a supercritical Au plasma with a density of $n_e = 4 \times 10^{23} \text{ cm}^{-3}$, a value approaching 100 times the critical density, typical of the conditions resulting from irradiating the nanowire arrays with the intensity we used in the experiments. In this case the radiative cooling time is smaller than the hydrodynamic cooling time, leading to greatly increased radiation efficiency. For larger average density nanowire arrays irradiated at increased intensities, even higher electron densities will result [10], further driving the plasma into a radiation loss dominated regime.

The large increase in CE we report here is made possible by selecting a combination of irradiation and target parameters designed to achieve the condition in equation (1). First, we use ultrahigh contrast $>10^{12}$ laser pulses that avoids destroying the nanowires and establishing a critical density layer before the main pulse arrives. Second, we use short laser pulses (55 fs) that allow for nearly all of the laser energy to be deposited deep into the array before the nanowires explode and close the interwire gap, forming a continuous critical density surface. After this time no further efficient coupling of the laser energy can occur into the volumetrically heated plasma. Third, the use of long nanowires allows for volumetric heating to occur to depths of $4\text{-}5 \mu\text{m}$ [27], increasing the hydrodynamic expansion time. Fourth, we use dense arrays, in which the plasma density reaches nearly 100 times the critical density which results in high collisional rates and consequently in very short radiative cooling times. Fifth, we use relativistic irradiation intensities that heat the plasmas to multi-keV temperatures deep into the array, which leads to a high degree of ionization [16], an

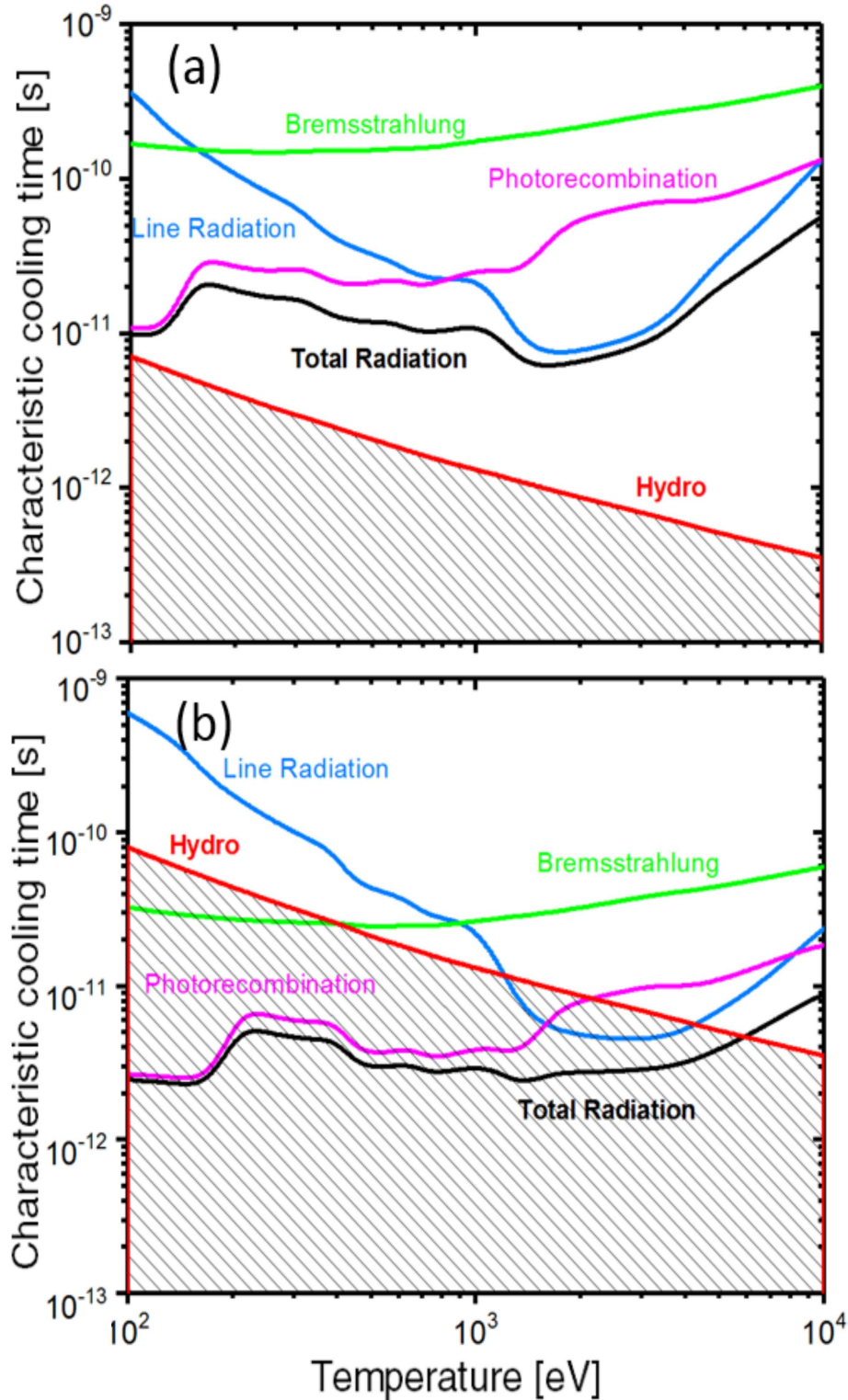


Figure 3.3: Comparison of radiative and hydrodynamic cooling times as a function of electron temperature for two different Au plasmas with the characteristics corresponding to the x-ray emitting region of: (a) a flat solid target, $n_e = 6 \times 10^{22} \text{ cm}^{-3}$, plasma size $L = 0.2 \mu\text{m}$, and (b) a nanowire array plasma $n_e = 4 \times 10^{23} \text{ cm}^{-3}$ and plasma size $L = 4 \mu\text{m}$. The total radiation time is the effective radiative cooling time computed from the photorecombination, bremsstrahlung and line radiation rates

increased electron density, and a decreased radiation lifetime. This simultaneous set of conditions differs from those in previous experiments that measured x-ray yield from nanowire targets. Prior work used either picosecond pulses [12], short wires [12,14], relatively low contrast pulses [12-14] or non-relativistic intensities [11-14]. This limited the radiation fraction obtained for $h\nu > 1$ keV to values nearly two orders of magnitude smaller than that we report here. For photon energies $h\nu > 1$ keV both Au and Ni nanowires display a convex angular emission profile with maximum intensity in the direction normal to the target (Figure 3.4), resulting from increased opacity in the periphery of the plasma.

The increase in x-ray flux, the small source size of ≈ 5 μm deduced from the penumbra in a knife edge test, and the ps pulse duration makes these plasmas an excellent x-ray point source for time resolved flash radiography. To illustrate this we conducted a single shot radiography experiment of a wasp's knee. Figure 3.6b compares a single shot radiograph taken irradiating an array of 100nm diameter Ni nanowires with 15% solid density to that obtained irradiating a flat Ni solid target with a similar laser pulse (Figure 3.6a). The radiograph taken with the nanowire target shows that a single laser shot with a laser pulse energy of only 25mJ on target is sufficient to produce a detailed image. In comparison the image obtained with the flat Ni target shows insufficient flux and would require over an order of magnitude more shots to obtain a similar image.

Integration of these emission profiles over a hemisphere gives us the total x-ray yields shown in Figure 3.5. Comparison of the x-ray CE for Au and Ni nanowire array targets of different wire diameters show that the x-ray emission is higher for Au. CE is defined here as the ratio of the measured x-ray energy for photons $h\nu > 1$ keV (or > 6 keV) emitted into 4π sr. divided by the laser drive energy impinging onto the target. The highest yield corresponds to targets with 80nm diameter Au nanowires, with an average CE of 18% and individual shots reaching values up to 22% in 4π sr Figure 3.5a. This CE for $h\nu > 1$ keV exceeds the highest reported values reported using any type of target by more than an order of magnitude [6] and those reported for nanowire targets by two orders of magnitude [12]. Figure 3.5b compares the $h\nu > 6$ keV plasma emission from Au

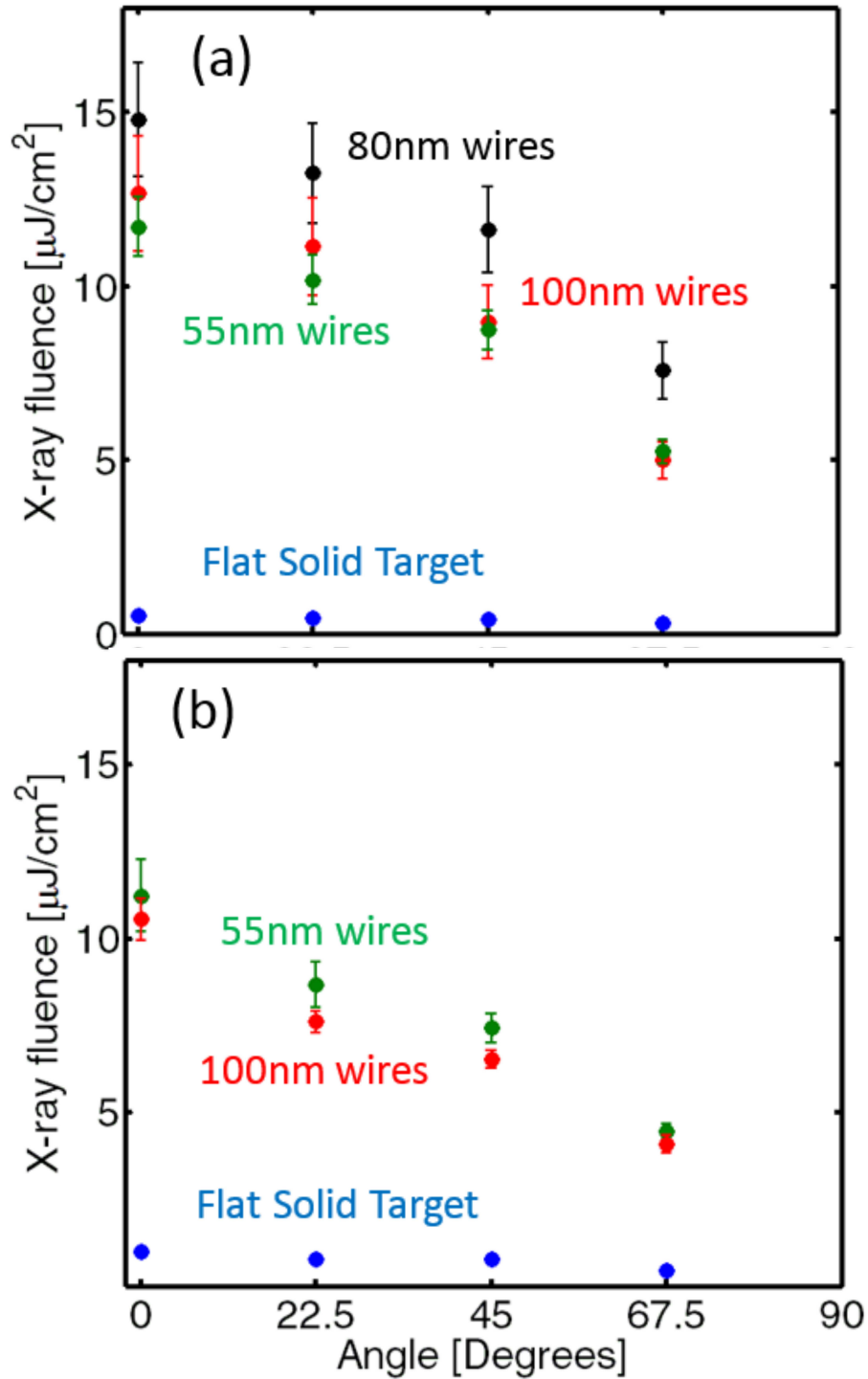


Figure 3.4: Measured angular distribution of the x-ray fluence on each diode from nanowire arrays at photon energies > 1 keV for (a) Au and (b) Ni nanowire targets of different nanowire diameters. Measurements for flat solid targets of the same materials are included for comparison. The irradiation intensity was $4 \times 10^{19} \text{ Wcm}^{-2}$. Error bars correspond to one standard deviation. Fluctuations in x-ray CE result mostly from irregularities and imperfections in the ordered wire array. The angle is measured with respect to the normal to the target surface.

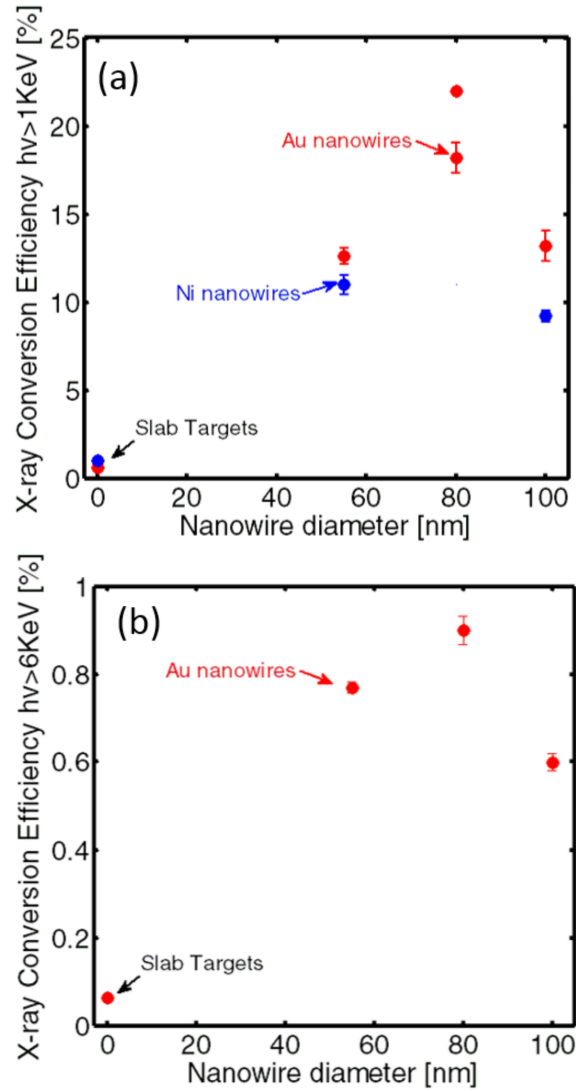


Figure 3.5: (a) X-ray CE ($h\nu > 1\text{keV}$) for Au and Ni nanowires arrays of different wire diameters compared to flat solid targets of the same material. $I=4\times 10^{19}\text{ Wcm}^{-2}$. The values are averages of 10 shots. Error bars correspond to one standard deviation. The maximum measured single shot CE for 80 nm diameter wires exceeded 22% in 4π sr which is represented by the point without an error bar. This yield corresponds to an increase of 35x with respect to a polished flat target; (b) CE into $h\nu > 6\text{keV}$ x-rays. An enhancement of 14x in x-ray emission is observed compared to flat targets.

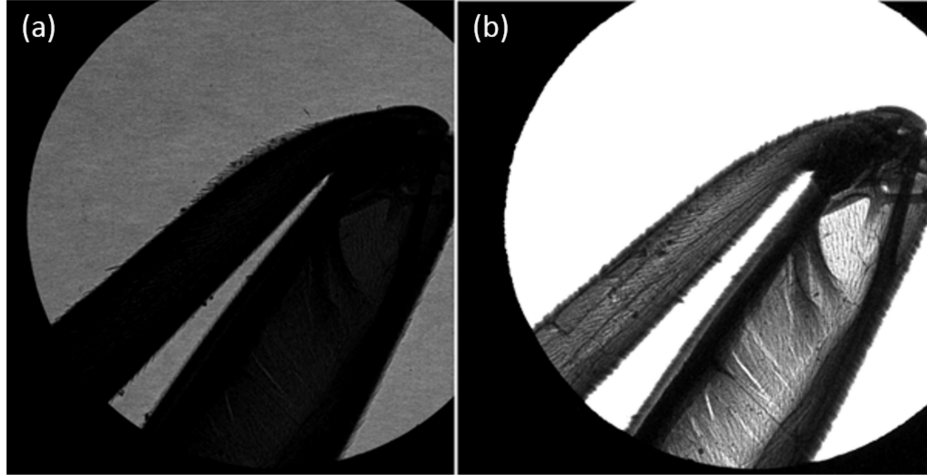


Figure 3.6: Single shot radiograph of a wasp’s knee using the x-ray flash emitted from: (a) a flat Ni target, and (b) an array of 100nm Ni nanowires. A $13\mu\text{m}$ Be filter was used to block photons of $h\nu < 1\text{keV}$. The sample was placed at 4 cm from the plasma and a CCD array was placed at a distance of 35cm from the sample leading to an effective magnification of 8.75x with a field of view of $425\ \mu\text{m}$. Both images are plotted on the same intensity scale. The laser energy on target was 25mJ.

nanowire targets of different nanowire diameters to that from a Au foil target irradiated with the same pulses. At these energies, the active region of the Si detector starts to become transparent to the radiation. We corrected the measured photodiode signal for the $50\mu\text{m}$ thickness of the Si detector active region, and also for the energy dependency of the filter transmissivity. For the latter, since model simulations show there is no line radiation above 6 keV for these transient Au plasmas, we assumed the spectral distribution is that resulting from bremsstrahlung plus photorecombination. This continuum radiation was calculated using the electron energy distribution computed by PIC simulations. With these corrections the 80nm Au nanowire targets are estimated to radiate at $h\nu > 6\ \text{keV}$ with a CE that exceed 0.8% in $4\pi\ \text{sr.}$, an increase of 14 times over Au foils irradiated by the same laser pulses.

3.5 Conclusion

In conclusion, we have demonstrated that the CE of optical laser pulses into picosecond x-ray pulses can be greatly improved by increasing the radiative to hydrodynamic energy loss rate ratio in volumetrically heated supercritical density plasmas. By tailoring nanostructured targets irradiated

at relativistic intensities to fulfill this condition we have generated ultrafast pulses of $h\nu > 1\text{keV}$ photons with a record efficiency of $\approx 20\%$ into 4π sr. This increase of more than an order of magnitude in the efficient generation of picosecond line and continuum x-ray radiation will open new opportunities in flash radiography including the backlighting of imploding capsules in laser fusion experiments, in opacity measurements of matter at the conditions of stellar interiors, and in table-top applications requiring intense picosecond flashes of x-rays. Furthermore, the results will also motivate more efficient x-ray generation experiments at larger laser facilities.

Chapter 4

Energy deposition dynamics of highly relativistic femtosecond laser pulses into nanowire array plasmas

Overview: The efficient coupling of relativistic intensity laser pulses into dense aligned nanowires arrays can result in near solid density plasma volumetrically heated to multi-keV temperature, producing record x-ray yields, multi-MeV ion energies, and quasi-monoenergetic neutron bursts. To scale this approach to highly relativistic intensities, $>1 \times 10^{21} \text{ Wcm}^{-2}$ as well as high energy facilities typically characterized by longer pulse durations, it is necessary to ensure that the gap between the individual wires remains open during the laser pulse. The formation of a critical electron density between the wires will prevent any further laser heating of the nanowire structure. This chapter presents results of dual pump pulse experiments that demonstrate highly relativistic intensities ($a_0 \approx 11$) can couple their energy efficiently into arrays of 100nm diameter Ni nanowires with 24% of solid density for up to 100fs after the initial laser pulse.

4.1 Introduction

Irradiation of nanowires with high contrast, femtosecond pulses with intensities less than $5 \times 10^{19} \text{ Wcm}^{-2}$ was shown to create multi-keV temperature near solid density plasmas that several μm deep [10, 11]. Experiments have shown that these vertically aligned nanowire arrays plasmas yield striking enhancements in x-ray conversion efficiency in comparison to solid density targets [13, 14, 39, 61] reaching 20% in 4π for $h\nu > 1 \text{ keV}$ photons [12]. Nanowire arrays have generated a $>500\text{x}$ increase in neutron production from deuterated nanowires [18], and greatly enhanced hot electron yields [16, 17]. These nanostructure targets also constitute a possible pathway

to creating astronomically relevant ultra-high energy density plasmas in a laboratory when irradiated with different laser pulse durations ranging from tens of femtoseconds to a few picoseconds.

An intrinsic advantage of these aligned nanostructures is their ability to effectively trap and absorb laser energy deep into the array, which volumetrically heats their solid density to multi-keV temperatures. However, the timespan for efficient energy deposition is limited. The critical parameter for the realization of this efficient laser matter interaction is the time scale in which the nanowires explode and fill the interwire gaps with a super critical plasma which inhibits significant further laser energy coupling deep into the array. This is the key parameter described here: the gap closure time. The intense laser pulse extracts electrons from the nanowire, creating a charge separation in which the associated Coulomb force accelerates the ions radially outward, helping to close the interwire space and absorb the laser radiation. In addition, due to the high solid density of the wires, the electrons quickly heat ionize to He-like and H-like Ni. As a result, very high pressure develops within the heated wires causing a rapid hydrodynamic expansion that causes the wires to explode and fills the gaps with an overdense plasma. Three dimensional particle in cell simulations suggest that at the laser intensities investigated in this work, the latter effect is the one that dominates the dynamics of the gap closure, determining the gap closure time. Its knowledge allows tailoring of the nanowire geometry, in particular the interwire distance, to achieve maximum coupling of the laser pulse into the nanostructure for a given laser pulse duration.

Understanding the gap closure dynamics is critical for utilizing nanowire targets with various types of laser pulse for different applications. The gap closure time, which has never been measured experimentally, can in principle be approximated by the ratio of the gap between the nanowires divided by the acoustic velocity, C_s , at which the heated wires can be estimated to expand:

$$C_s = \sqrt{\gamma Z k_b T_e / m_i} = 9.79 \times 10^3 \sqrt{\gamma Z T_e / \mu} \quad [m/s]$$

where γ is the adiabatic index, Z and m_i are the ion charge state and mass, k_b is the Boltzmann constant, T_e [eV] is the electron temperature and μ is the ion mass to proton mass ratio. Particle in

cell (PIC) simulations estimate that irradiation with 45 fs FWHM duration pulses with an intensity of $1 \times 10^{21} \text{ Wcm}^{-2}$ 100 nm diameter nanowires will heat to a temperature of 10 keV by the end of the laser pulse. For such an initial wire temperature, the wires should in principle expand at a velocity of 840 km/s. This would result in a gap closure time of ≈ 50 fs for wires with an interwire gap of 85nm. Here we report results of experimental measurements that show that highly relativistic laser light is able to couple 100 fs after the initial heating of the array.

4.2 Measurement of efficient coupling into near solid density nanowire arrays

In order to measure the time available for efficient energy coupling, we irradiated nickel nanowire arrays using a dual pulse sequence as illustrated in Figure 4.1. In this approach, the laser pulse energy is separated into two equal pulses while adjusting the temporal delay between them.

The two pulses were developed separating the seed pulse from the laser oscillator using a polarizer and a polarizing cube beamsplitter, and the time delay between the two pulses was controlled with a retroreflector mounted on a delay stage accurate to $\pm 0.4 \mu\text{m}$ corresponding to 1.3fs error in time. The two beams were subsequently recombined and sent through the Ti:Sapphire amplifier chain. A second harmonic generation frequency resolved optical gate (FROG) was used to measure ratio of the energy of the pulses after amplification to 200mJ. To ensure the pulses contained equal energy after amplification, it was necessary to tune the polarizer and thus the ratio of the split seed pulses by observing when the auto-correlation traces had 50% energy in the side lobe of the auto-correlation. The temporal coherence time of the laser is defined as $\tau_{coherence} = \lambda^2 c / \Delta\lambda$ yielding 84fs for a beam operating at a central wavelength of 800nm with a bandwidth of 40nm FWHM. Therefore, the minimum intrapulse delay was limited to 100fs so that it was larger than the coherence time to avoid interference between the two pulses. Past this time delay, the delay stage was moved in increments of $7.5 \mu\text{m}$ corresponding to temporal delays of 50fs when accounting for a double pass.

As a signature of gap closure and energy coupling efficiency we monitored two physical quantities: the intensity of the He- α resonant line in a Ni plasma and the overall plasma emission at photon energies > 1 keV. We conducted experiments that show that the presence of strong He- α emission is a good indicator of the efficiency with which the second pulse couples its' energy into the array. When the intrapulse delay exceeds the gap closure time, the second pulse encounters a supercritical density plasma that fills the gaps between the wires by which is significantly reflected, not letting it contribute to the volumetric heating of the nanowire array. At the lower irradiation intensities the light is absorbed into a near critical density region of the plasma, typically 0.1% of solid density, and is not efficiently converted into x-rays [12]. In contrast to this, when the two pulses irradiating the nanowires have an intrapulse delay shorter than that of the gap closure time, the second pulse can propagate deep into the wire array further heating the plasma which leads to an increase in the He-like ion line emission and the overall x-ray photon yield. To qualify the intensity of He- α line as an accurate gauge of energy coupling, an energy scan was conducted which shows there is a linear relation between the energy of a single 45 fs pulse impinging into the nanowire array target and the line intensity shown in Figure 4.2. As a second gauge of the energy coupling we monitored the spectrally integrated x-ray emission of photons with energy > 1 keV, for which again a linear relation with laser pulse energy impinging of target was verified for the range of intensities of interest.

The scheme is sensitive to the contrast of the laser system as any significant pre-pulse would ablate the nanowire arrays and create a plasma preceding the arrival of the main pulse, disrupting the measurement. Therefore, very high laser contrast is required. Pulses from the CSU petawatt class, chirped pulse amplification Ti:Sapphire laser were frequency doubled in a potassium diphosphate crystal to achieve a contrast $> 1 \times 10^{12}$ [42]. An f/2 off axis parabola was used to focus the two collinear high contrast $\lambda=400$ nm laser pulses onto nearly diffraction limited focal spot onto to the target [11]. Each laser pulse contained up to 2.5 J of energy and had a 45 fs FWHM duration, resulting in a FWHM intensity of 1×10^{21} Wcm $^{-2}$ ($a_o \approx 11$). It was confirmed that the individual pulses were overlapped by monitoring the focal spot and blocking each of the pulse arms.

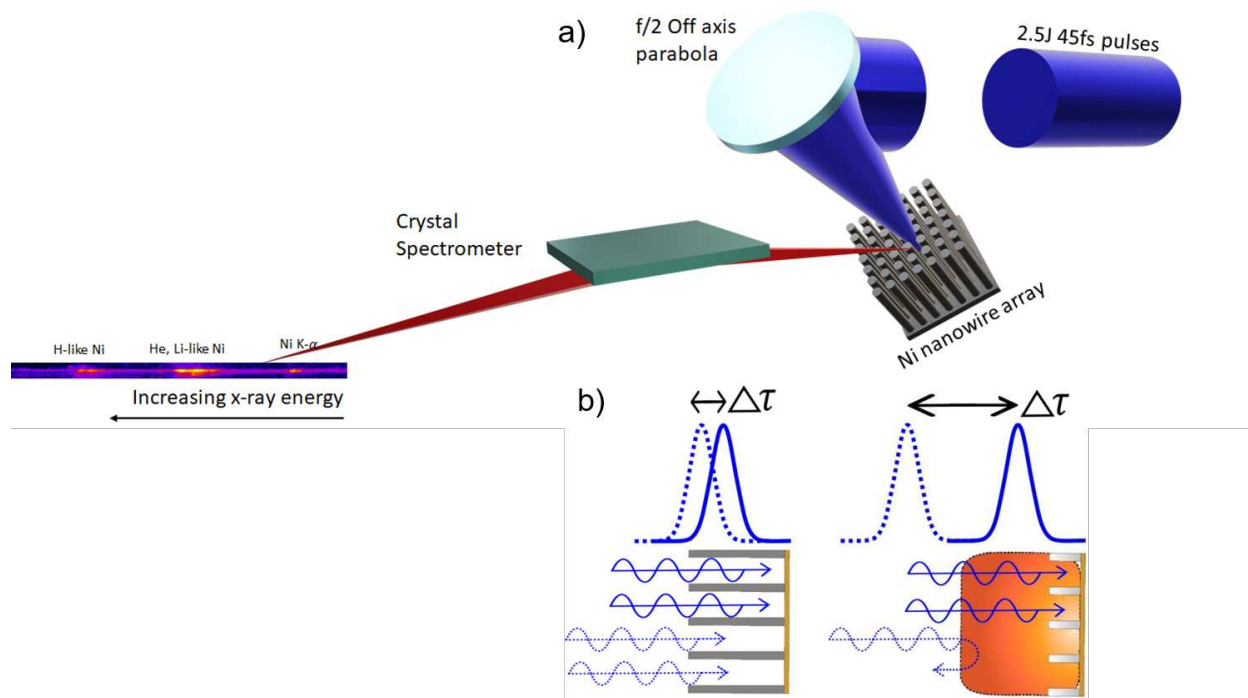


Figure 4.1: a) Two 2.5J, 45fs high contrast laser pulses are focused into a Ni nanowire array using an $f/2$ off axis parabola. The delay between the pulses is varied while observing changes in the ionized K shell emission of Ni. b) A schematic of the laser entering the nanowire array for: 1) $\Delta\tau$ less than the gap closure time and 2) $\Delta\tau$ larger than the gap closure time.

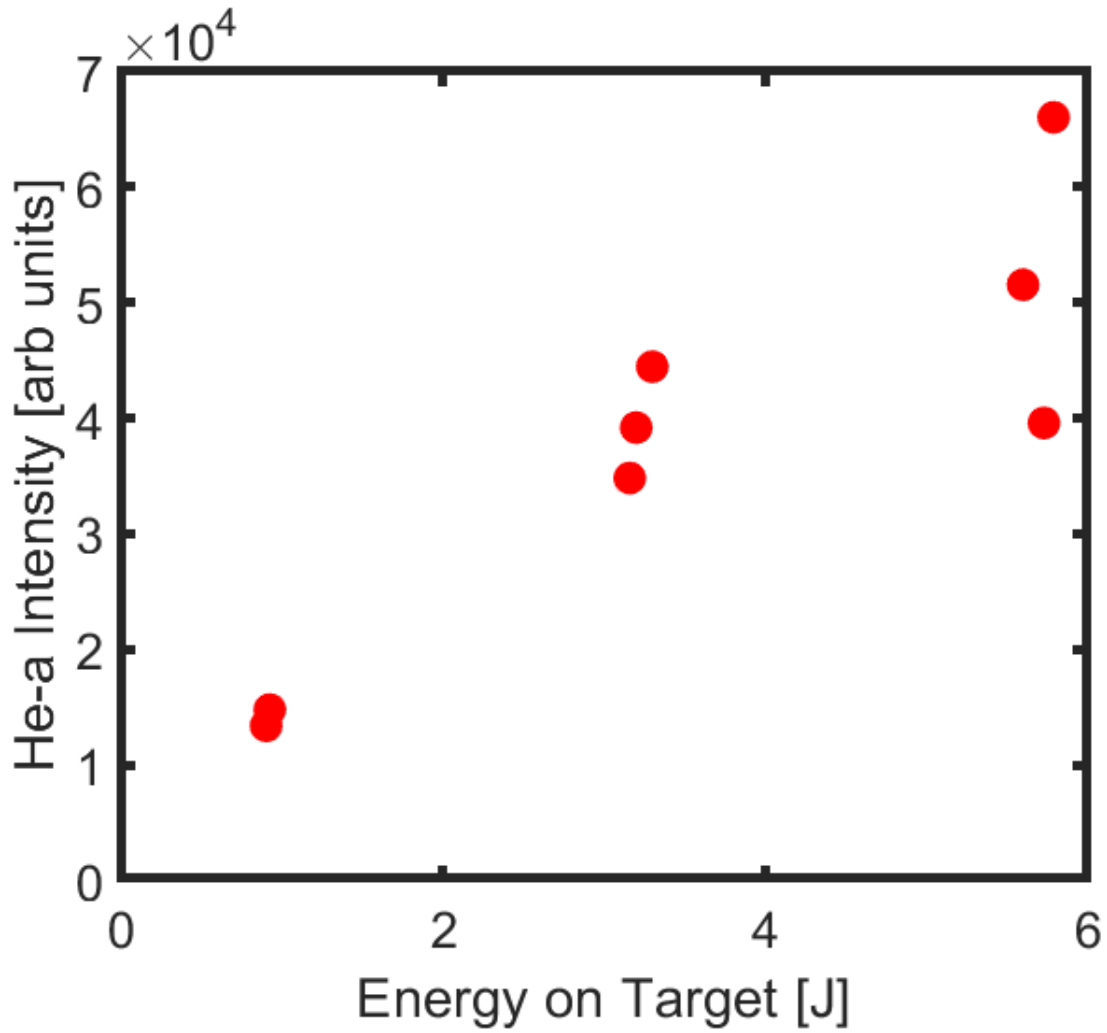


Figure 4.2: Integrated He- α and He/Li line emission from 100nm Ni nanowire arrays versus input energy up to an intensity of $1 \times 10^{21} \text{ Wcm}^{-2}$ showing the linearity of He-like signal.

The He-like and $K\alpha$ emission from the Ni plasma was monitored with a Von Hamos geometry crystal spectrometer. High resolution ($\Delta E/E \approx 1000$), single shot spectra in the 7.2keV-8.4keV photon energy range were recorded with Fujifilm BAS MS film placed in the image plane of a Von Hamos geometry crystal spectrometer using a curved mica crystal ($2d=19.84 \text{ \AA}$) with a radius of curvature of 4 cm in the 3rd diffraction order.

The $h\nu > 1 \text{ keV}$ x-ray emission was simultaneously measured by an array of three filtered Si photodiodes covered with $13 \mu\text{m}$ thick Be filters used to block photons with energies $< 1 \text{ keV}$. Assemblies of 0.5 tesla magnets were placed in front of each of the diodes to ensure that spurious signal from hot electrons do not affect the measurement.

Large surface areas ($>1\text{cm}^2$) nanowires targets were fabricated by electrodepositing nickel into anodic aluminum oxide templates with pore diameters of 100 nm and at two different fractions of solid density, 7% and 24%, which correspond to intrawire separations of 85nm and 230nm respectively. After dissolving the alumina membrane, arrays of free standing parallel nanowires are exposed. All samples were imaged with a scanning electron microscopy prior to the experiment.

4.3 Gap closure time for 100nm diameter Ni nanowire arrays at two densities

The series of spectra in Figure 4.3. shows the variation of the intensity of the resonant He-like and H-like emission for different intrapulse delay for an array with an edge to edge interwire spacing of 85nm, corresponding to an average density of 24% solid density. The individual pulse intensity was $1 \times 10^{21} \text{ Wcm}^{-2}$ and the intrapulse delay was varied in increments of 50fs starting with a delay of 100fs. The two pulse configuration was not operated at a delay of 50fs since this was less than the temporal coherence time of the laser pulses which would have resulted in temporal ringing due to interference between the two pulses of energy. Each spectrum represents an average of 5-7 shots for each time delay.

All the spectra were normalized in intensity to the zero time delay spectrum. The spectra corresponding to 100 fs time delay in Figure 4.3b shows that the He-like emission has decreased slightly

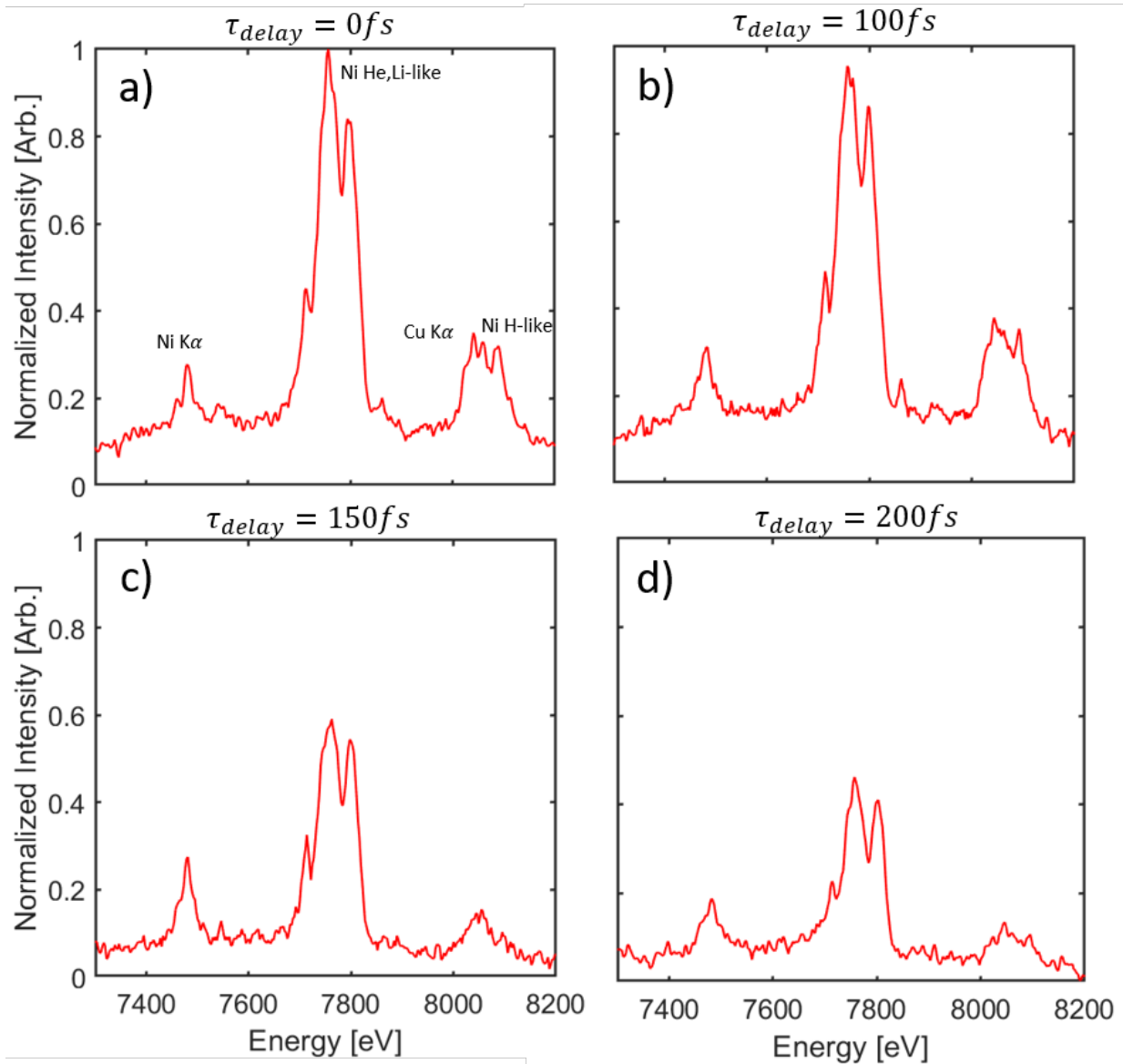


Figure 4.3: Time integrated spectral emission from an array of 100nm diameter Ni nanowires, 24% of solid density corresponding to an interwire spacing of 85nm irradiated at an intensity of $1 \times 10^{21} \text{ Wcm}^{-2}$ corresponding to different intrapulse delays.

respect to the zero delay spectra, but overall the emission is similar including the presence of the H-like Lyman alpha line of Ni which is an indication that at this delay the laser light still couples efficiently into the nanowire array. At a delay of 150fs, however, the He-like line intensity drops to roughly to half of the zero time delay signal, indicating the second pulse is no longer coupling efficiently into the nanowire array and that the gap closure time has been exceeded. The He-like line intensity remains roughly the same as the delay is further increased to 200fs (Figure 4.3d).

Gap closure time measurements were conducted for two irradiation intensities: $5 \times 10^{19} \text{ Wcm}^{-2}$ and a highly relativistic intensity of $1 \times 10^{21} \text{ Wcm}^{-2}$. In each case data was recorded for two arrays of 100nm diameter wires with different edge-to-edge wire separations: 230 nm and 85 nm. Figure 4.4 summarizes the measured integrated emission of the He-like lines versus intra-pulse delay for all four cases. The total He-like emission was calculated by integrating the spectral window from 1.57\AA to 1.60\AA which contains the resonant He- α Ni line as well as the He/Li intercombination lines. In case of the array with 230 nm wire separation irradiated at the lower intensity $5 \times 10^{19} \text{ Wcm}^{-2}$, the gaps remain open for $>200\text{fs}$, as indicated by the fact that at this time the He-like emission remains at $\approx 90\%$ of that at zero delay (Figure 4.4a). In contrast, at the higher irradiation intensity of $1 \times 10^{21} \text{ Wcm}^{-2}$, the He-like intensity at this time has decreased to $\approx 60\%$, an indication of a significantly degraded coupling for the second pulse. The results for the smaller interwire separation, 85 nm, for which the gap is expected to close sooner, show at 100fs the gap is practically close for the lower irradiation intensity (x-ray emission dropped to $\approx 60\%$), while surprisingly it remains practically open ($>90\%$ of the peak He-like emission) for irradiation at highly relativistic intensity (Figure 4.4a).

These conclusions, based on the variation of the line intensity of the He-like Ni lines are corroborated by the simultaneously measured variation of the spectrally integrated x-ray emission at photon energies $> 1 \text{ keV}$, shown in Figure 4.5. Here again at a time delay of 100fs, the gap remains practically open at the highly relativistic intensity, when is already significantly closed for the twenty times lower irradiation intensity. The results suggest that at highly relativistic intensities mechanisms arise that allow for the laser pulse to couple at unexpectedly long times after the

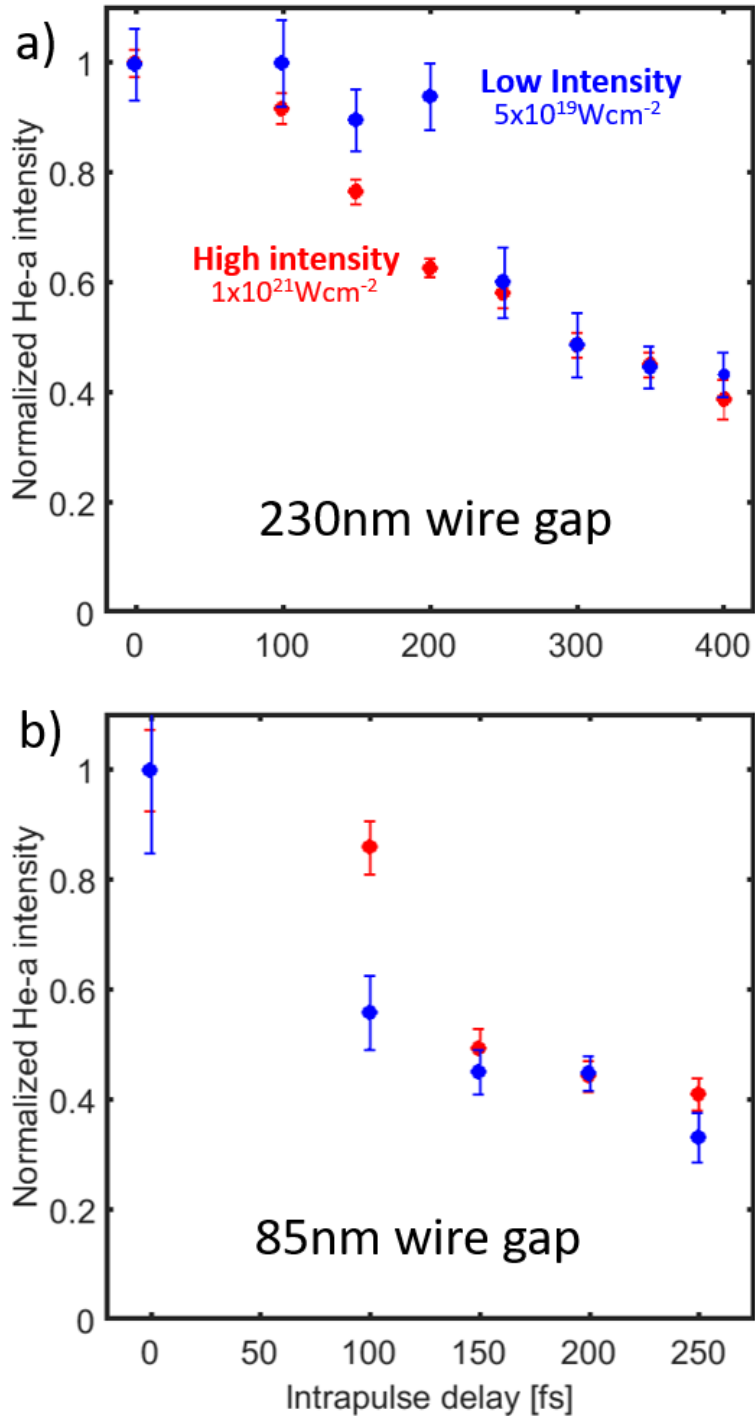


Figure 4.4: Normalized He-like emission integrated in the spectral region between 1.57\AA and 1.6\AA versus intra-pulse delay for wire gaps of 85nm and 230nm is plotted in a,b for two intensities: $1 \times 10^{21} \text{ Wcm}^{-2}$ in red and $5 \times 10^{19} \text{ Wcm}^{-2}$ in blue.

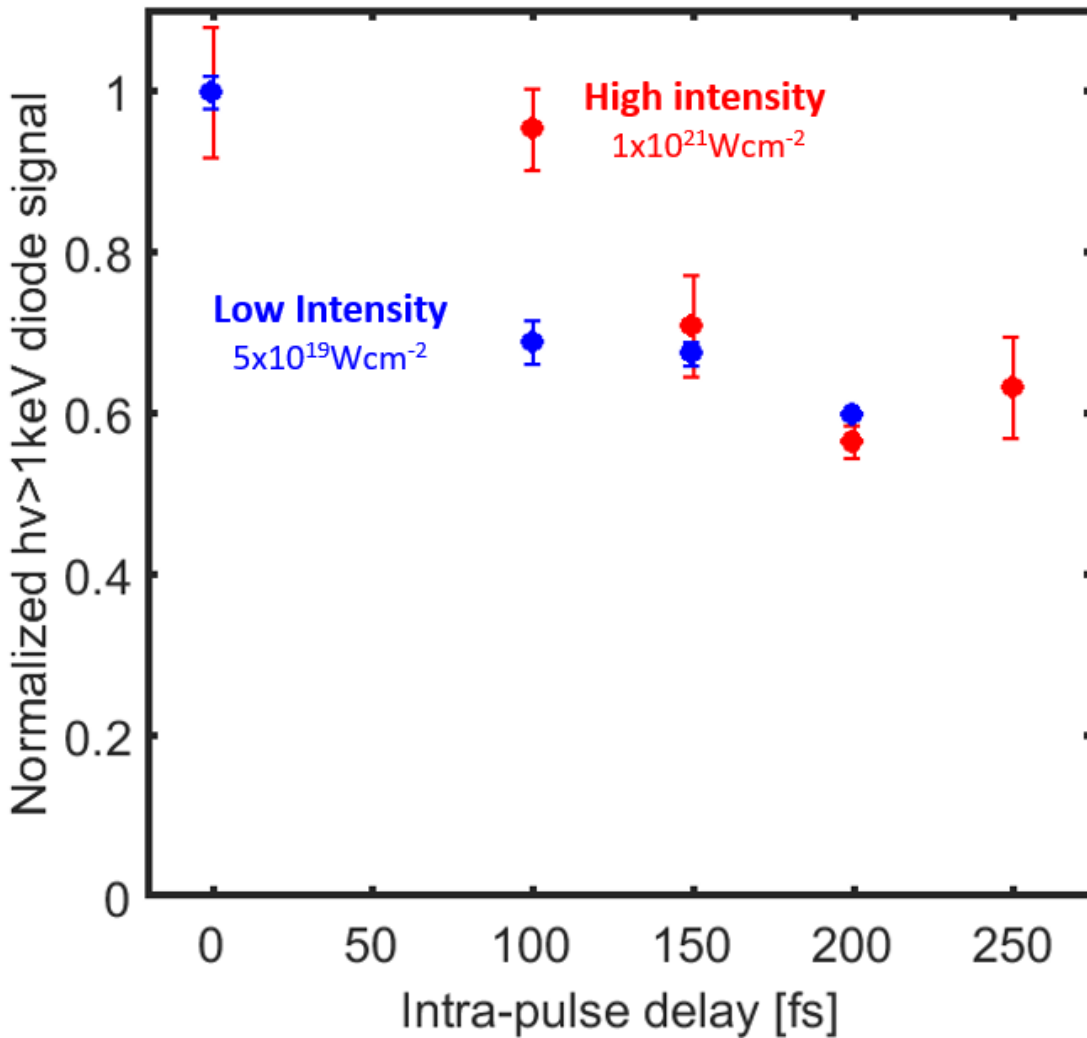


Figure 4.5: Normalized x-ray yield for photon energies $h\nu > 1\text{keV}$ for two different individual pulse intensities, $1 \times 10^{21} \text{ Wcm}^{-2}$ in red and $5 \times 10^{19} \text{ Wcm}^{-2}$ in blue as a function of time delay between the two laser pulses

initial laser pulse. The measurements also provide additional information on the overall conversion efficiency of the optical laser light into > 1 keV x-rays. While the x-ray signals plotted in Figure 4.5 are normalized to the zero time delay signal, the raw data shows that the optical laser to x-ray conversion efficiencies reaches a maximum of 10% in 4π for the 24% solid density nanowire arrays.

4.4 Conclusion

The energy deposition dynamics into nanowire array plasmas was measured for two different intensities, $5 \times 10^{19} \text{ Wcm}^{-2}$ and $1 \times 10^{21} \text{ Wcm}^{-2}$ and for two different 100nm nanowire arrays at two different fractions of solid density, 7% and 24%. At the lower intensities, the coupling time was experimentally determined to be 200fs for an interwire gap distance of 230nm and < 100 fs for an interwire gap distance of 85nm. The dynamics of efficient coupling changes at significantly higher intensities ($a_o \approx 10$) while the time for efficient coupling is shorter (≈ 100 fs) for the 230nm gap size, the 85nm wires exhibit an interesting behavior. The second pulse is still able to couple efficiently and heat the plasma at a 100fs delay after the first pulse. The reason for this is still being investigated using fully relativistic three dimensional particle in cell modeling. Possible explanations include the onset of relativistic transparency [62], the generation of gigagauss azimuthal magnetic fields from strong currents driven in the wires [63] and hot electron generation from the interaction of the second pulse with a thin, surface plasma at the tips of the wires. Further modeling will elucidate these mechanisms and guide our understanding of the interaction of these highly relativistic laser pulses with nanostructured arrays. These results are important for identifying the scaling laws required to use nanostructured targets at high energy picosecond duration laser facilities, such as the ARC facility at LLNL used for radiography of inertially confined fusion plasmas which would benefit from the increased x-ray conversion efficiency exhibited by nanowire arrays.

Chapter 5

Extreme degree of ionization in near solid density plasmas volumetrically heated by highly relativistic laser pulses

Overview: Stripping heavy elements such as gold of most electrons in near solid density environments is challenging and requires heating significant plasma volumes to extreme temperatures, achieved in the core of spherical compression experiments driven by the world's largest lasers. This chapter reports using highly relativistic femtosecond laser pulses of less than 10 joules of laser energy focused to intensities of $4 \times 10^{21} \text{ Wcm}^{-2}$ to volumetrically heat near solid and solid density plasmas to temperatures $>5 \text{ keV}$. Nanowire arrays and solid foils of gold and nickel were observed to reach the Ne-like Au (Au^{69+}) and H-like (Ni^{27+}) states. While the solid density targets exhibit a higher average charge state, the nanowire plasma are experimentally determined to have an order of magnitude larger volume. This results in up to 10 times enhancement in X-ray emission due to decreased hydrodynamic cooling.

5.1 Introduction

High nuclear charge (Z) elements with an extreme degree of ionization are difficult to achieve in near solid density plasmas. Gold atoms ionized by electron impact excitation with an electron beam while trapped in a potential well have been ionized up to Ne-like stage, producing very high quality L-shell spectra from the 3d-2p transition over a broad range of high ion charges [64, 65]. However, these plasmas are characterized by very low plasma densities, over 10 orders of magnitude below solid density. Achieving similar degrees of ionization in solid density plasmas require the deposition of extreme energy densities to achieve the required high temperatures and

high collisional ionization rates. This is achieved in the core of spherical compressions driven by lasers using kilojoules to megajoules of laser energy.

For example, experiments conducted at the OMEGA laser using 9kJ pulses on a reduced scale 'hot' hohlraum revealed strong emission from the L shell transitions of gold [66]. The resolution of the spectrometer used was not sufficiently high to resolve contributions from individual charge states, rather the position of the central peak of the 3d-2p structure centered on the Ti-like Au (Au^{57+}) ion which resulted in an inferred temperature of 6.5 keV at an electron density of 10^{21} cm^{-3} .

In another experiment performed at the Vulcan laser system at Rutherford Appleton Laboratory, mid-Z elements such as Ni were irradiated with intensities up to $5 \times 10^{20} \text{ Wcm}^{-2}$, with 400 J pulses of 0.8ps duration. X-ray spectroscopy of the Ni K shell revealed emission from the Ly- α transitions, at roughly a sixth of the intensity of the He-like 1s2p-1s² transitions suggesting a surface temperature of 5 keV decreasing to 600 eV at a $1.3 \mu\text{m}$ depth using 400J of laser energy [32].

Recent experiments conducted at the J-KAREN-P laser facility at the Kansai Photon Science Institute also investigated the irradiation of mid Z elements— stainless steel foils containing mostly Fe with some Cr and Ni. At an intensity of $3 \times 10^{21} \text{ Wcm}^{-2}$ emission from He-like Fe was observed similar in intensity to the neutral K- α as well as a small amount of H-like Fe signal, comparable to the continuum [28]. With this, the modeling (Spectroscopic Collisional-Radiative Atomic Model SCRAM [29]) suggested an electron temperature of 2.1 keV at an electron density of $5 \times 10^{22} \text{ cm}^{-3}$.

Here we report for the first time a sufficiently resolved Au L shell transition array with emission up to the Ne-like state Au^{69+} as well as the observation of hydrogen-like emission from Ni plasmas exceeding half the intensity of the He-like transitions using a less than 10J of energy from a compact laser focused to an intensity of $4 \times 10^{21} \text{ Wcm}^{-2}$. We compare results obtained by irradiating aligned nanowire arrays with those obtained by irradiating solid targets of the same materials. We show that at these intensities ($a_o > 20$), it is possible to volumetrically heat solid density plasmas from foils to depths of $>1 \mu\text{m}$ and plasmas from aligned nanowire plasmas at 15 % of solid density to $>6 \mu\text{m}$ in depth. The results demonstrate that highly relativistic, high contrast, femtosecond laser

pulses with less than 10J of energy, can volumetrically heat solid density and near solid density plasmas to extreme states of ionization. Moreover, the study shows that at these highly relativistic irradiation intensities solid foil targets reach higher degree of ionization due to an increased collisional excitation rate, the larger plasma volume from irradiating arrays of nanowires results in one order of magnitude higher conversion efficiency into $h\nu > 1$ keV x-rays.

5.2 Gold L shell emission at highly relativistic intensities

The experiments were conducted at the newly commissioned high repetition rate petawatt class Ti:Sapphire laser at Colorado State University [42] described in Chapter 2, delivering up to 10J of high contrast ($>10^{12}$), $\lambda=400$ nm light with a pulse duration of 45fs. The beam is focused with an $f/2$ off axis parabola to a near diffraction limited spot size of $1.6\mu\text{m}$ FWHM generating a focal intensity of $4 \times 10^{21} \text{ Wcm}^{-2}$. At this intensity, the ultrahigh contrast is necessary to prevent the creation of a preplasma prior to the arrival of the main pulse. Gold nanowire arrays and solid density targets were irradiated while monitoring emission from the L shell region (9.5-11keV). These lines originate from the Ni-like (Au^{51+}) to Ne-like (Au^{69+}) ions. X-ray spectroscopy was performed using a mica crystal ($2d = 19.84\text{\AA}$) with a radius of curvature of 40mm in a Von Hamos configuration in the 3rd order [45]. The spectrographs were recorded on Fujifilm BAS MS image plate. The spectrometer had moderate resolution ($\Delta E/E \approx 1000$) and was able to distinguish the contributions from individual L shell ion originating from the near solid density plasma.

The complex L shell spectra was carefully calibrated using the well resolved He-like and H-like transitions from the K shell of germanium at 10274eV and 10569eV, respectively shown in Figure 5.1. The Au L shell spectra in Figure 5.3 were taken by exposing image plate for 3 shots in quick succession to avoid fading. The blue curve corresponds to a solid density Au target whereas the red curve is for a 80nm diameter Au nanowire array at 12% of solid density. At an intensity of $4 \times 10^{21} \text{ Wcm}^{-2}$, both targets display emission from the Ne-like Au transition at 10527eV. The average charge state for the nanowire array is centered around P-like Au, whereas the solid density targets are centered around the Mg-like Au state, which has a charge of 4 higher, both significantly

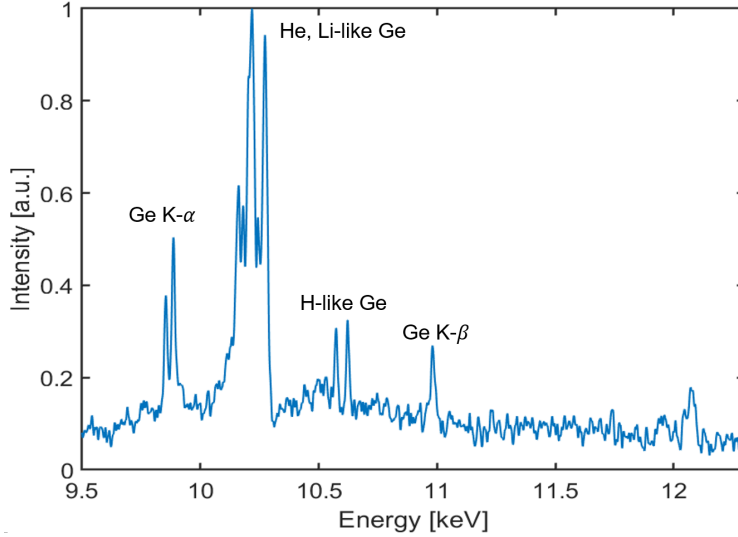


Figure 5.1: Ionized K shell spectrum from solid Ge irradiated at $4 \times 10^{21} \text{ Wcm}^{-2}$.

higher in ionization than the reduced scale hot hohlraums irradiated at OMEGA that achieved an average charge state of Ti-like Au^{57+} [66] using 9kJ, 1ns laser pulses.

Steady state modeling using FLYCHK [67] suggested that Ne-like Au appears at a temperature of $\approx 7\text{keV}$ for $n_e = 3 \times 10^{23} \text{ cm}^{-3}$ (nanowires) and $n_e = 3 \times 10^{24} \text{ cm}^{-3}$ (solid densities) shown in Figure 5.2. This temperature was chosen since it shows the creation of Ne-like Au for both densities. It represents a lower bound of the actual temperature since the plasma is transient and there is a finite amount of time to achieve the ionization state through sequential step ionization processes. The average charge state of the two plasmas is also nearly matched at Au^{65+} and Au^{68+} for nanowires and foils, respectively. This suggests that the difference in ionization state is strictly due to the change in plasma density, which increases the collisional ionization rate of the plasma.

5.3 Strong Lyman- α emission from Ni nanowires and solid density targets

Single shot, time integrated K shell x-ray spectra from both nickel nanowires and nickel solid density targets irradiated at 4 different intensities are shown in Figure 5.4. At an intensity of $4 \times 10^{20} \text{ Wcm}^{-2}$, the 55nm nanowires at 12% solid density in 1a display a significant amount of He-like

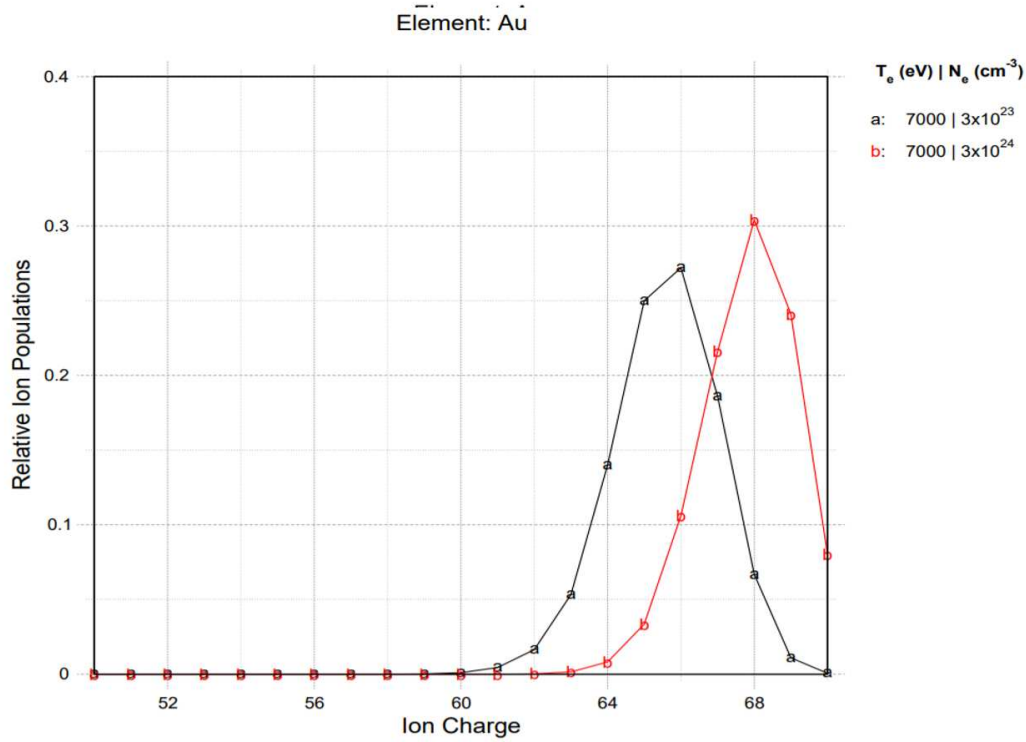


Figure 5.2: Charge state distribution for two different Au plasmas with $T_e=7\text{keV}$ at for two different densities: a nanowire plasma ($n_e=3 \times 10^{23} \text{ cm}^{-3}$) and a solid density plasma ($n_e=3 \times 10^{24} \text{ cm}^{-3}$).

emission, exceeding that of the neutral K- α by over an order of magnitude. As the intensity is increased to $1 \times 10^{21} \text{ Wcm}^{-2}$, emission from the Ly- α_2 8073eV and Ly- α_1 at 8096eV from the Ni⁺²⁷ ions begin to appear. The spectra also contain lines from neutral Cu K- α that result from the 75 μm copper backing that supports the 100nm Au film on which the nanowire arrays are grown. The Cu K- α slightly overlaps with the Ni Ly- α_1 , but the Ni Ly- α_2 is unaffected. The intensity scan of the solid density pure Ni target (Figure 5.4b) also shows the onset of the Ly- α lines at an intensity of $4 \times 10^{20} \text{ Wcm}^{-2}$, which do not contain any copper. The ratio of the Ly- α_1 to the He- α emission is plotted in Figure 5.4c for 24 single shots versus laser energy deposited on target. For the solid density target, the intensity of the Ly- α_1 exceeds half of the He-like emission while the nanowire target at 12% solid density only reaches a ratio of 15%. To our knowledge, this Ly to He ratio of 0.5 for solid density Ni is the highest reported in the literature for a mid-Z plasma. The intensity ratio corresponding to the solid density target is significantly higher than that of the nanowire array. This is due to the higher collisional ionization rate since the solid density target's

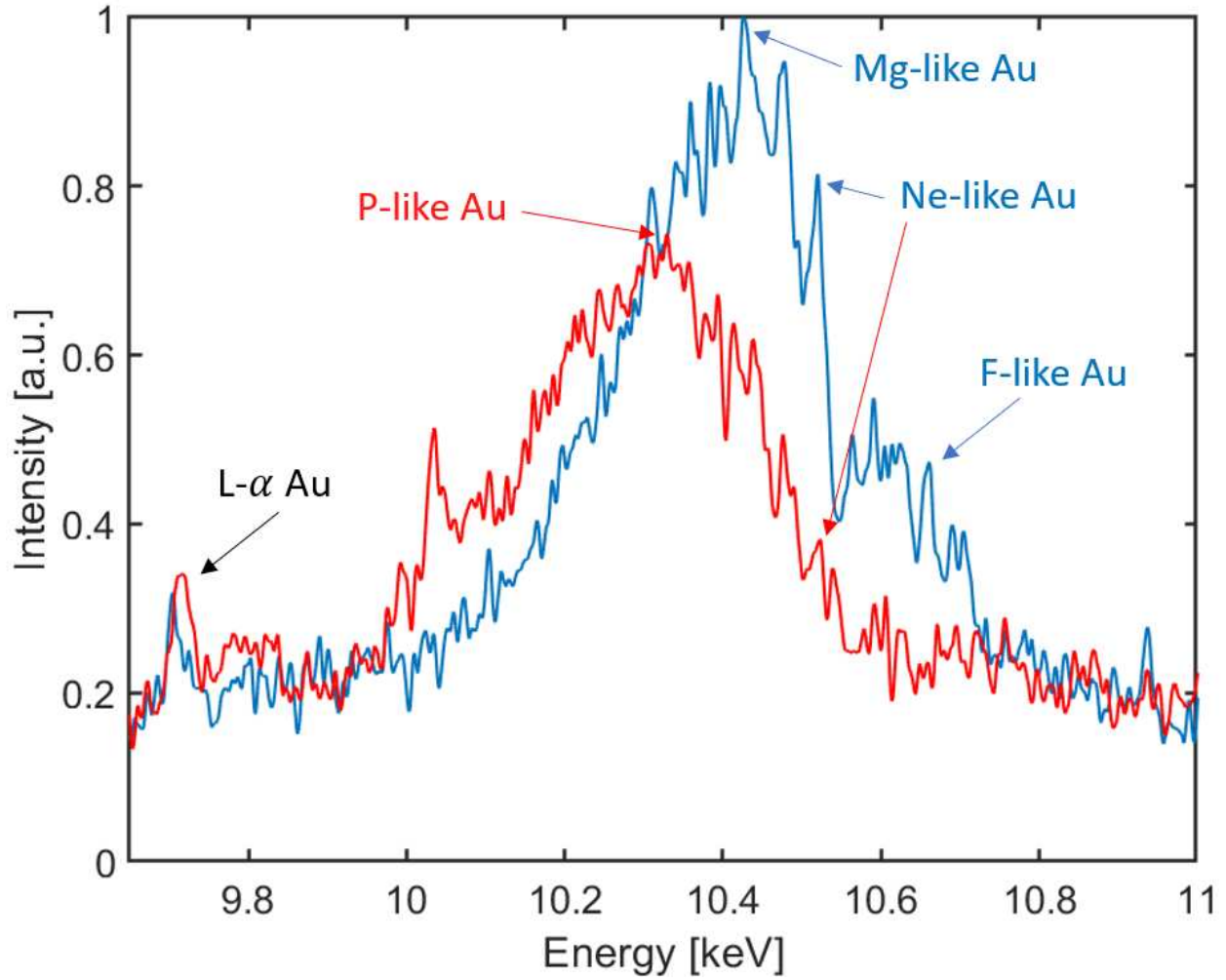


Figure 5.3: L shell emission from 12% solid density, 55nm diameter Au nanowire array irradiated at 4×10^{21} Wcm^{-2} (red curve) and solid density Au targets (blue curve). The charge state reaches up to Ne-like Au for both targets, however the average charge state distribution is centered around P-like Au for the nanowire plasma and Mg-like Au for the solid density plasma.

electron density is several times higher than the nanowire array during the emission time. However, the nanowire plasma emits $>3.5\times$ more photons from the He-like region of the spectrum (1.58Å to 1.62Å) than the flat target.

5.4 Measurement of heat penetration into solid density Ni using buried Co tracers

The heat penetration depth in Ni foil was studied by monitoring the ionized K shell emission of a Co buried tracer underneath a variable amount of Ni. In this measurement, a dual composition target consisting of a varying amount of Ni on top of a Co tracer was irradiated on the Ni side. The Ly- α and He- α spectral emission from the Co tracer was monitored while varying the thickness of the nickel layer. These materials were chosen since they differ in nuclear charge by one, thus they can be simultaneously recorded on the spectrometer. The lines originating from the buried Co tracer are optically thin in the Ni plasma above it. A single shot x-ray spectrum of a target consisting of 0.25 μm of Ni on top of several micron of Co is shown in Figure 5.5a. The spectrum shows clearly resolved He-like Co and Ni and H-like Ni lines, while the H-like emission from Co is slightly overlapped with the neutral Ni K- α line, similar to the case of neutral Cu K shell overlapping with H-like Ni. As the thickness of the Ni layer increases, the intensity of He-like Co continues to decrease with respect to the He-like and H-like Ni lines. When the Co layer is underneath 1 μm of Ni, the Co He-like lines are still visible indicating a penetration depth of slightly greater than 1 μm in solid density Ni as seen in Figure 5.5c. The He-like Co lines merge with the continuum at a depth of 2.5 μm of Ni in Figure 5.5d. A summary of the He-like Co emission as a function of depth under the Ni foil is plotted in Figure 5.5e. A depiction of the target setup can be found in the inset of Figure 5.5e.

This increase in penetration depth is in part due to the modification of the critical electron density from relativistic transparency. The critical electron density for $\lambda=400\text{nm}$ is $6.87\times 10^{21}\text{ cm}^{-3}$. However, for a laser strength parameter of $a_0 \approx 20$, the relativistically corrected electron density is nearly 10^{23} cm^{-3} allowing for significantly higher penetration of the laser energy into

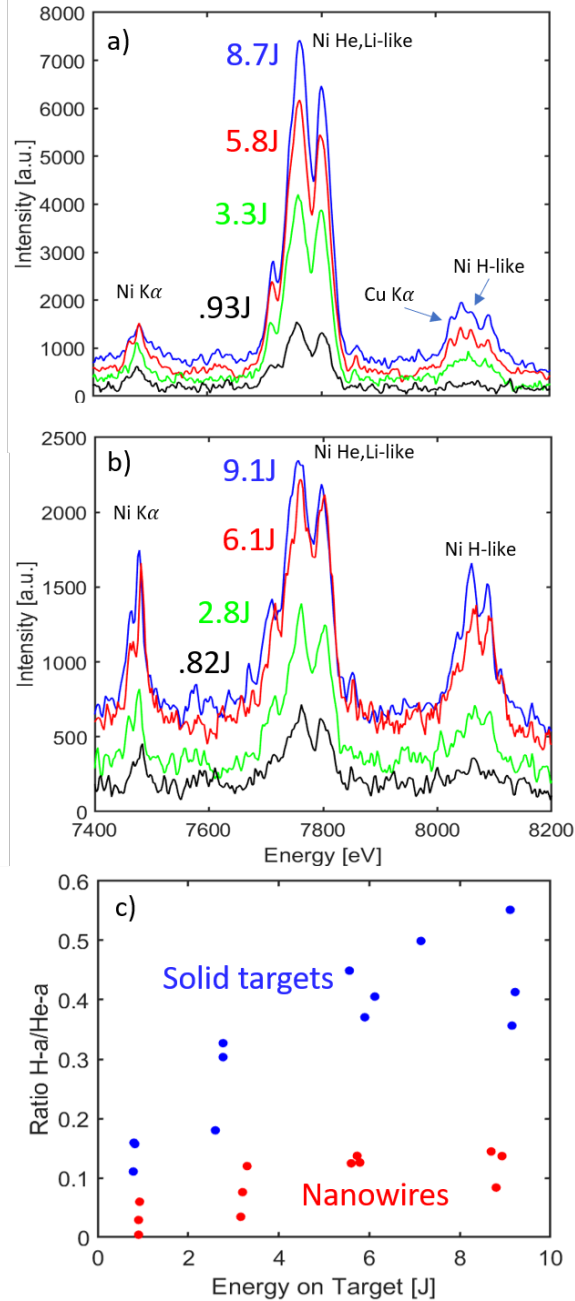


Figure 5.4: (a,b) Single shot x-ray spectra of ionized K shell emission of Ni with significant radiation from Lyman- α and He-like lines for a) 55nm nanowire array at 12% of solid density and b) solid density Ni target irradiated at four different intensities. Laser energy on target is displayed for each shot. Blue curves correspond to an intensity of $\approx 4 \times 10^{21} \text{ Wcm}^{-2}$ while black curves correspond to an intensity of $\approx 4 \times 10^{20} \text{ Wcm}^{-2}$. The ratio of the Lyman- α and He-like lines are shown in c) for solid flat targets in blue and nanowires in red for 24 individual laser shots.

the targets. [62,68]. A corresponding heat penetration experiment was also conducted for nanowire arrays using 55nm diameter dual composition wires at 12% of solid density with 6 μm of Ni on top of 3 μm of Co for comparison. The He-like Co lines are still visible under the Ni at an intensity of $4 \times 10^{21} \text{ Wcm}^{-2}$. This result shows that the nanowire plasmas are roughly six times larger in depth than the solid density target plasmas allowing us to conclude that the heat penetration at these highly relativistic irradiation conditions is several times larger in the nanowire array than the solid density target.

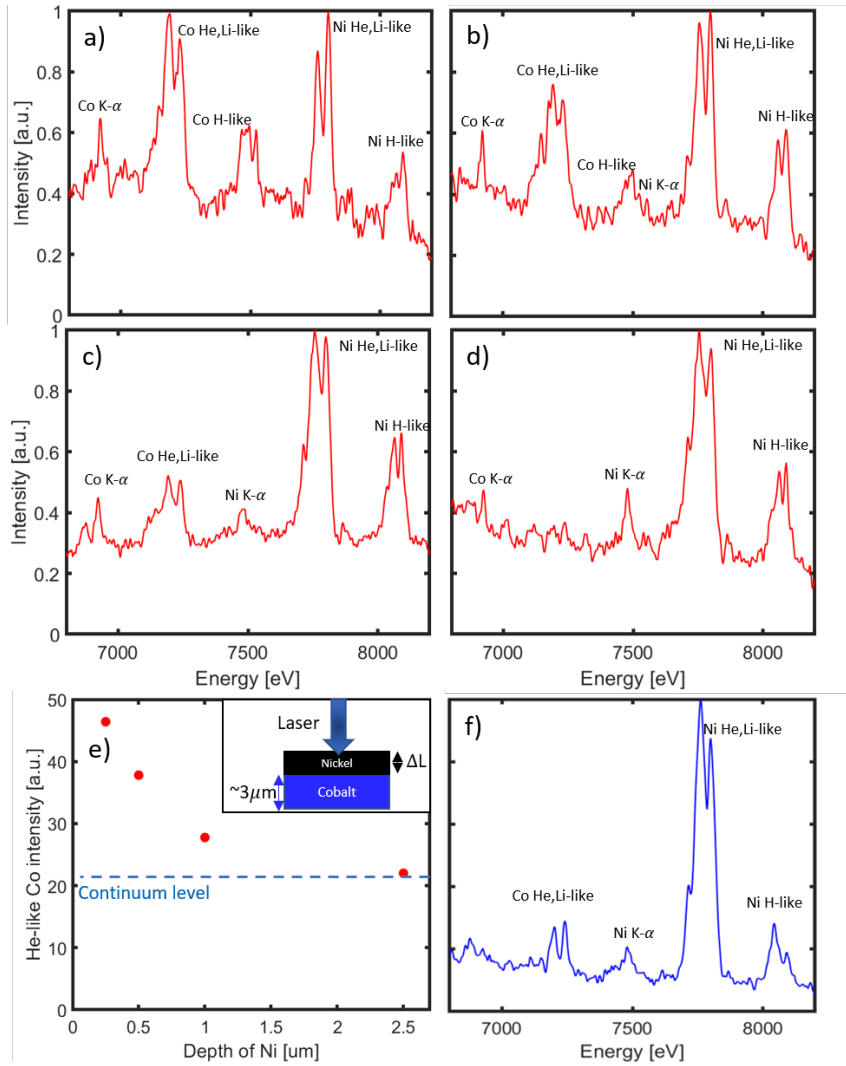


Figure 5.5: Heat penetration into solid density material by monitoring highly ionized Co tracer underneath varying amount of Ni. (a)-(d) are single shot spectra monitoring the ionized K shell emission of a Co tracer under a layer of $0.25\mu\text{m}$ of Ni in (a) to $2.5\mu\text{m}$ of Ni in (d). The integrated He-like Co intensity is versus the Ni thickness is plotted in (e) with an inset showing the setup of the tracer experiment. The foil result is compared to a 55nm nanowire array consisting of $6\mu\text{m}$ of Ni wires on top of $3\mu\text{m}$ of Co wires at 12% solid density showing a signal similar to that of the $1\mu\text{m}$ solid target in (f).

5.5 Lateral source size of nanowire and solid density targets

The lateral extent of these multi-keV temperature plasmas were determined by measuring the x-ray source size with point projection radiography of a tungsten carbide (WC) sphere [69]. The sphere suffers no parallax and is of sufficiently high Z to block x-rays from propagating through it. From the width of the geometrical penumbra, it is possible to calculate the x-ray source size. Figure 5.6 shows radiographs of a $500\mu\text{m}$ WC sphere placed at approximately 6cm from the plasma. An e2v 4240 silicon charge coupled device (CCD) camera with $13.5\mu\text{m}$ pixels recorded the radiographs at a distance of 2.5m from the source, resulting in a magnification of 43.5x. At this magnification, the effective pixel size was 300nm, sufficient to measure the penumbra of the WC sphere when irradiating a solid density target (Figure 5.6a) or a nanowire target (Figure 5.6b). A filter consisting of $13\mu\text{m}$ of Be and $50\mu\text{m}$ of Al was placed in front of the CCD to filter out photons $h\nu < 6\text{keV}$. A high end spectral cut off is provided by the absorption of the Si in the CCD, which rapidly decays for $h\nu > 20\text{keV}$. The lineout of the edge of the sphere is plotted for both targets in Figure 5.6c. The source size is related to the size of the penumbra divided by the magnification of the imaging system. The geometry of this analysis is shown in Figure 5.6d. The source size is found to be $6\mu\text{m}$ for the solid density target and $10\mu\text{m}$ for the nanowire array target, a ratio of 2.7 in surface area. The larger size of the nanowire source is likely the result of a larger velocity of the diffusive heatwave that propagates laterally with a velocity proportional to $1/\sqrt{n_e}$. For the nanowire plasma with 15% of solid density, the heat wave should propagate at a velocity 2.5 faster than a solid density plasma at the same temperature.

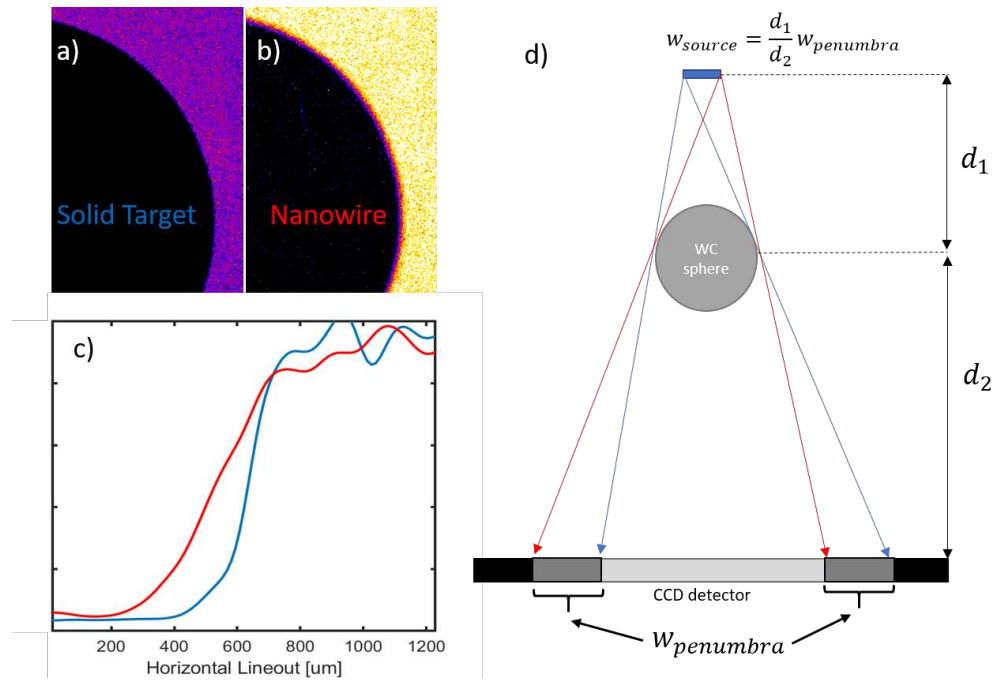


Figure 5.6: Measurement of the x-ray source size from analysis of the penumbra of a point projection radiograph of a $500\mu\text{m}$ tungsten carbide sphere with a magnification of $43.5\times$ for $h\nu > 6\text{keV}$. The radiograph from irradiating a solid flat target at $4 \times 10^{21} \text{ Wcm}^{-2}$ is shown in (a) and for a 15% 100nm Ni nanowire in (b) which is $\approx 3\times$ brighter. The source size is computed to be $6\mu\text{m}$ for the solid and $10\mu\text{m}$ for the nanowire array from the normalized lineouts of the radiographs in (c) using the geometrical analysis in (d).

The nanowire target plasma volume is therefore found experimentally to be over an order of magnitude greater than the solid density target. This increase in plasma volume increases the hydrodynamic expansion time allowing plasma radiation to be an increased energy loss mechanism. This results a more efficient conversion of the optical laser light into x-rays [12]. The x-ray conversion efficiency for Ni nanowire arrays and solid density targets measured using an array of filtered Si photodiodes (AXUV100-G from International Radiation Detectors) is plotted in Figure 5.7 for photon energies $h\nu > 1\text{keV}$ (a) and $>6\text{keV}$ (b) versus laser energy deposited on target. An array of 3 diodes for each spectral window (13 μm Be used for $h\nu > 1\text{keV}$ and 50 μm Al used for $h\nu > 6\text{keV}$) were placed at 2.5m from the plasma at 22.5, 45 and 67.5 degrees to measure the angular emission. The x-ray conversion efficiency for solid targets is found to increase by nearly a factor of 2 from 0.8% at $4 \times 10^{20}\text{ Wcm}^{-2}$ to nearly 1.5% at $2.6 \times 10^{21}\text{ Wcm}^{-2}$. The x-ray conversion efficiency from 100nm, 15% solid density nanowire targets stays relatively unchanged in this intensity range, with high shots exceeding 10%. For $h\nu > 6\text{keV}$ photons, the x-ray conversion efficiency for both nanowire arrays and solid density targets increase as a function of intensity, with nanowires reaching nearly 0.7% and solid targets reaching 0.25% conversion efficiency.

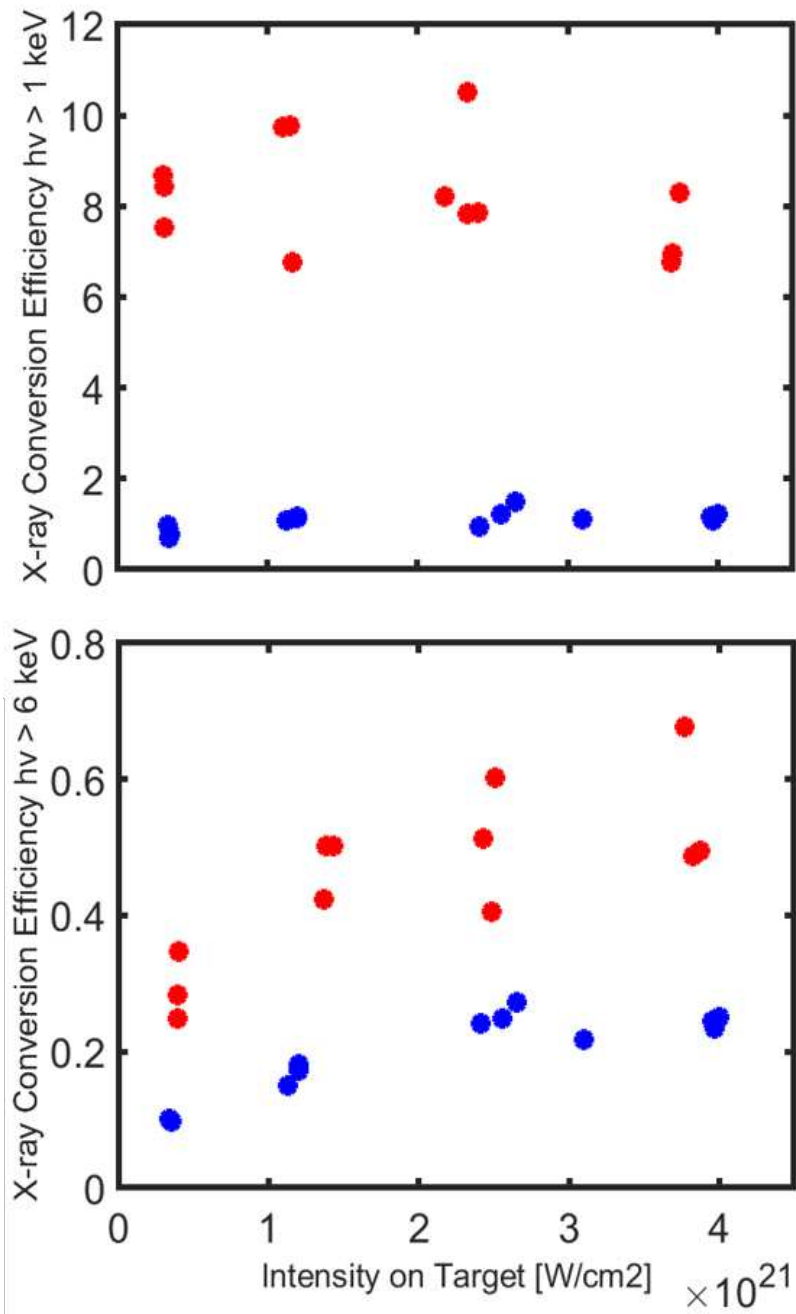


Figure 5.7: (a) X-ray conversion efficiency for photons $h\nu > 1\text{keV}$ for 100nm diameter Ni nanowire arrays at 15% of solid density (red) and solid density targets (blue) at intensities of 4×10^{21} to $4 \times 10^{21} \text{ Wcm}^{-2}$. (b) CE into $h\nu > 6\text{keV}$ x-rays.

5.6 Conclusion

It was demonstrated that both solid density and near solid density Au and Ni targets irradiated at intensities $>10^{21} \text{ Wcm}^{-2}$ with pulses of $<10\text{J}$ of laser energy can reach ionization states of Ne-like and H-like. While the ionization state of the solid density targets exceeds that of the nanowire targets, the optical to x-ray conversion efficiency is measured to be greater for the nanowire targets by a factor of $\approx 10\text{x}$ and $\approx 3\text{x}$ for $>1\text{keV}$ and $>6\text{keV}$ x-rays, respectively. The volume of the nanowire and solid target plasmas were measured by using buried tracers to estimate the depth of the plasma combined with observing the change in the penumbra of the x-ray source sizes to estimate the lateral source size. The order of magnitude increase in the volume of the nanowire plasmas compared to the solid target plasmas increases the hydrodynamic lifetime of the plasma, allowing more time for the collisions to convert kinetic energy in the plasma to x-ray radiation. These highly relativistic laser nanostructure interactions constitute the first measurements of plasmas from ordered nanowire targets at these laser intensities.

Chapter 6

Conclusions

The interaction of high contrast, relativistic laser pulses with vertically aligned, ordered nanostructures has been demonstrated to volumetrically heat plasmas to multi-keV temperatures at near solid densities. Achieving volumetric heating in turn results in an increase of the hydrodynamic cooling time while the high density results in a high collisional rate and a decreased radiative cooling time. The plasma is then able to convert much of its' energy into x-rays before cooling through hydrodynamic expansion leading to a very efficient conversion of visible laser light to x-rays. The work reported in this dissertation has shown that using this approach can yield a 20% conversion efficiency into $h\nu > 1\text{keV}$ x-rays when irradiating 12% solid density arrays of 80nm diameter Au nanowires at an intensity of $4 \times 10^{19} \text{ Wcm}^{-2}$, a record for picosecond duration x-ray sources. These x-ray sources were also measured to be several micron in size which make them attractive for ultrafast point projection radiography.

In order to conduct experiments at highly relativistic intensities, a second harmonic beamline was constructed capable of delivering up to 10 joules of high contrast ($>10^{12}$), 45fs duration pulses at $\lambda = 400\text{nm}$. Using a $f/2$ off axis parabola focused to a near diffraction limit, it was possible to achieve intensities $>10^{21} \text{ Wcm}^{-2}$.

Efficient energy coupling of the laser pulse into the nanowire array requires the laser pulse to be shorter than the time it takes for the wires to explode and fill the interwire gap with a supercritical density plasma. Experiments were conducted to measure this time limit for efficient coupling of the laser into the nanowire array. The measurements were performed by creating two identical laser pulses delayed in time and monitoring the x-ray emission of the plasma including spectrally resolved He-like line emission. The experiment concluded that the amount of time for efficiently coupling laser energy into a 100nm Ni nanowire arrays is on the order of less than 200fs for low density arrays. It was found arrays at a higher fraction of solid density, 24%, exhibit an interesting behavior. While at low intensities the efficient coupling time was found to be $<100\text{fs}$, it increases

for highly relativistic intensities. Despite the increase in intensity, the second pulse is still able to efficiently couple into the array at a delay of 100fs suggesting the onset of physical mechanism which allows the laser pulse to still couple its' energy at times greater than the dissociation time of the nanowire array. The investigation of this mechanism is still ongoing using fully relativistic three dimensional particle in cell simulations. Ultimately, a better understanding of the time limit for efficient coupling into the nanowire arrays will guide experiments at larger, high energy laser facilities characterized by longer laser pulses.

Finally, detailed measurements of the ionization state of solid flat targets and near solid density Au and Ni nanowire targets were conducted for intensities $>10^{21} \text{ Wcm}^{-2}$. It was found that Ne-like Au and H-like Ni could be achieved using $<10\text{J}$ of laser energy. The nanowire array targets achieved higher x-ray conversion efficiency despite solid density targets achieving a slightly higher ionization state. This is attributed to the larger volume of the nanowire plasmas, which were measured to be an order of magnitude larger for the nanowire array, similar to the ratio of the x-ray conversion efficiency for $h\nu > 1\text{keV}$ for both targets.

This work contributes to the study of the interaction of ordered nanostructures with relativistic laser pulses which is a relatively nascent field. Significant future work must still be conducted. For example, all of the experiments presented in this dissertation are time integrated– temporally resolved experiments using x-ray streak cameras will help to further understand plasma dynamics by observing the changes in x-ray emission in time. As more powerful, higher contrast laser systems come online in the next decade, new opportunities to further extend this field of research will arise. These include the possibility of optically pumped synchrotron emission from ordered nanowire arrays resulting in an increase of x-ray source brightness [70, 71], the production of gigagauss magnetic fields produced by large return currents through the nanowires [63] and the generation of extreme pressures [10]. These and other phenomena should be an area of exploration for this class of interactions over the next several years.

Bibliography

- [1] O. A. Hurricane, D. A. Callahan, D. T. Casey, P. M. Celliers, C. Cerjan, E. L. Dewald, T. R. Dittrich, T. Döppner, D. E. Hinkel, L. F. Hopkins, J. L. Kline, S. Le Pape, T. Ma, A. G. Macphee, J. L. Milovich, A. Pak, H. S. Park, P. K. Patel, B. A. Remington, J. D. Salmonson, P. T. Springer, and R. Tommasini, “Fuel gain exceeding unity in an inertially confined fusion implosion,” *Nature*, vol. 506, no. 7488, pp. 343–347, 2014.
- [2] S. H. Glenzer, B. J. MacGowan, P. Michel, N. B. Meezan, L. J. Suter, S. N. Dixit, J. L. Kline, G. A. Kyrala, D. K. Bradley, D. A. Callahan, E. L. Dewald, L. Divol, E. Dzenitis, M. J. Edwards, A. V. Hamza, C. A. Haynam, D. E. Hinkel, D. H. Kalantar, J. D. Kilkenny, O. L. Landen, J. D. Lindl, S. LePape, J. D. Moody, A. Nikroo, T. Parham, M. B. Schneider, R. P. J. Town, P. Wegner, K. Widmann, P. Whitman, B. K. F. Young, B. Van Wonterghem, L. J. Atherton, and E. I. Moses, “Symmetric Inertial Confinement Fusion Implosions at Ultra-High Laser Energies,” *Science*, vol. 327, pp. 1228 LP – 1231, mar 2010.
- [3] S. Fujioka, H. Takabe, N. Yamamoto, D. Salzmann, F. Wang, H. Nishimura, Y. Li, Q. Dong, S. Wang, Y. Zhang, Y. J. Rhee, Y. W. Lee, J. M. Han, M. Tanabe, T. Fujiwara, Y. Nakabayashi, G. Zhao, J. Zhang, and K. Mima, “X-ray astronomy in the laboratory with a miniature compact object produced by laser-driven implosion,” *Nature Physics*, vol. 5, no. 11, pp. 821–825, 2009.
- [4] H. F. Robey, P. A. Amendt, J. L. Milovich, H. S. Park, A. V. Hamza, and M. J. Bono, “Hohlraum-driven mid-Z (SiO₂) double-shell implosions on the omega laser facility and their scaling to NIF,” *Physical Review Letters*, vol. 103, no. 14, pp. 1–4, 2009.
- [5] S. Le Pape, L. F. Berzak Hopkins, L. Divol, A. Pak, E. L. Dewald, S. Bhandarkar, L. R. Benedetti, T. Bunn, J. Biener, J. Crippen, D. Casey, D. Edgell, D. N. Fittinghoff, M. Gatu-Johnson, C. Goyon, S. Haan, R. Hatarik, M. Havre, D. D. Ho, N. Izumi, J. Jaquez, S. F. Khan, G. A. Kyrala, T. Ma, A. J. Mackinnon, A. G. Macphee, B. J. Macgowan, N. B. Meezan,

- J. Milovich, M. Millot, P. Michel, S. R. Nagel, A. Nikroo, P. Patel, J. Ralph, J. S. Ross, N. G. Rice, D. Strozzi, M. Stadermann, P. Volegov, C. Yeamans, C. Weber, C. Wild, D. Callahan, and O. A. Hurricane, "Fusion Energy Output Greater than the Kinetic Energy of an Imploding Shell at the National Ignition Facility," *Physical Review Letters*, vol. 120, no. 24, p. 245003, 2018.
- [6] H. S. Park, O. A. Hurricane, D. A. Callahan, D. T. Casey, E. L. Dewald, T. R. Dittrich, T. Döppner, D. E. Hinkel, L. F. Berzak Hopkins, S. Le Pape, T. Ma, P. K. Patel, B. A. Remington, H. F. Robey, J. D. Salmonson, and J. L. Kline, "High-adiabat high-foot inertial confinement fusion implosion experiments on the national ignition facility," *Physical Review Letters*, vol. 112, no. 5, pp. 1–5, 2014.
- [7] T. Maiman, "Stimulated Optical Radiation in Ruby," *Nature*, vol. 187, no. 4736, pp. 493–494, 1960.
- [8] H. Kiriyama, A. S. Pirozhkov, M. Nishiuchi, Y. Fukuda, K. Ogura, A. Sagisaka, Y. Miyasaka, M. Mori, H. Sakaki, N. P. Dover, K. K. Kondo, J. K. Koga, T. Z. Esirkepov, M. Kando, and K. K. Kondo, "High-contrast high-intensity repetitive petawatt laser," *Opt. Lett.*, vol. 43, pp. 2595–2598, jun 2018.
- [9] A. J. Kemp and L. Divol, "What is the surface temperature of a solid irradiated by a Petawatt laser?," *Physics of Plasmas*, vol. 23, no. 9, 2016.
- [10] C. Bargsten, R. Hollinger, M. G. M. Capeluto, V. Kaymak, A. Pukhov, S. Wang, A. Rockwood, Y. Wang, D. Keiss, R. Tommasini, R. London, J. Park, M. Busquet, M. Klapisch, V. N. V. Shlyaptsev, and J. J. Rocca, "Energy penetration into arrays of aligned nanowires irradiated with relativistic intensities: Scaling to terabar pressures," *Science Advances*, vol. 3, no. 1, pp. 3–11, 2017.

- [11] M. a. Purvis, V. N. Shlyaptsev, R. Hollinger, C. Bargsten, A. Pukhov, A. Prieto, Y. Wang, B. M. Luther, L. Yin, S. Wang, and J. J. Rocca, “Relativistic plasma nanophotonics for ultra-high energy density physics,” *Nature photonics*, vol. 7, no. 10, pp. 796–800, 2013.
- [12] R. Hollinger, C. Bargsten, V. N. V. Shlyaptsev, V. Kaymak, A. Pukhov, M. G. M. Capeluto, S. Wang, A. Rockwood, Y. Wang, A. Townsend, A. Prieto, P. Stockton, A. Curtis, and J. J. Rocca, “Efficient picosecond x-ray pulse generation from plasmas in the radiation dominated regime,” *Optica*, vol. 4, no. 11, p. 1344, 2017.
- [13] G. Kulcsar, D. AlMawlawi, F. Budnik, P. Herman, M. Moskovits, L. Zhao, and R. Marjoribanks, “Intense picosecond X-Ray pulses from laser plasmas by use of nanostructured “Velvet” targets,” *Physical review letters*, vol. 84, no. 22, pp. 5149–52, 2000.
- [14] P. P. Rajeev, P. Taneja, P. Ayyub, A. S. Sandhu, and G. R. Kumar, “Metal nanoplasmas as bright sources of hard X-ray pulses.” *Physical review letters*, vol. 90, no. 11, p. 115002, 2003.
- [15] T. Nishikawa, H. Nakano, K. Oguri, N. Uesugi, M. Nakao, K. Nishio, and H. Masuda, “Nanocylinder-array structure greatly increases the soft X-ray intensity generated from femtosecond-laser-produced plasma,” *Applied Physics B-Lasers and Optics*, vol. 73, no. 2, pp. 185–188, 2001.
- [16] S. Jiang, A. G. Krygier, D. W. Schumacher, K. U. Akli, and R. R. Freeman, “Enhancing Bremsstrahlung production from ultraintense laser-solid interactions with front surface structures,” *European Physical Journal D*, vol. 68, no. 10, 2014.
- [17] Z. Zhao, L. Cao, L. Cao, J. Wang, W. Huang, W. Jiang, Y. He, Y. Wu, K. Dong, Y. Ding, B. Zhang, Y. Gu, M. Y. Yu, X. T. He, Z. Zhao, L. Cao, L. Cao, J. Wang, W. Huang, and W. Jiang, “Acceleration and guiding of fast electrons by a nanobrush target Acceleration and guiding of fast electrons by a nanobrush target,” vol. 123108, no. 2010, 2012.

- [18] A. Curtis, C. Calvi, J. Tinsley, R. Hollinger, V. Kaymak, A. Pukhov, S. Wang, A. Rockwood, Y. Wang, V. Shlyaptsev, J. Rocca, and J. R. A. Curtis, C. Calvi, J. Tinsley, R. Hollinger, V. Kaymak, A. Pukhov, S. Wang, A. Rockwood, Y. Wang, V. Shlyaptsev, “Micro-Scale Fusion in Dense Relativistic Nanowire Array Plasmas,” *Nature Communications*, vol. Accepted, no. 1, 2018.
- [19] F. Brunel, “Not-so-resonant, resonant absorption,” *Phys. Rev. Lett.*, vol. 59, pp. 52–55, jul 1987.
- [20] D. Neely, P. Mckenna, R. Wilson, M. King, R. J. Gray, D. C. Carroll, R. J. Dance, and C. Armstrong, “Ellipsoidal plasma mirror focusing of high power laser pulses to ultra-high intensities,” vol. 033106, no. 2016, 2017.
- [21] A. Caruso and R. Gratton, “Interaction of short laser pulses with solid materials,” *Plasma Physics*, vol. 11, no. 10, p. 839, 1969.
- [22] J. H. Bechtel, “Heating of solid targets with laser pulses,” *Journal of Applied Physics*, vol. 46, pp. 1585–1593, apr 1975.
- [23] M. D. Perry, D. Pennington, B. C. Stuart, G. Tietbohl, J. A. Britten, C. Brown, S. Herman, B. Golick, M. Kartz, J. Miller, H. T. Powell, M. Vergino, and V. Yanovsky, “Petawatt laser pulses,” *Opt. Lett.*, vol. 24, pp. 160–162, feb 1999.
- [24] S. P. Hatchett, C. G. Brown, T. E. Cowan, E. A. Henry, J. S. Johnson, M. H. Key, J. A. Koch, A. B. Langdon, B. F. Lasinski, R. W. Lee, A. J. Mackinnon, D. M. Pennington, M. D. Perry, T. W. Phillips, M. Roth, T. C. Sangster, M. S. Singh, R. A. Snavely, M. A. Stoyer, S. C. Wilks, and K. Yasuike, “Electron, photon, and ion beams from the relativistic interaction of Petawatt laser pulses with solid targets,” *Physics of Plasmas*, vol. 7, no. 5, pp. 2076–2082, 2000.
- [25] A. Y. Faenov, J. Colgan, S. B. Hansen, A. Zhidkov, T. A. Pikuz, M. Nishiuchi, S. A. Pikuz, I. Y. Skobelev, J. Abdallah, H. Sakaki, A. Sagisaka, A. S. Pirozhkov, K. Ogura, Y. Fukuda, M. Kanasaki, N. Hasegawa, M. Nishikino, M. Kando, Y. Watanabe, T. Kawachi, S. Masuda,

- T. Hosokai, R. Kodama, and K. Kondo, “Nonlinear increase of X-ray intensities from thin foils irradiated with a 200 TW femtosecond laser,” *Scientific Reports*, vol. 5, no. February, pp. 1–13, 2015.
- [26] N. Rohringer, D. Ryan, R. A. London, M. Purvis, F. Albert, J. Dunn, J. D. Bozek, C. Bostedt, A. Graf, R. Hill, S. P. Hau-Riege, and J. J. Rocca, “Atomic inner-shell X-ray laser at 1.46 nanometres pumped by an X-ray free-electron laser,” *Nature*, vol. 481, p. 488, jan 2012.
- [27] L. Young, E. P. Kanter, B. Krässig, Y. Li, A. M. March, S. T. Pratt, R. Santra, S. H. Southworth, N. Rohringer, L. F. Dimauro, G. Doumy, C. A. Roedig, N. Berrah, L. Fang, M. Hoener, P. H. Bucksbaum, J. P. Cryan, S. Ghimire, J. M. Glowia, D. A. Reis, J. D. Bozek, C. Bostedt, and M. Messerschmidt, “Femtosecond electronic response of atoms to ultra-intense X-rays,” *Nature*, vol. 466, no. 7302, pp. 56–61, 2010.
- [28] M. A. Alkhimova, A. Y. Faenov, I. Y. Skobelev, T. A. Pikuz, M. Nishiuchi, H. Sakaki, A. S. Pirozhkov, A. Sagisaka, N. P. Dover, K. Kondo, K. Ogura, Y. Fukuda, H. Kiriya, K. Nishitani, T. Miyahara, Y. Watanabe, S. A. Pikuz, M. Kando, R. Kodama, and K. Kondo, “High resolution X-ray spectra of stainless steel foils irradiated by femtosecond laser pulses with ultra-relativistic intensities,” *Optics Express*, vol. 25, no. 23, p. 29501, 2017.
- [29] S. Hansen, J. Bauche, C. Bauche-Arnoult, and M. Gu, “Hybrid atomic models for spectroscopic plasma diagnostics,” *High Energy Density Physics*, vol. 3, pp. 109–114, may 2007.
- [30] D. J. Hoarty, P. Allan, S. F. James, C. R. D. Brown, L. M. R. Hobbs, M. P. Hill, J. W. O. Harris, J. Morton, M. G. Brookes, R. Shepherd, J. Dunn, H. Chen, E. Von Marley, P. Beiersdorfer, H. K. Chung, R. W. Lee, G. Brown, and J. Emig, “The first data from the Orion laser; measurements of the spectrum of hot, dense aluminium,” *High Energy Density Physics*, vol. 9, no. 4, pp. 661–671, 2013.
- [31] D. J. Hoarty, P. Allan, S. F. James, C. R. Brown, L. M. Hobbs, M. P. Hill, J. W. Harris, J. Morton, M. G. Brookes, R. Shepherd, J. Dunn, H. Chen, E. Von Marley, P. Beiersdorfer,

- H. K. Chung, R. W. Lee, G. Brown, and J. Emig, "Observations of the effect of ionization-potential depression in hot dense plasma," *Physical Review Letters*, vol. 110, no. 26, pp. 1–5, 2013.
- [32] K. U. Akli, S. B. Hansen, A. J. Kemp, R. R. Freeman, F. N. Beg, D. C. Clark, S. D. Chen, D. Hey, S. P. Hatchett, K. Highbarger, E. Giraldez, J. S. Green, G. Gregori, K. L. Lancaster, T. Ma, A. J. MacKinnon, P. Norreys, N. Patel, J. Pasley, C. Shearer, R. B. Stephens, C. Stoeckl, M. Storm, W. Theobald, L. D. Van Woerkom, R. Weber, and M. H. Key, "Laser heating of solid matter by light-pressure-driven shocks at ultrarelativistic intensities," *Physical Review Letters*, vol. 100, no. 16, pp. 1–4, 2008.
- [33] S. P. Gordon, T. Donnelly, a. Sullivan, H. Hamster, and R. W. Falcone, "X rays from microstructured targets heated by femtosecond lasers.," *Optics letters*, vol. 19, no. 7, pp. 484–486, 1994.
- [34] F. Khattak, R. Clarke, E. Divall, M. Edwards, P. Foster, C. Hooker, A. Langley, O. du Sert Percie, C. Spindloe, G. Tallents, D. Riley, P. Mistry, D. Neely, J. Smith, and M. Tolley, "Enhanced He-alpha emission from "smoked" Ti targets irradiated with 400nm, 45 fs laser pulses," *Europhysics Letters*, vol. 242, no. 72, p. 242, 2005.
- [35] H. A. Sumeruk, S. Kneip, D. R. Symes, I. V. Churina, a. V. Belolipetski, T. D. Donnelly, and T. Ditmire, "Control of strong-laser-field coupling to electrons in solid targets with wavelength-scale spheres," *Physical Review Letters*, vol. 98, no. 4, p. 045001, 2007.
- [36] M. M. Murnane, H. C. Kapteyn, S. P. Gordon, J. Bokor, E. N. Glytsis, and R. W. Falcone, "Efficient coupling of high-intensity subpicosecond laser pulses into solids," *Applied Physics Letters*, vol. 62, no. 10, pp. 1068–1070, 1993.
- [37] S. Kahaly, S. K. Yadav, W. M. Wang, S. Sengupta, Z. M. Sheng, A. Das, P. K. Kaw, and G. R. Kumar, "Near-Complete Absorption of Intense , Ultrashort Laser Light by Sub- Gratings," *Physical Review Letters*, vol. 101, no. 14, p. 145001, 2008.

- [38] A. Ovchinnikov, O. Kostenko, O. Chefonov, O. Rosmej, N. Andreev, M. Agranat, J. Duan, J. Liu, and V. Fortov, “Characteristic X-rays generation under the action of femtosecond laser pulses on nano-structured targets,” *Laser and Particle Beams*, vol. 29, no. 02, pp. 249–254, 2011.
- [39] S. Mondal, I. Chakraborty, S. Ahmad, D. Carvalho, P. Singh, A. D. Lad, V. Narayanan, P. Ayyub, G. R. Kumar, J. Zheng, and Z. M. Sheng, “Highly enhanced hard x-ray emission from oriented metal nanorod arrays excited by intense femtosecond laser pulses,” *Physical Review B - Condensed Matter and Materials Physics*, vol. 83, no. 3, pp. 1–5, 2011.
- [40] W. Theobald, K. Akli, R. Clarke, J. a. Delettrez, R. R. Freeman, S. Glenzer, J. Green, G. Gregori, R. Heathcote, N. Izumi, J. a. King, J. a. Koch, J. Kuba, K. Lancaster, a. J. MacKinnon, M. Key, C. Mileham, J. Myatt, D. Neely, P. a. Norreys, H. S. Park, J. Pasley, P. Patel, S. P. Regan, H. Sawada, R. Shepherd, R. Snavely, R. B. Stephens, C. Stoeckl, M. Storm, B. Zhang, and T. C. Sangster, “Hot surface ionic line emission and cold K-inner shell emission from petawatt-laser-irradiated Cu foil targets,” *Physics of Plasmas*, vol. 13, no. 4, 2006.
- [41] A. Pukhov, “Three-dimensional electromagnetic relativistic particle-in-cell code VLPL (Virtual Laser Plasma Lab),” *Journal of Plasma Physics*, vol. 61, no. 3, pp. 425–433, 1999.
- [42] Y. Wang, S. Wang, A. Rockwood, B. Luther, R. Hollinger, A. Curtis, C. Calvi, C. Menoni, and J. Rocca, “0.85 PW laser operation at 3.3 Hz and high-contrast ultrahigh-intensity $\lambda = 400$ nm second-harmonic beamline,” *Optics Letters*, vol. 42, no. 19, 2017.
- [43] Z. Samsonova, S. Höfer, R. Hollinger, T. Kämpfer, I. Uschmann, R. Röder, L. Trefflich, O. Rosmej, E. Förster, C. Ronning, D. Kartashov, and C. Spielmann, “Hard X-ray Generation from ZnO Nanowire Targets in a Non-Relativistic Regime of Laser-Solid Interactions,” *Applied Sciences*, vol. 8, no. 10, 2018.
- [44] A. P. Shevelko, A. a. Antonov, I. G. Grigorieva, Y. S. Kasyanova, L. V. Knight, a. Reyesmenac, C. Turnerc, Q. Wang, and O. F. Yakusheva, “A Focusing Crystal von Hamos Spec-

- trometer for X-ray Spectroscopy and X-ray Fluorescence Applications,” *Proc. of SPIE*, vol. 4144, pp. 148–154, 2000.
- [45] a. P. Shevelko, Y. S. Kasyanov, O. F. Yakushev, and L. V. Knight, “Compact focusing von Hamos spectrometer for quantitative x-ray spectroscopy,” *Review of Scientific Instruments*, vol. 73, no. 10, p. 3458, 2002.
- [46] A. L. Prieto, M. Martín-González, J. Keyani, R. Gronsky, T. Sands, and A. M. Stacy, “The electrodeposition of high-density, ordered arrays of Bi_{1-x}Sb_x nanowires,” *Journal of the American Chemical Society*, vol. 125, no. 9, pp. 2388–2389, 2003.
- [47] Y. Liang, C. Zhen, D. Zou, and D. Xu, “Preparation of free-standing nanowire arrays on conductive substrates,” *Journal of the American Chemical Society*, vol. 126, no. 50, pp. 16338–16339, 2004.
- [48] F. J. Marshall, P. W. McKenty, J. a. Delettrez, R. Epstein, J. P. Knauer, V. a. Smalyuk, J. a. Frenje, C. K. Li, R. D. Petrasso, F. H. Séguin, and R. C. Mancini, “Plasma-density determination from X-ray radiography of laser-driven spherical implosions,” *Physical Review Letters*, vol. 102, no. 18, p. 185004, 2009.
- [49] C. M. Huntington, C. M. Krauland, C. C. Kuranz, R. P. Drake, H. S. Park, D. H. Kalantar, B. R. Maddox, B. a. Remington, and J. Kline, “Development of a short duration backlit pinhole for radiography on the National Ignition Facility,” *Review of Scientific Instruments*, vol. 81, no. 10, p. 10E536, 2010.
- [50] J. E. Bailey, T. Nagayama, G. P. Loisel, G. a. Rochau, C. Blancard, J. Colgan, P. Cosse, G. Faussurier, C. J. Fontes, F. Gilleron, I. Golovkin, S. B. Hansen, C. a. Iglesias, D. P. Kilcrease, J. J. Macfarlane, R. C. Mancini, S. N. Nahar, C. Orban, J. Pain, a. K. Pradhan, M. Sherrill, and B. G. Wilson, “A higher-than-predicted measurement of iron opacity at solar interior temperatures,” *Nature*, vol. 517, p. 56, 2015.

- [51] B. Yaakobi, T. R. Boehly, D. D. Meyerhofer, T. J. B. Collins, B. A. Remington, P. G. Allen, S. M. Pollaine, H. E. Lorenzana, and J. H. Eggert, “EXAFS measurement of iron bcc-to-hcp phase transformation in nanosecond-laser shocks,” *Physical Review Letters*, vol. 95, no. 7, pp. 1–4, 2005.
- [52] A. Cavalleri, C. W. Siders, F. L. H. Brown, D. M. Leitner, C. Toth, J. A. Squier, C. P. J. Barty, K. R. Wilson, K. Sokolowski-Tinten, M. Horn Von Hoegen, D. Von Der Linde, M. Kammler, C. T??th, J. A. Squier, C. P. J. Barty, K. R. Wilson, K. Sokolowski-Tinten, M. Horn Von Hoegen, D. Von Der Linde, and M. Kammler, “Anharmonic lattice dynamics in germanium measured with ultrafast X-ray diffraction,” *Physical Review Letters*, vol. 85, no. 3, pp. 586–589, 2000.
- [53] P. P. Rajeev, P. Ayyub, S. Bagchi, and G. R. Kumar, “Nanostructures, local fields, and enhanced absorption in intense light-matter interaction.,” *Optics letters*, vol. 29, no. 22, pp. 2662–2664, 2004.
- [54] M. J. May, Y. P. Opachich, G. E. Kemp, J. D. Colvin, M. A. Barrios, K. W. Widmann, K. B. Fournier, M. Hohenberger, F. Albert, and S. P. Regan, “Demonstration of a long pulse X-ray source at the National Ignition Facility,” *Physics of Plasmas*, vol. 24, no. 4, p. 042701, 2017.
- [55] F. Pérez, J. J. Kay, J. R. Patterson, J. Kane, B. Villette, F. Girard, C. Reverdin, M. May, J. Emig, C. Sorce, J. Colvin, S. Gammon, J. Jaquez, J. H. Satcher, and K. B. Fournier, “Efficient laser-induced 6-8 keV x-ray production from iron oxide aerogel and foil-lined cavity targets,” *Physics of Plasmas*, vol. 19, no. 8, p. 083101, 2012.
- [56] E. L. Dewald, M. Rosen, S. H. Glenzer, L. J. Suter, F. Girard, J. P. Jadaud, J. Schein, C. Constantin, F. Wagon, G. Huser, P. Neumayer, and O. L. Landen, “X-ray conversion efficiency of high-Z hohlraum wall materials for indirect drive ignition,” *Physics of Plasmas*, vol. 15, no. 7, p. 072706, 2008.

- [57] D. Babonneau, M. Primout, F. Girard, J. P. Jadaud, M. Naudy, B. Villette, S. Depierreux, C. Blancard, G. Faussurier, K. B. Fournier, L. Suter, R. Kauffman, S. Glenzer, M. C. Miller, J. Grün, and J. Davis, “Efficient multi-keV X-ray sources from laser-exploded metallic thin foils,” *Physics of Plasmas*, vol. 15, no. 9, p. 092702, 2008.
- [58] C. A. Back, J. Grun, C. Decker, L. J. Suter, J. Davis, O. L. Landen, R. Wallace, W. W. Hsing, J. M. Laming, U. Feldman, M. C. Miller, and C. Wuest, “Efficient Multi-keV Underdense Laser-Produced Plasma Radiators,” *Physical Review Letters*, vol. 87, no. 27, p. 275003, 2001.
- [59] D. H. Martz, D. Alessi, B. M. Luther, Y. Wang, D. Kemp, M. Berrill, and J. J. Rocca, “2 . 5 Hz repetition rate excited by a slab-pumped Ti : sapphire laser,” *Optics Letters*, vol. 35, no. 10, pp. 1632–1634, 2010.
- [60] V. S. Vinogradov, A.V., “Characteristics of a laser plasma x-ray source (review),” *Sov. J. Quantum. Electron*, vol. 17, no. 1, p. 1, 1987.
- [61] S. Bagchi, P. P. Kiran, K. Yang, a. M. Rao, M. K. Bhuyan, M. Krishnamurthy, and G. R. Kumar, “Bright, low debris, ultrashort hard x-ray table top source using carbon nanotubes,” *Physics of Plasmas*, vol. 18, no. 1, pp. 16–19, 2011.
- [62] S. Palaniyappan, B. M. Hegelich, H. C. Wu, D. Jung, D. C. Gautier, L. Yin, B. J. Albright, R. P. Johnson, T. Shimada, S. Letzring, D. T. Offermann, J. Ren, C. Huang, R. Hörlein, B. Dromey, J. C. Fernandez, and R. C. Shah, “Dynamics of relativistic transparency and optical shuttering in expanding overdense plasmas,” *Nature Physics*, vol. 8, pp. 763–769, aug 2012.
- [63] V. Kaymak, A. Pukhov, V. N. Shlyaptsev, and J. J. Rocca, “Nanoscale Ultradense Z -Pinch Formation from Laser-Irradiated Nanowire Arrays,” *Physical Review Letters*, vol. 117, no. 3, pp. 1–5, 2016.

- [64] E. Träbert, S. B. Hansen, P. Beiersdorfer, G. V. Brown, K. Widmann, and H. K. Chung, “L-shell spectroscopy of Au as a temperature diagnostic tool,” *Review of Scientific Instruments*, vol. 79, no. 10, pp. 1–4, 2008.
- [65] G. V. Brown, S. B. Hansen, E. Träbert, P. Beiersdorfer, K. Widmann, H. Chen, H. K. Chung, J. H. T. Clementson, M. F. Gu, and D. B. Thorn, “Investigation of the $2p_{3/2}$ - $3d_{5/2}$ line emission of Au^{53+} & Au^{69+} for diagnosing high energy density plasmas,” *Physical Review E*, vol. 77, no. 6, p. 066406, 2008.
- [66] M. J. May, M. B. Schneider, S. B. Hansen, H. K. Chung, D. E. Hinkel, H. A. Baldis, and C. Constantin, “X-ray spectral measurements and collisional-radiative modeling of hot, gold plasmas at the omega laser,” *High Energy Density Physics*, vol. 4, no. 3-4, pp. 78–87, 2008.
- [67] H. K. Chung, M. H. Chen, W. L. Morgan, Y. Ralchenko, and R. W. Lee, “FLYCHK: Generalized population kinetics and spectral model for rapid spectroscopic analysis for all elements,” *High Energy Density Physics*, vol. 1, no. 1, pp. 3–12, 2005.
- [68] J. C. Fernández, D. Cort Gautier, C. Huang, S. Palaniyappan, B. J. Albright, W. Bang, G. Dyer, A. Favalli, J. F. Hunter, J. Mendez, M. Roth, M. Swinhoe, P. A. Bradley, O. Depert, M. Espy, K. Falk, N. Guler, C. Hamilton, B. M. Hegelich, D. Henzlova, K. D. Ianakiev, M. Iliev, R. P. Johnson, A. Kleinschmidt, A. S. Losko, E. McCary, M. Mocko, R. O. Nelson, R. Roycroft, M. A. Santiago Cordoba, V. A. Schanz, G. Schaumann, D. W. Schmidt, A. Sefkow, T. Shimada, T. N. Taddeucci, A. Tebartz, S. C. Vogel, E. Vold, G. A. Wurden, and L. Yin, “Laser-plasmas in the relativistic-transparency regime: Science and applications,” *Physics of Plasmas*, vol. 24, no. 5, p. 56702, 2017.
- [69] R. Tommasini, C. Bailey, D. K. Bradley, M. Bowers, H. Chen, J. M. Di Nicola, P. Di Nicola, G. Gururangan, G. N. Hall, C. M. Hardy, D. Hargrove, M. Hermann, M. Hohenberger, J. P. Holder, W. Hsing, N. Izumi, D. Kalantar, S. Khan, J. Kroll, O. L. Landen, J. Lawson, D. Martinez, N. Masters, J. R. Nafziger, S. R. Nagel, A. Nikroo, J. Okui, D. Palmer, R. Sigurdsson,

S. Vonhof, R. J. Wallace, and T. Zobrist, “Short pulse, high resolution, backlighters for point projection high-energy radiography at the National Ignition Facility,” *Physics of Plasmas*, vol. 24, no. 5, 2017.

[70] Z. Lécz and A. Andreev, “Bright synchrotron radiation from nano-forest targets,” *Physics of Plasmas*, vol. 24, p. 33113, mar 2017.

[71] B. Martinez, E. D’Humières, and L. Gremillet, “Synchrotron emission from nanowire array targets irradiated by ultraintense laser pulses,” *Plasma Physics and Controlled Fusion*, vol. 60, no. 7, p. 74009, 2018.